Magnetic properties of surface-adsorbed single rare earth atoms, molecules, and atomic scale clusters

THÈSE N^{O} 7921 (2017)

PRÉSENTÉE LE 16 NOVEMBRE 2017
À LA FACULTÉ DES SCIENCES DE BASE
LABORATOIRE DE NANOSTRUCTURES SUPERFICIELLES
PROGRAMME DOCTORAL EN PHYSIQUE

ÉCOLE POLYTECHNIQUE FÉDÉRALE DE LAUSANNE

POUR L'OBTENTION DU GRADE DE DOCTEUR ÈS SCIENCES

PAR

Aparajita SINGHA

acceptée sur proposition du jury:

Prof. C. Hébert, présidente du jury
Prof. H. Brune, directeur de thèse
Prof. A. Khajetoorians, rapporteur
Dr A. Barla, rapporteur
Prof. J.-Ph. Ansermet, rapporteur

ÉCOLE POLYTECHNIQUE
FÉDÉRALE DE LAUSANNE
Suisse
2017

"...when you have eliminated the impossible, whatever remains, however improbable, must be the truth".
— Sir Arthur Conan Doyle

Dedicated to my mom Avralekha Singha and my husband Soham Basu.

Acknowledgements

I want to express my sincere gratitude to Prof. Harald Brune, for supervising this thesis, for his invaluable scientific inputs on our manuscripts, for encouraging my participation in beamtimes in different parts of Europe (SLS, Grenoble, and Trieste), and for supporting my participation in numerous international schools, lectures, and conferences which have boosted my scientific growth. Above all, I am thankful to him since he believed in me when I wanted to join a completely new field, while changing my career from experimental biophysics.

I am very thankful to Dr. Fabio Donati for providing regular supervision and for encouraging me to develop critical scientific approach during these four years. I want to thank him especially for his passionate and yet relaxed and patient teaching skills. I enjoyed learning from our regular scientific discussions in front of the STM, during the beamtimes, on our manuscript drafts, and especially the brain-storming sessions over many scientific models such as the rate equations, multiplet analysis and the spin Hamiltonian. Apart from physics, he also showed me how to deal with complicated systems and stressful situations (be it in the lab or in real life) with a lot of positive attitude and energy.

I want to express my appreciation to Dr. Stefano Rusponi for his availability to initiate any scientific discussion, for the several day and night shifts shared during the beamtimes, and for always providing a critical outlook to my work. Many thanks and appreciations to Dr. Marina Pivetta for allowing me to measure the Er clusters in her STM, for her constructive feedback on the manuscripts and the figures therein and above all for providing me with invaluable personal mentorship and support whenever I needed them. I will remain grateful for the endless support from Dr. François Patthey for dealing with the 0.4 K STM. His active presence accelerated the completion of the Ho-Co project within a very limited time frame.

Special thanks to Dr. Christian Wäckerlin and Dr. Katharina J. Diller for introducing me to world of magnetic molecules and for their constructive scientific criticism on my presentations which have helped me grow during these years. I am also thankful to Kathi for introducing me to XPS. I want to acknowledge Dr. Jan Dreiser for our active collaborations in XMCD projects, his feedback to improvise our manuscripts, and his ever-present beamline support at SLS. I also would like to acknowledge the fruitful collaborations with the group of Prof. Pietro Gambardella at ETH Zürich, in the RE single atom projects.

I will continue to remember our regular "gossips", lunch, and coffee breaks with my fellow PhD friends and colleagues from the group. Those offered me a break from many stressful moments.

During this thesis, I have received excellent IT support especially from Primo Locatelli, contin-

uous technical support from Claude Amendola and Gilles Grandjean at the workshops, and persistent administrative help from Chantal Roulin and Carole Pascalon.
I want to thank Soham for providing mental support and for forgiving my crazy working hours and habits. Many thanks to my mom for all the sacrifices she made throughout this journey and for being the constant source of motivation, determination, and strength. This journey would have been impossible to initiate without the continued support from my loving sisters (Archita and Anuva) and Soumit da.
Finally, without mentioning any names, I want to thank all my friends in Switzerland and abroad who stayed by me during these years and forced me to relax "a bit" in stressful moments.
Lausanne, 15 May 2017 A. S.

Abstract

This thesis presents combined experimental and theoretical investigations of nanoscale, surface-supported magnets based on rare earths (RE) to understand and control the magnetic properties down to the scale of single atoms.

Firstly, we present the effects of adatom-substrate interaction on the magnetic properties of isolated single RE atoms using x-ray absorption spectroscopy (XAS), x-ray magnetic circular dichroism (XMCD), and multiplet analysis. Our systematic investigations of Dy, Ho, Er, and Tm adatoms adsorbed on Pt(111), Cu(111), Ag(100), and Ag(111), reveal that the REs can possess two types of $4f$ occupancy on the metal substrates, namely divalent with $4f^n$ and trivalent with $4f^{n-1}$, where n is the $4f$ occupation of the free RE atom in its gas phase. The $4f^{n-1}$ state is realized in presence of low $4f-5d$ promotion energy of the RE and strong hybridization of their external spd shell with the surrounding environment. Notably, none of the REs exhibit magnetic hysteresis, suggesting that magnetic relaxation is faster than approximately 10 seconds.

Secondly, we report on the effect of electrostatic interaction between different adatoms by studying the size-dependent magnetic properties of Er clusters adsorbed on Cu(111). Combining XMCD, scanning tunneling microscopy (STM), and mean-field nucleation theory we reveal that the electrostatic interaction among the adatoms dominates over the adatom-substrate interaction in Er clusters starting from the size of three atoms. Consequently the easy axis of Er changes from in-plane for the single atoms and dimers to out-of-plane for trimers and bigger clusters. In addition, the out-of-plane magnetic anisotropy of 2.9 meV/atom results in magnetic hysteresis at 2.5 K in all clusters starting from trimers. With a magnetic lifetime of approximately 2 minutes at 0.1 T, the Er trimers are one of the smallest metal-supported ferromagnetic clusters observed so far.

The investigation of adatom-adatom interaction is further extended by studying $4f-3d$ heterodimers namely, Ho-Co adsorbed on thin insulating layers of MgO. Their magnetic easy axis is oriented along the out-of-plane direction. Using spin-polarized STM we have detected spin-excitations in these heterodimers at ±20 and ±8 meV. We have identified the origin behind these spin-excitations using an effective spin-Hamiltonian model. This model indicates that, given a ferromagnetic exchange interaction between Ho and Co, the most intense feature at ±20 meV corresponds to a transition in which the spin moment of Co is strongly diminished. This is further accompanied by an overall change of the total magnetic moment of the heterodimer, *i.e.*, $\Delta J = -1$. In contrast, the weaker transition at ±8 meV occurs following a change in the out-of-plane moment of Ho while the total moment of the

heterodimer remains intact *i.e.*, $\Delta J = 0$. Notably, we observe an effective g factor of 3.1 for the ± 20 meV transition, which significantly exceeds the free electron value of 2. In addition, the ferromagnetic coupling between Ho and Co is very unusual compared to the ferrimagnetic exchange interaction known for the bulk $4f - 3d$ compounds, especially those derived from the late lanthanides. Nonetheless, this marks the first evidence of spin-excitations in the smallest $4f$ containing cluster.

The knowledge gained on the fundamental aspects of magnetism in surface-supported REs combined with the continued parallel search for magnetic stability down to single atoms, enabled us to achieve magnetic remanence in single adatoms with lifetimes of the order of 1000 s at 2.5 K. In addition we have achieved significantly enhanced hysteresis and magnetic lifetime in the well known single molecule magnet, $TbPc_2$. My contribution to the investigation of these novel systems will be described in the last section of this thesis, especially highlighting the factors which promote the long magnetic lifetime in each case.

Key words: Magnetism, x-ray absorption spectroscopy, x-ray magnetic circular dichroism, scanning tunneling microscope, rare earth, single adatoms, clusters, magnetic lifetime, magnetic stability, magnetic hysteresis, crystal field, symmetry, single atom magnet, single molecule magnet.

Résumé

Cette thèse présente les résultats d'études expérimentales et théoriques des propriétés d'aimants à l'échelle nanométrique. Ces aimants sont composés d'atomes de terres rares (TR) et sont adsorbés sur un substrat. Le but de ces investigations est de comprendre et contrôler les propriétes magnétiques de ces objets jusqu'à l'échelle d'un atome individuel.

Tout d'abord, nous présentons les effets de l'interaction adatome-substrat sur les propriétés magnétiques d'atomes de TR isolés en utilisant la spectroscopie d'absorption de rayons X (XAS), le dichroïsme circulaire magnétique de rayons X (XMCD) et le calcul de multiplets. Nous avons étudié systématiquement les atome Dy, Ho, Er, et Tm adsorbés sur Pt(111), Cu(111), Ag(100), et Ag(111). Ces études révèlent que les TR peuvent posséder deux types d'occupation des niveaux $4f$ lorsque elles interagissent avec des substrats métalliques : divalente avec $4f^n$ et trivalente avec $4f^{n-1}$, où n est l'occupation $4f$ de l'atome TR dans sa phase gazeuse. L'état $4f^{n-1}$ est réalisé en présence d'une petite énergie de promotion $4f-5d$ et d'une forte hybridation de leur couche spd externe avec l'environnement. Notamment, aucune des TR ne présente une hystérèse magnétique, ce qui suggère que la relaxation magnétique est plus rapide que environ 10 s.

Ensuite, nous rapportons l'effet de l'interaction électrostatique entre différents adatomes en étudiant les propriétés magnétiques de clusters de Er adsorbés sur Cu(111) en fonction de leur taille. En combinant XMCD, microscopie à balayage à effet tunnel (STM) et théorie de nucléation de champ moyen, nous révélons que l'interaction électrostatique entre les adatomes domine l'interaction adatom-substrat dans les clusters de Er à partir de la taille de trois atomes. Par conséquent, l'axe d'aimantation facile de l'Er passe de la direction dans-le-plan pour les atomes et les dimères individuels à hors-plan pour les trimères et les clusters plus grands. En outre, l'anisotropie magnétique hors plan de 2.9 meV par atome entraîne une hystérèse magnétique à 2.5 K dans tous les clusters de à partir de trimères. Avec un durée de vie magnétique d'environ 2 minutes à 0.1 T, les trimères de Er sont l'un des plus petits clusters ferromagnétiques adsorbés sur une surface métallique observés jusqu'ici.

L'étude de l'interaction adatome-adatome est étendue aux hétérodimères $4f-3d$, à savoir, Ho-Co adsorbé sur de fines couches isolantes de MgO. Leur axe facile magnétique est orienté le long de la direction hors-plan. À l'aide de STM polarisé en spin, nous avons détecté des excitations de spin dans ces hétérodimères à ±20 et ±8 meV. Nous avons identifié l'origine de ces excitations de spin en utilisant un modèle d'hamiltonien de spin efficace. Ce dernier suggère un échange ferromagnétique entre Ho et Co. La structure la plus intense à ±20 meV correspond à une transition dans laquelle le moment de spin du Co est fortement réduit,

accompagné d'un changement global du moment magnétique total de l'hétérodimère, *c.-à-d.*, $\Delta J = -1$. En revanche, nous interprétons la transition plus faible à ± 8 meV comme la modification de la projection hors-plan du moment du Ho avec le moment total de l'hétérodimère restant intact *c.-à-d.*, $\Delta J = 0$. Notamment, le facteur g effectif pour la transition ± 20 meV est 3.1, ce qui dépasse considérablement la valeur de l'électron libre $g = 2$. En outre, le couplage ferromagnétique entre Ho et Co est très inhabituel par rapport à l'échange ferrimagnétique connu pour les composés $4f - 3d$, en particulier ceux dérivés des lanthanides de la fin de la série. Néanmoins, cela marque la première preuve d'excitations de spin dans le plus petit groupe contenant $4f$.

Les connaissances acquises sur les aspects fondamentaux du magnétisme des TR adsorbées en surface, associées à la recherche de la stabilité magnétique pour des nanostructures de plus en plus petites, nous ont permis de découvrir la rémanence magnétique pour un ensemble d'adatomes en surface, avec une durée de vie de l'ordre de 1000 s à 2.5 K. De plus, nous avons réalisé une hystérèse et une durée de vie magnétique considérablement améliorées par rapport aux résultats connus pour la molécule aimant, $TbPc_2$. Ma contribution à ces projets est décrite dans la dernière section de cette thèse, dans laquelle les facteurs qui favorisent l'allongement de la durée de vie magnétique de ces systèmes sont mis en évidence.

Mots clefs : Magnétisme, spectroscopie d'absorption de rayons X, dichroïsme circulaire magnétique de rayons X, microscopie à balayage à effet tunnel, terres rares, adatomes individuels, clusters, durée de vie magnétique, stabilité magnétique, hystérèse magnétique, champ cristallin, symétrie, aimant à un seul atome, molécule aimant.

Contents

List of Figures

List of Tables

Frequently used abbreviations

AF	Anti-ferromagnetic
CF	Crystal field
CF	Crystal field
DFT	Density functional theory
DOS	Density of states
EPR	Electron paramagnetic resonance
FM	Ferromagnetic
FWHM	Full width at half maximum
IETS	Inelastic tunnelling spectroscopy
LDOS	Local density of states
LF	Ligand field
LT	Low temperature
MAE	Magnetic anisotropy energy
MAE	Magnetic anisotropy energy
ML	Monolayer
MNFT	Mean-field nucleation theory
Pc	Phthalocyanine
QT	Quantum tunneling
QTM	Quantum tunnelling of magnetization
RE	Rare earth
RKKY	Ruderman-Kittel-Kasuya-Yosida
SES	Spin-excitation spectroscopy
SMM	Single molecule magnet
SO	Spin-orbit coupling
SP-tip	Spin polarize tip
STM	Scanning tunnelling microscope
STS	Scanning tunnelling spectroscopy
TEY	Total electron yield
UHV	Ultrahigh vacuum
XA	X-ray absorption
XAS	X-ray absorption spectroscopy
XLD	X-ray linear dichroism
XMCD	X-ray magnetic circular dichroism
XPS	X-ray photoemission spectroscopy
ZFS	Zero field splitting

1 Introduction

"I would like to describe a field, in which little has been done, but in which an enormous amount can be done in principle . . . it is more like solid-state physics in the sense that it might tell us much of great interest about the strange phenomena that occur in complex situations. Furthermore, a point that is most important is that it would have an enormous number of technical applications.
What I want to talk about is the problem of manipulating and controlling things on a small scale."

—R. P. FEYNMAN, *There's Plenty of Room at the Bottom*, 1959

The idea of miniaturizing the logical building blocks of a computer down to the scale of single atoms was already envisioned in 1959 by the famous physicist Richard P. Feynman. Although the need was not too obvious 60 years back, it happens to be so in today's digital world where the social media need to process data as large as 100s of petabytes on average per day[a]. Moreover the continued progress in science and technology is creating perpetual demands for efficient, *i.e.*, scalable and durable storage, transfer, and processing of this *big data* [1]. Naturally it boils down to the obvious question: how small can one bit of information be? How fast, efficient, and flawless communication can we make? Once brought up in 1959, these questions led the research in nanoscale magnetism in the past decades. A surface-supported single magnetic atom that can retain its magnetic orientation for long time and allows manipulation of its quantum magnetic states, eventually offers the possibility of encoding binary data in the magnetic orientation of the smallest unit of matter. Therefore most of the recent scientific interests in this field are largely driven by the search of magnetic stability down to the scale of single atoms at technically relevant temperatures.

However, there is a caveat! Atoms are very different than the deterministic macroscopic world we see around us. Their probabilistic nature is described by quantum mechanics [b]. Therefore as the very first step towards reaching the goal of single-atom-bit, it is crucial to understand the non-trivial quantum physics which determines the fundamental magnetic properties in surface-supported, low-coordinated atoms. This thesis endeavours to provide insights

[a] Data size estimates 1 petabytes = 10^6 gigabytes $\equiv 2 \times 10^9$ photos with average size of 500 kilobytes.
[b] Atomic radius 1 Å = 10^{-10} m, *i.e.* 5500 times smaller than the visible yellow light (550 nm).

into this through a collection of experimental and theoretical investigations of magnetism in single rare earth (RE) adatoms, molecules, and atomic-scale clusters. In particular, this work is aimed at identifying the key factors which determine the intriguing quantum magnetic properties of RE adatoms and in employing those to achieve the smallest-scale, stable magnet on surface. In the following we will first introduce the basic concepts of quantum magnetism at the nanoscale followed by an overview of the enormous progress made in the past decades. Further to this we will provide the rationale behind the choice of REs and finally we will describe the main objectives of the thesis.

1.1 Magnetism of low dimensional systems

The classical concepts of magnetism becomes inadequate for describing the properties of a nanoscale magnet where quantum effects play a predominant role. For a classical bulk magnet the magnetic energy is a continuous function of magnetization direction. In contrast, quantum mechanics imposes a set of discrete states in low dimensional systems. As a prototype of such systems, we first consider the case of a free magnetic atom in its gas phase. The electrons in its unfilled electronic shells give rise to the spin and orbital component of its magnetic moment J. Under the full rotational symmetry of the free atom J lacks directional preference. However, unlike the classical case, only a few discrete orientations of J are allowed. Given the rotational symmetry of the atom these orientations can be characterized by the projections of J along an arbitrary quantization axis z *i.e.*, J_z (Figure 1.1a upper panel) [c]. The high symmetry of the free atom implies that these $\pm J_z$ levels are degenerate. In other words, the free atom does not possess any magnetic anisotropy (lower panel of Figure 1.1a).

This scenario changes when the atom is placed on a substrate since the substrate breaks the inversion symmetry. In addition, it allows interactions between the magnetic atom and local environment [d], an effect commonly termed as the crystal field (CF). The CF lifts the degeneracy among the J_z levels. Figure 1.1b depicts the case of an axially symmetric CF. For simplicity, and as this is the case for many surface-supported systems, the quantization axis is chosen along the surface normal and this defines the z axis of the coordinate system (upper panel of Figure 1.1b). The strength of the CF is proportional to $-|J_z^2|$. This assumption is valid only if the higher order uniaxial and transverse terms can be ignored (which are discussed later). Therefore the J_z levels are split into a parabolic energy distribution (lower panel of Figure 1.1b). Given this level diagram, we can define the energy gap between the ground state doublets and the highest lying state as the magnetic anisotropy energy (MAE) whereas the difference between ground and first excited state can be termed as the zero field splitting (ZFS). The latter is to recall that this description holds true in absence of any external magnetic field, *i.e.*$B = 0$, a non-zero value of which will introduce Zeeman splitting and thereby it will distort the level distribution [3].

[c] Both J and J_z are quantized. The occupancy of the open electronic shells determines the values of J, whereas J_z is obtained following Hund's rules: $J_z = (-J, -J+1, \cdots, J-1, J)$ [2] (discrete red levels in Figure 1.1a lower panel)

[d] The magnetic atom can interact with the electrons from the atoms of the substrate or surrounding ligands.

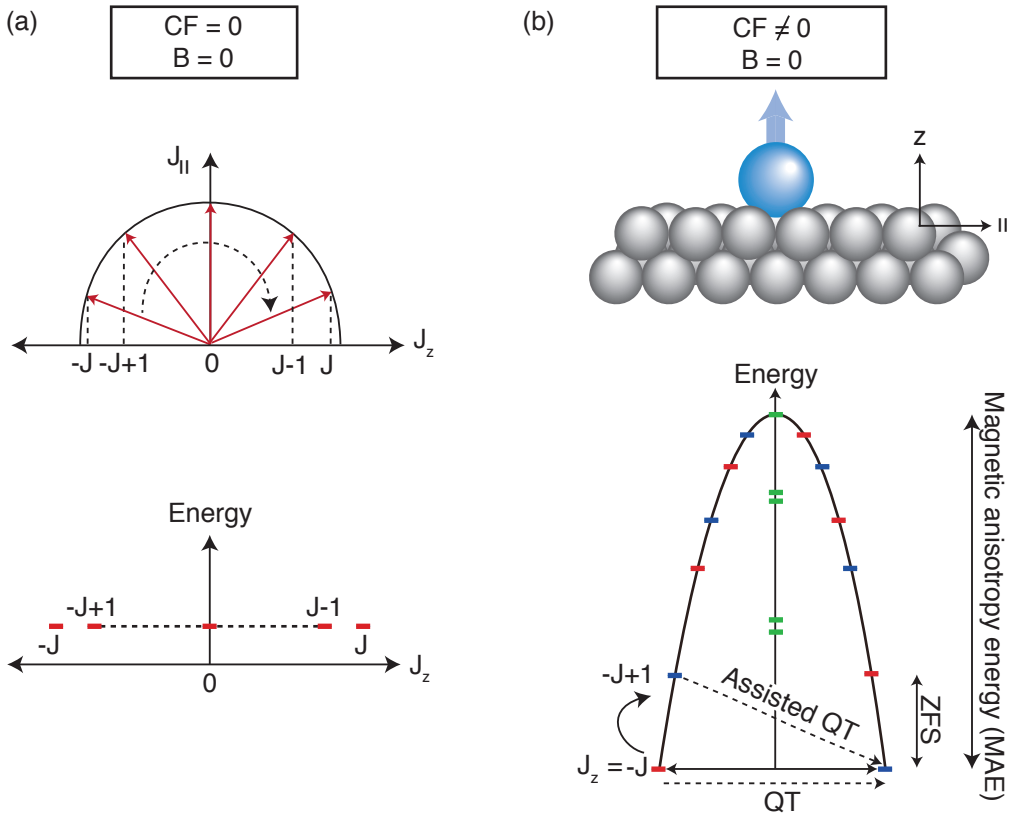

Figure 1.1: Schematic showing the magnetic level distribution of an atom (a) in absence and (b) in presence of a CF. External magnetic field $B = 0$ in both cases. The different projections of the J moment along the rotational axis of symmetry z are shown in the upper panel of (a). In (b) various possible pathways of quantum tunneling are shown in dotted lines along with the definitions of MAE and ZFS. The magnetic levels which undergo similar transformations under the CF symmetry are designated with the same color. The blue arrows indicate the magnetic moment of the atom drawn as blue sphere, whereas the substrate is shown in units of grey spheres.

The MAE defines the energy required to fully reverse the orientation of the magnetic moment. Due to the quantum nature of low dimensional systems, there is a finite probability for direct transitions from one side of the barrier to the other without crossing the real barrier height. In fact it occurs when the CF is not strictly uniaxial, *i.e.*, it contains terms which promote finite overlap or mixing of the otherwise pure quantum states and thereby can induce switching of the ground state doublets. These are the so called transverse terms of the CF and the process is known as quantum tunneling (QT) (lower panel of Figure 1.1b). In this case the total barrier becomes transparent to the magnetic element since a direct route from $-J_z$ to J_z or indirect channels *via* excited states open up [e]. The latter occurs through sequential spin excitations to higher lying states, if transitions from those excited states to the ground state doublets are

[e] Given an m fold symmetry of the CF, magnetic levels with $J_z \propto \pm m$ are connected across the barrier [4–6].

allowed (assisted QT in Figure 1.1b). Such sequential spin excitations can arise due to the tunneling electrons in a scanning tunnleing microscope (STM), the conduction electrons of the substrate that can scatter off the magnetic atom or molecule, and phononic excitations. The quantum tunnelling of magnetization (QTM) essentially reduces the effective barrier for magnetization reversal and therefore it is identified as one of the key elements which can shorten the magnetic lifetime in surface-supported single magnetic atoms or molecules [7–12]. In order to rule out such QTM one needs to make clever choices of CF symmetry and the atomic magnetic moment in the ground state. The relevant concepts are beautifully illustrated in refs. [4–6].

1.1.1 Nanoscale magnetism: some exemplary steps

The understanding of nanoscale magnetism has advanced remarkably in the past two decades through the intensive experimental and theoretical investigations on three types of systems, namely, single molecules containing one or more magnetic cores, clusters made of a few magnetically coupled atoms, and single atoms adsorbed on different kinds of substrates. In the following we will briefly describe the evolution of each stream with explicit emphasis on the respective milestones.

The field of single molecule magnets (SMM) was initiated with the discovery of magnetic stability in bulk crystalline structure of an Mn_{12} complex in 1993, with magnetic lifetime of the order of months at 2 K and an effective barrier for magnetization reversal of 6.3 meV [13]. Initial 10 years of this field was mainly focused in preparing and studying magnetic cores comprising of $3d$ metal clusters of large total spin, this being the promising key element for stabilizing high spin ground state doublets. However, it was soon realized that this approach may compromise on the total amount of magnetic anisotropy as it has been illustrated through few evidences. For instance, an Mn_{19} complex which has a total spin of 83/2, showed 12 times smaller effective barrier for magnetization reversal compared to the Mn_{12} complex [14]. For the successful design of a SMM, the need of optimizing the CF parameters for each magnetic center was recognized at this point. A profound illustration of this can be found in an article entitled "*What is not required to make a single molecule magnet*" by Nesse *et al.* [15].

The discovery of exceptionally large barrier for magnetization reversal and long spin relaxation time in lanthanide phthalocyanine sandwich complexes in 2003 brought a new direction to this field [f]. Mononuclear complex of $TbPc_2$ containing one Tb^{3+} ion was the first lanthanide based system that was reported to possess a large effective barrier of 28 meV [16]. Fundamentally different from the $3d$ metal cluster complexes, the magnetic anisotropy in the lanthanide

[f] The stability of a quantum magnet is characterized by two timescales, namely, the energy (spin) relaxation time T_1 and phase-coherence time T_2. In the context of qubits, the former defines the time to reach the thermodynamic equilibrium. For all of our systems, we measure the spin relaxation time described as the time taken by the system to relax from an excited state ($|1\rangle$) to the ground state ($|0\rangle$). This is quite different from the energy relaxation time in its physical meaning but it coincides often with T_1. For a quantum superposition of states, the T_2 describes the timescale within which the phase coherence is lost.

based systems originates from their very strong spin-orbit coupling. Following the discovery of $TbPc_2$, several other SMMs with different lanthanide cation center (*e.g.*, Dy^{3+}, Ho^{3+}, Er^{3+} etc.) were also explored. For a broad overview on lanthanide based SMMs, the readers are referred to ref. [17]. Notably, interests have also grown in anchoring the SMMs to conducting surfaces. The surface allows them to be individually addressable through scanning probes, which is interesting for both high resolution morphological studies as well as for local spectroscopic investigations [9, 18–20].

For a typical surface-supported SMM, the molecular cage around the magnetic center imposes a lateral distance between the adjacent molecules on surface. This allows the investigations of the true *single molecule* behaviour. In addition, the molecular cage protects the magnetic atom(s) from contaminations. However, the interaction between the magnetic atom(s) and the electrons and phonons of the surrounding ligands can potentially limit the magnetic stability. Therefore, in the pursuit of better performances the potential of individual magnetic atoms and clusters directly adsorbed on surfaces have also been explored recently. In this context, the experimental evidence of remarkable magnetic stability in artificially constructed clusters of a few exchange coupled $3d$ metal atoms, has been a breakthrough. Due to either ferromagnetic (FM) coupling among the atoms at 0.3 K [21] or anti-ferromagnetic (AF) coupling at 0.5 K [22], these clusters exhibit magnetic lifetime of the order of hours.

Magnetism in surface-adsorbed single atoms was first reported in 2003. The discovery of large out-of-plane MAE of 9.3 meV in single Co atoms adsorbed on Pt(111) [23] is the seminal work which paved the path for the extended research on single adatoms in the following years. Being largely driven by the search of magnetic stability in these systems, soon it became crucial to understand the origin of their magnetic anisotropy and the physics behind their fundamental magnetic properties. So far, the $3d$ transition metals (TM) have been the most studied elements in this respect [24–32], culminating in the ultimate experimental realization of the largest possible MAE in single Co atoms adsorbed on MgO/Ag(100) [33]. However, despite the large magnetic anisotropy, the spin relaxation time T_1 has only been limited to $\approx 200\ \mu$s. For Fe atoms adsorbed on the same surface, this increases up to ≈ 10 ms [34]. Longer T_1 time is unlikely to be achievable from the TM elements since their $3d$ electrons are prone to hybridize with the atoms of the surrounding ligands and thereby are intrinsically more sensitive to external perturbations. The use of $4f$ lanthanides is a better alternative as we are going to argue in the following section. Therefore, with the aim of achieving single-atom-bit with longer magnetic lifetime, the attention is now moving to these elements.

1.1.2 Magnetism in rare earth single atoms and atomic scale clusters

The term RE is used in this thesis for calling the fourteen different lanthanides conventionally starting with Ce. Magnetism in these REs stems from the unpaired electrons in the $4f$ orbitals. The large atomic numbers of these elements create a strong coupling between the spin (S) and orbital moment (L) which outweighs the strength of the CF [35]. The spin-orbit coupling

(SO) in REs is at least an order of magnitude larger compared to the case of conventional $3d$ materials. This makes the total magnetic moment $J = L + S$ a good quantum number. Again, this is a stark contrast with the conventional $3d$ elements whose L moment is usually quenched by the ligand field (LF), unless a very specific bonding geometry is designed [32, 33]. Moreover the strongly localized nature of the $4f$ electrons inhibits their direct hybridization with the substrate or surrounding atoms, thus allowing them to preserve most of their atomic character. Altogether this renders the $4f$ elements one of the most appealing candidates for studying quantum magnetic properties in low dimensional systems.

The magnetism of RE clusters was first brought into attention by Schuh *et al.* in 2012 [36]. They reported some inelastic features from the scanning tunneling spectroscopy (STS) on Gd atoms and dimers adsorbed on metal substrates. These excitations were interpreted to arise from transitions between magnetic quantum levels (spin-excitation), albeit without the proof of magnetic field (B) dependence in such excitations. In the following year Ho adatoms on Pt(111) was studied by Miyamachi *et al.* [37]. They reported similar inelastic features and telegraphic signals which were interpreted to characterize the orientation of the Ho moment as probed by a spin-polarized tip (SP-tip). From the telegraphic signals, the Ho adatoms were interpreted to have a magnetic lifetime of $\approx$ 400 s at 0.7 K. However, this also lacked several control measurements. For instance, the B field dependence in the observed inelastic excitation and measurements with a non SP-tip were not shown.

Thanks to those inadequacies, these works arouse further scientific questions and debates. In fact, whether magnetic stability is possible to achieve from RE atoms directly adsorbed on metal substrate, is the very question that initiated this thesis work. In the following we will focus on the main objectives and briefly explain the overall organization of the thesis.

1.2 Objectives and outlines of this thesis

The principal aim of this thesis is to identify the fundamental handles for controlling the magnetic properties in surface-supported single RE atoms. In particular we want to address the following questions:

- What are the effects of adatom-substrate interaction on the magnetic properties of isolated single RE atoms and adatom-adatom interaction in case of RE clusters?
- Can these be optimized to achieve the desired properties? *e.g.*, the $4f$ occupancy in the REs, the orientation of the easy axis, amount of magnetic anisotropy etc.
- Can we combine these knowledge to achieve long magnetic lifetime in surface-supported RE single atoms, molecules or atomic scale clusters?

Our studies involve a combination of the following experimental tools:

- spatially averaging, element specific XAS and XMCD, which allow quantitative measurement of the magnetic moment, its preferred orientation, and the anisotropy energy.

- spatially resolving STM measurements, which allows topography with atomic precision along with local spectroscopic investigation on different individual magnetic entities. Therefore it is used to complement the knowledge gained from XAS and XMCD.

In Chapter 2 we will first introduce these experimental techniques in detail along with the description of the few theoretical tools used in this work.

Chapters 3, 4, 5, and 6 are dedicated to elaborate the experimental results. Chapter 3 starts with the investigation of adatom-substrate interaction by exploring the magnetic properties of several RE atoms adsorbed on different metal substrates. None of them exhibit magnetic stability. However, this detailed survey allows us to gain important insights about how to control the $4f$ occupancy and related magnetic properties in surface-supported RE atoms.

Chapter 4 is focussed on Er atoms and small clusters adsorbed on Cu(111). This novel system allows us to learn how the electrostatic interaction between the adatoms can play an important role (a) in modifying the orientation of magnetic easy axis and (b) in promoting magnetic stability in surface-supported few-atom clusters of REs.

To expand the knowledge of adatom-adatom interaction, we have further investigated the magnetic properties of RE-TM heterodimer. Chapter 5 introduces this novel system: Ho-Co adsorbed on thin insulating layers of MgO grown on Ag(100). We will demonstrate the very first evidence of spin-excitations in these RE-TM heterodimers. Moreover, we will describe how to identify the origin behind the observed spin-excitations using an effective spin-Hamiltonian model based on density matrix formalism.

In Chapter 6 we will be briefly focussed on few other projects in which I was involved during this PhD in parallel with the mainstream projects mentioned above. The overall conclusions and future perspective will be presented in Chapter 7.

2 Methods

2.1 Experimental

2.1.1 Sample preparation

Handling of the rare earths

Rare earths are highly reactive and are prone to oxidation. Most of them are also hazardous for health [38]. Therefore they need to be treated very carefully. High purity (99.9%) rods of specific REs (Dy, Ho, Er, and Tm) used in this work were delivered in a vacuum sealed package from *GoodFellow*. As a first step, these rods are cleaned by scratching off the oxidized surface layer, if any, until a shiny metallic part is obtained. To limit the direct exposure to these REs, this step is performed in a fume hood equipped with a proper ventilation system. In order to minimize their exposure to ambient conditions, the RE rods are then immediately placed into the electron-beam evaporator. Following this, the evaporator is baked up to 150°C for about 48 hours. Finally, to ensure purity of our samples all rods were well degassed for several days. The degassing was terminated when no further change in the base pressure was observed after switching on or off the e-beam evaporator.

For the XMCD measurements, the RE rods were transported in a vacuum suitcase from EPFL to the X-Treme beamline of the Swiss Light Source [39]. Before using them in our XMCD experiments, we always used the above mentioned cleaning and degassing protocol.

Preparation of the metal substrates

The following single crystalline substrates have been used in this thesis: Pt(111), Cu(111), Ag(100), and Ag(111). These were prepared using several Ar^+ ion sputtering and annealing cycles, according to the specific annealing conditions required for the different crystals as mentioned in references [40, 41]. Clean substrates were transferred from the preparation chamber to the measurement chamber without breaking the vacuum.

Preparation of MgO on Ag(100)

MgO was grown by evaporating Mg from a Knudsen cell onto a clean Ag(100) substrate in a background oxygen pressure of 1×10^{-6} mbar. Prior to this preparation, the Mg source was thoroughly degassed. For each sample, stepwise degassing was done under the following conditions: (a) at least 30 minutes at 280°C without water cooling, (b) ≈ 15 minutes at 350°C, (c) ≈ 15 minutes at a temperature that is 20°C higher than the deposition temperature, and (d) ≈ 15 minutes at the deposition temperature (≤ 400°C). The last three steps were performed while the Mg source was water cooled. During the preparation of MgO the Ag(100) crystal was maintained at its annealing temperature (773 K). After the preparation the shutter of the Mg source was closed while the Ag(100) surface was allowed to cool down to room temperature. The temperature of Ag(100) during deposition and the speed of its post-deposition cool down determine the thickness of MgO.

Deposition of single atoms

For all XMCD samples, the substrates were kept at a temperature of 4 K during deposition of the atoms, in order to suppress diffusion-induced nucleation. This way only statistical nucleation is viable and cluster formation is negligible below 0.02 ML [42]. To ensure purity of the XMCD samples, (a) the depositions were made at a very good base pressure ($\leq 4 \times 10^{-11}$ mbar), (b) the cryostat was equipped with a non-emitting getter to minimize the hydrogen content in the residual gas, and (c) measurements for each XMCD sample lasted no longer than 5 hours to limit the exposure to residual vacuum contaminants. The RE coverage of each sample is defined in terms of monolayers (ML) where one ML describes one adatom per substrate atom (see section 2.1.3 for calibration of RE coverage). The desired coverage of the RE is achieved by carefully controlling the deposition flux and time.

The samples measured with low temperature (LT) STM were prepared following similar strategy. However there are subtle differences. In particular, the base pressure during deposition was about 3×10^{-10} mbar and the sample temperature was maintained at 4 K for most of the measurements, except a few samples of Er/Cu(111) for which the deposition was made at 10 K as mentioned in section 4.2.

Machine specifications

The XAS and XMCD measurements presented in this work, were performed with circularly polarized x-rays at the EPFL/PSI X-Treme beamline of the Swiss Light Source [39] (Figure 2.2). The XMCD measurement chamber is equipped with a variable temperature insert allowing measurements between $2-300$ K with an out-of-plane magnetic field of -7 to $+7$ T and in-plane field of -2 to $+2$ T. The preparation chamber has standard sputtering and annealing facilities for *in situ* sample preparation. The end station is built at Paul Scherrer Institute (PSI) in close collaboration with the LNS group at EPFL [39].

The LT-STM measurements were carried out using two different set ups. The measurements of Er/Cu(111) for deposition at 10 K (section 4.2) were done in a home-built ultrahigh vacuum (UHV) LT-STM operating at 5 K (without any magnetic field), under the supervision of Dr. Marina Pivetta [43]. The rest of the STM measurements presented in this thesis have been performed under the supervision of Dr. Fabio Donati using a home-built UHV LT-STM, equipped with −8.5 T to +8.5 T magnetic field oriented normal to the surface and −0.8 T to +0.8 T magnetic field along one of the in-plane directions. This machine is based on a commercial single-shot ^{3}He-^{4}He cryostat allowing utmost 15 hours of measurement time at 0.4 K. Measurements can be also performed at 4 K when the gaseous ^{3}He provides thermal contact to the ^{4}He bath. The design of this machine was conceived jointly by Prof. Harald Brune and Prof. Pietro Gambardella. It was built at EPFL-LNS laboratory by Dr. Laurent Claude and Prof. Pietro Gambardella [44, 45].

2.1.2 X-ray absorption spectroscopy and x-ray magnetic circular dichroism

Working principles

XAS and XMCD are versatile tools for measuring magnetic properties of matter in an element specific manner. They can be considered as one of the most important photon-in-electron-out processes that is routinely used for studying magnetic properties of materials adsorbed on surface. Essentially these are spectroscopic techniques in which the energy of the incident x-ray is varied in order to match a specific electronic transition of the element under investigation. In other words, an x-ray photon is absorbed when a core electron is excited to an unoccupied valence band (Figure 2.1 a). A core hole (defined as "absence of electron") is created in this process which is subsequently filled via a cascade of Auger processes. The amount of primary Auger electrons that is produced is a direct measure of the absorption strength. The primary electrons further create secondary scattered electrons, which is what is measured in Total Electron Yield (TEY) mode. Typically the electron yield signals are obtained by measuring the drain currents as shown in Figure 2.1 b. TEY is a surface sensitive measurements since the electrons that are produced deep inside the material do not have enough energy to surpass the workfunction of the sample and therefore they will not contribute to the total signal. All XAS and XMCD works presented in this thesis were performed in TEY mode. The typical sampling depth in such mode is a few nanometers.

We will limit the discussion of XAS and XMCD to the $M_{4,5}$ edge of the RE materials since this is the main focus of this thesis. The corresponding electric dipole transition occurs from the $3d$ core level to the unoccupied $4f$ level (Figure 2.1 a). For the REs discussed in this thesis, the incident x-ray energies lie within 1000 – 1500 eV in this absorption edge. Note that these measurements require an x-ray source that is highly intense, collimated, polarized, and has the possibility of tuning the photon energy to any selected wavelength in the range of interest. Obtaining all of these qualities are not possible from usual laboratory sources. Synchrotron facilities are developed for conducting such demanding measurements around the globe.

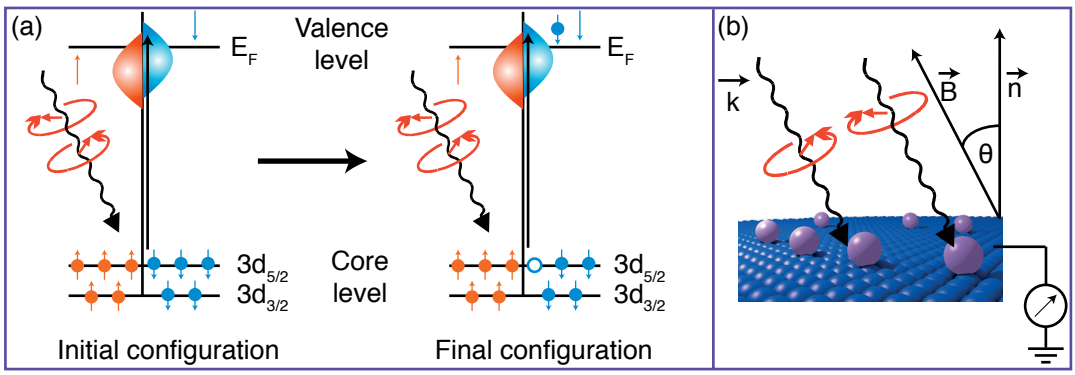

Figure 2.1: (a) Schematic explaining the basic principle behind XAS and XMCD. These are photon-in-electron-out spectroscopic techniques. XAS is defined as the total absorption from the two circular polarizations while XMCD is the dichroic signal obtained from the difference in the absorptions. (b) Illustration of the experimental set up. The adatoms are shown as purple spheres.

XMCD is only one branch of multidimensional use of synchrotron facilities. Interested readers may refer to [46, 47] for gaining further insights about various other x-ray based measurement techniques, as well as for a detailed account of the theoretical basis of XAS and XMCD.

All x-ray absorption spectra were normalized with respect to the total flux of incident x-rays measured using a metal grid. These spectra were further normalized with respect to the absorption pre-edge, in order to discard spurious effects due to different TEY at different angles of incidence. All XAS and XMCD spectra were measured at an external magnetic field of $B = 6.8$ T (unless otherwise specified) at $T = 2.5$ K, and in UHV ($P_{cryostat} \leq 3 \times 10^{-11}$ mbar).

Experimental geometry

In our experimental set up, the magnetic field was always collinear with the incident x-rays ($\hat{B} \parallel \hat{k}$). To identify the magnetic easy axis and to quantify the MAE, we rotated the sample around an axis perpendicular to the field and beam, and acquired XAS and XMCD spectra at two incident angles, namely, normal, $\theta = 0°$, and grazing, $\theta \neq 0°$, where θ defines the angle between $\hat{B}$ (or $\hat{k}$) and the surface normal $\hat{n}$ [39] (Figure 2.1 b).

Magnetization curves

Magnetization curves were recorded by mapping the maximum XMCD of the M_5 edge as a function of B, normalized by the corresponding pre-edge of the XAS signal. Note that, apart from the contribution of the M_4 edge, this signal is proportional to the total magnetic moment per atom. Therefore, we normalized the magnetization curves obtained from the two angles of incidence such that their ratio at 6.8 T equals the corresponding ratio of the total moments

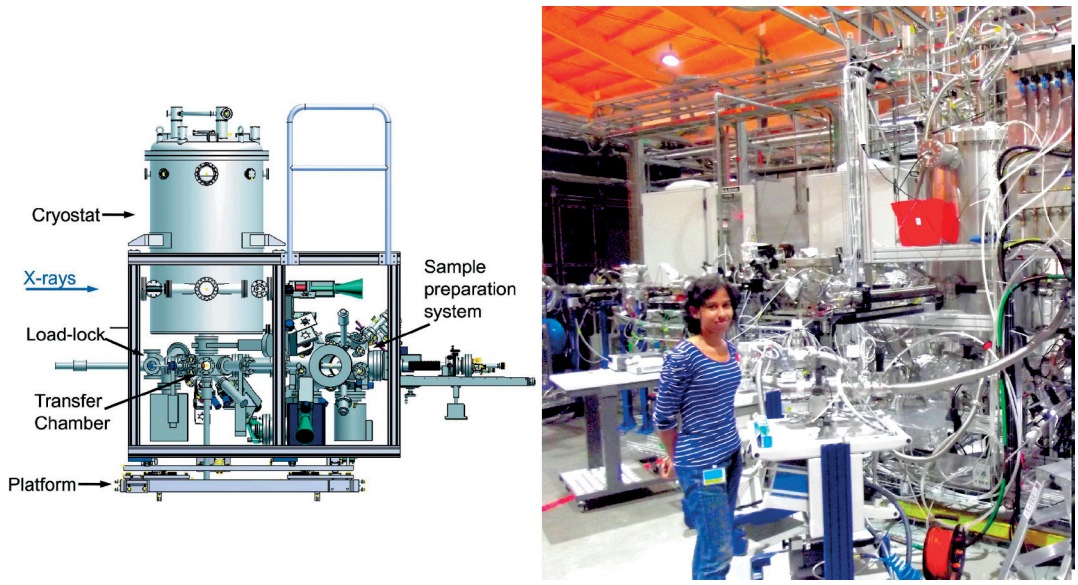

Figure 2.2: (left) The schematic of the X-Treme end station at Swiss Light Source (SLS), Paul Scherrer Institute (Switzerland) taken from ref. [39] and (right) its physical picture. All XAS and XMCD measurements reported in this thesis on single rare earth (RE) atoms adsorbed on metal substrates were performed in this beamline.

obtained by applying sum rules on the XAS and XMCD spectra for the entire $M_{4,5}$ range [48, 49]. For the measurements reported in Chapter 3 and 4, a sweep rate of 12.5 mT/s and photon flux of 2×10^{10} photons mm^{-2} s^{-1} were employed.

Analysis of XAS and XMCD data

To isolate the signal of the RE adatoms from the background of the corresponding substrate, XAS spectra of the clean surface were subtracted from the overall XAS signature. Figure 2.3 illustrates the steps involved in the analysis of the raw XAS and XMCD data, for an example case of Er adatoms adsorbed on Cu(111) substrate. The XAS for both circular polarizations were obtained at the $M_{4,5}$ edge of Er before and after the deposition of Er. The former was used as the background (top spectra of Figure 2.3 a) which was subtracted from the latter (middle spectra of Figure 2.3 a) in order to obtain the signal coming from Er only. These background corrected spectra (bottom spectra of Figure 2.3 a) were used to calculate the total absorption signal XAS, which is the sum of the absorption of the two polarizations, and the dichroism XMCD, that comes from the difference. Finally, XMCD sum rules were applied on such spectra (top and bottom spectra of Figure 2.3 b). To discard any spurious contribution from the unwanted regions, we chose only the regions marked with dashed boxes centered around the M_5 and M_4 edges for calculating the sum rules (Figure 2.3 b).

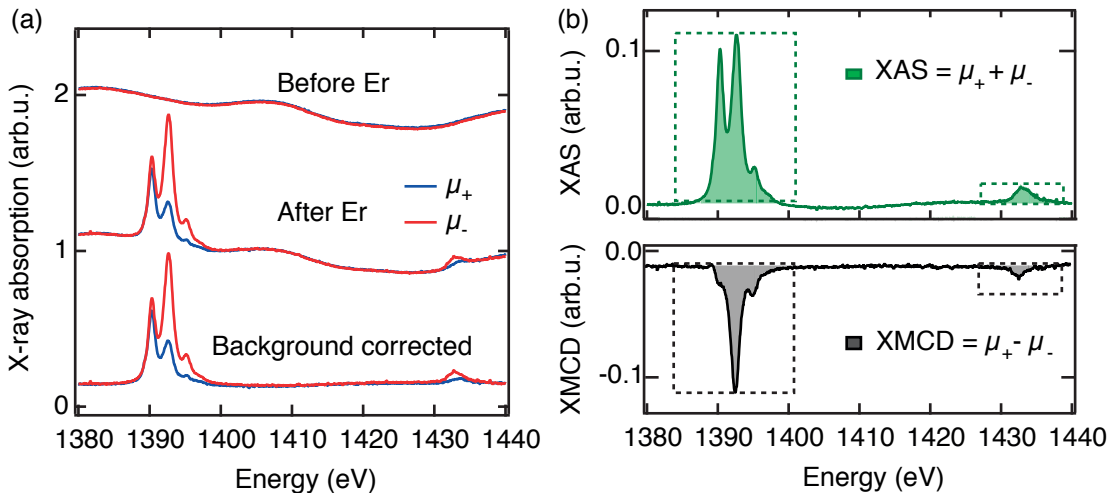

Figure 2.3: A typical example of XAS and XMCD spectra of Er adatoms on Cu(111). (a) XAS for both circular polarizations (μ_+ and μ_-) at Er $M_{4,5}$ edge obtained before (top) and after (middle) the deposition of Er. Respective background corrected spectra are shown at the bottom. All spectra are offset for clarity. (b) XAS and XMCD signals obtained from the sum (green) and the difference (grey) of the absorptions of the two polarizations. Respective boxes with dotted borders indicate the regions within which the spectra were integrated in order to apply the sum rules.

XMCD Sum rules

Sum rules are unique tools for relating the XAS and XMCD signals to the ground state expectation values of effective spin $\langle S_{eff}\rangle$ and orbital $\langle L_z\rangle$ magnetic moments [48, 49]. The effective spin moment $\langle S_{eff}\rangle$ contains information about the expectation value of the spin-dipole $\langle S_z\rangle$ and spin-quadrupole $\langle T_z\rangle$ terms. Here z refers to the field (and beam) axis. The relevant equations for the evaluation of orbital and spin sum rules of the REs are as follows:

$$\langle L_z\rangle = 3\frac{h_n X_{4,5}}{I} \tag{2.1}$$

$$\langle S_{eff}\rangle = 2\langle S_z\rangle + 6\langle T_z\rangle = 3h_n\frac{5X_5 - 3X_{4,5}}{I} \tag{2.2}$$

where $h_n = 14 - n$ defines the number of holes in the $4f$ shell with n occupancy, $X_{4,5}$ = the XMCD integrated over the entire $M_{4,5}$ edge, and X_5 = the XMCD integrated only under the M_5 edge [49]. The normalization is performed with respect to the unpolarized absorption signal

defined by

$$I = \int_{\omega} (\mu_0(\omega) + \mu_+(\omega) + \mu_-(\omega))\, d\omega \tag{2.3}$$

where ω is the incident photon energy and $\mu_+(\omega)$, $\mu_-(\omega)$, and $\mu_0(\omega)$ represent the absorption signals with circular plus, circular minus, and linear polarizations respectively [46]. While the first two components are readily available the last one was impossible to obtain experimentally with the given set up since it required the photon $\hat{k}$ vector to be perpendicular to the surface normal $\hat{n}$, a geometry in which no signal can be detected from the sample. For simplicity and under the assumption of isotropic absorption, the following approximation is commonly adopted:

$$\begin{aligned} &\mu_0(\omega) = \frac{1}{2}(\mu_+(\omega) + \mu_-(\omega)) \\ &\implies I = \frac{3}{2}\int_{\omega} (\mu_+(\omega) + \mu_-(\omega))\, d\omega \end{aligned} \tag{2.4}$$

We have considered the sum rules with this assumption everywhere except for estimating the spin-quadrupole component $\langle T_z \rangle$ in Chapter 3. For the latter we used multiplet analysis to calculate the contribution of $\mu_0(\omega)$ and used the resulting I (equation 2.4) for precisely determining the magnetic moments of the free atoms (see section 3.3.1).

The projected total magnetic moment $\langle J_z \rangle$ is expressed as $\langle S_z \rangle + \langle L_z \rangle$. While $\langle L_z \rangle$ can be directly derived from sum rules, $\langle S_z \rangle$ needs to be extracted from $\langle S_{eff} \rangle$. For this purpose, we have assumed that the ratio of $\langle T_z \rangle / \langle S_z \rangle$ does not change upon surface adsorption, *i.e.*, it remains the same as in the case of gas-phase atoms [40]. This assumption is justified for REs since their SO coupling is much stronger than the strength of the CF, which forces the L moment to remain strongly aligned with the S. Given this assumption, we can first obtain $\langle T_z \rangle_{free} / \langle S_z \rangle_{free}$ from the multiplet calculations of the free ions (see section 3.3.1) and further we can extract $\langle S_z \rangle$ from the following expression:

$$\langle S_z \rangle = \frac{\langle S_{eff} \rangle}{2 + 6\frac{\langle T_z \rangle_{free}}{\langle S_z \rangle_{free}}} \tag{2.5}$$

Here the subscript *free* denotes values obtained from multiplet calculation of gas-phase atoms and $\langle S_{eff} \rangle$ is obtained by applying the sum rules on the measured spectra.

2.1.3 Scanning tunneling microscopy (STM)

Since its discovery in 1986, Scanning tunnelling microscopy (STM) has unravelled a whole new world of atomic-scale imaging, spectroscopy, and manipulation to the surface science community. When integrated with cryogenic systems, STM can offer the exclusive freedom to study local electronic and magnetic properties of materials to an unprecedented energy resolution. A complete overview of STM is beyond the scope of this chapter. In the following we will mainly focus on the working principle of STM and describe the most commonly known measurement modes. However, interested readers may refer to [50] for a detailed overview on the subject.

Working principles

Before discussing the underlying theory of STM, we will first describe the principal ingredients of an STM. STM is generally done on two-dimensional surfaces of interest. One of the most crucial ingredients for doing STM is the probe tip. All the STM measurements shown here are performed with a tungsten (W) tip. The tip was prepared *ex situ*, by etching in NaOH solution from a bulk tungsten wire. Later it was introduced in UHV. In order to make an atomically sharp tip, usually the end of the tip is "gently crashed" on a flat terrace or step edges of the metal substrate under investigation. The second most important component is the piezoelectric stack comprising of three mutually perpendicular piezoelectric transducers (x, y, and z). Depending upon the design, either the tip or the substrate can be mounted on such piezoelectric stack. Piezoelectric materials contract or expand depending upon the applied voltage, solving the purpose of scanning over the surfaces of interest. Note that in the normal tunneling condition, the tip is never in physical contact with the surface and yet one can record a tunneling current that flows through the junction. The underlying physical mechanism can be mathematically modelled only using a quantum mechanical description (see section 2.1.3 and references [50, 51]).

The next important part is the feedback loop. STM can work in both (i) constant current, (ii) constant height mode. The first is usually adopted for topography. In order to maintain a constant tunneling current while scanning across a region of interests, the tip height needs to be adjusted. Feedback loop does this job by correcting for the minuscule differences in the voltage output of the piezodrive by comparing it with the demand set-point. The error signal is therefore the difference between I_{set} and the instantaneous signal before correction brought by the changes in vertical tip-to-surface distance owing to the atomic scale corrugations. Figure 2.4 shows the simplest illustration of the above mentioned circuit. Relevant information on the circuit design can be found in [52].

The constant height mode can be used if the surface is atomically flat. Otherwise there is a risk of crashing the end of the tip against the uneven surface. However this mode (equivalent to an "open" feedback loop condition) is used during scanning tunneling spectroscopy (STS) measurements, in which the tip needs to be stabilized at a certain vertical distance from the

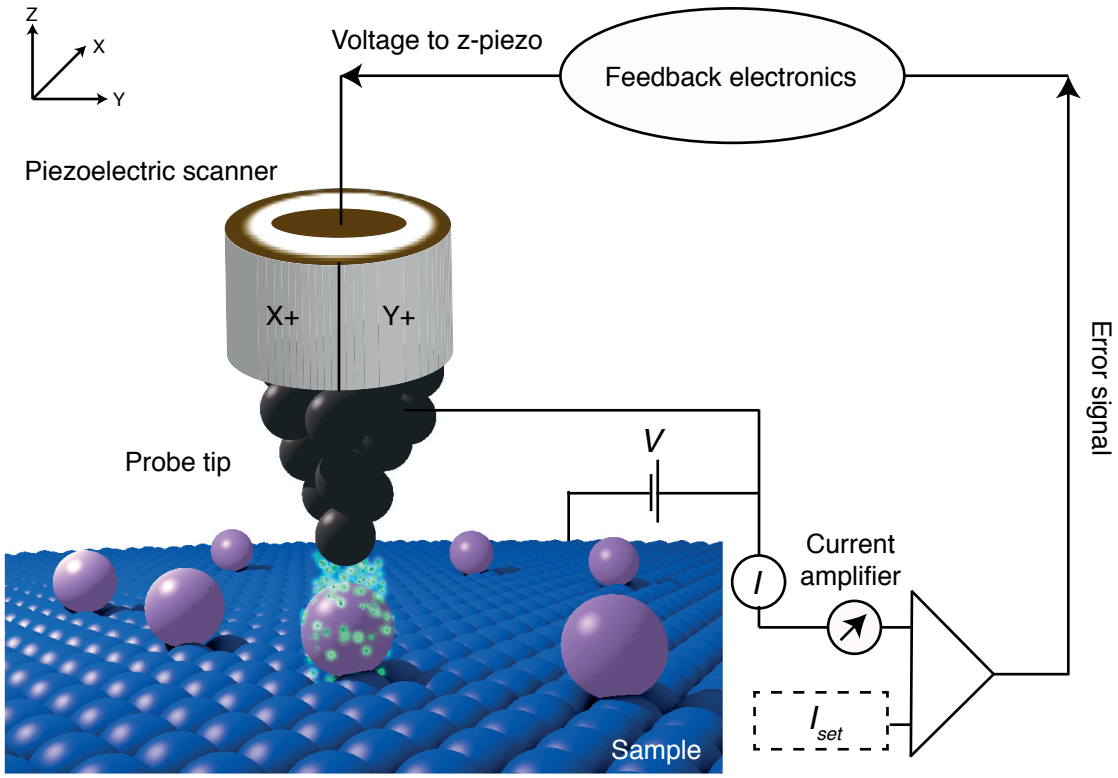

Figure 2.4: Schematic showing the important parts of an STM *i.e.*, probe tip, sample, feedback circuit, piezoelectric scanner, and a current amplifier.

surface by applying the desired tunneling set points. Then a voltage ramp is performed while the feedback loop stays inactive. This is required so that the tip height remains unchanged during the acquisition of the entire spectra.

Final important component is the current amplifier. This is necessary for converting the tunnelling current I_t into a voltage output that can be handled easily. Sometimes the measurements are so sensitive that only a very small I_t in the range of pA can be applied. This necessitates a large amplification of the current signal as well as low noise in the output. Moreover there might be cases where a large set-point of 100 nA is required in order to maintain the desired vertical tip-to-surface distance. In this case the current amplifier is required for having the flexibility of applying large set-point without an overflow.

Theoretical insights: tunnelling is a quantum mechanical process

At the heart of STM lies the principle of quantum tunneling of electrons across a classical barrier. This concept holds only in quantum regime and it explains the ability of a quantum object to be present in a classically forbidden region. Mathematical description on this topic can be found in most text books of quantum mechanics. Therefore we will skip the

detailed theoretical description and will only touch upon the basic equations that define the measurable quantities in an STM, *e.g.* tunneling current and local density of states (LDOS).

The excellent atomic resolution of an STM arises from the strong exponential dependence of the tunnel current on the vertical distance between the tip and the sample. The simplest theory of STM was first provided by Bardeen [51] in which the tip and the sample are considered as two electrodes separated by an insulating barrier of height U_{gap} (for instance vacuum gap in case of an UHV STM). The wavefunctions of an electron from the tip and sample are expressed as Ψ_T and ΨS respectively. The tunneling probability of an electron from the tip with energy E^T to an unoccupied state of energy E^S of the sample can be expressed by using Fermi's Golden Rule:

$$P(t) = \frac{2\pi}{\hbar}\delta(E^S - E^T)|M^2| \tag{2.6}$$

where M is the tunneling matrix element defined as:

$$M = \langle \Psi^T | \, U_{gap} \, | \Psi^S \rangle \tag{2.7}$$

Here the presence of the Dirac delta function ensures that tunneling occurs only if the energy of the initial and final state are matched. This is the case for elastic tunneling. It is possible to explain the inelastic tunneling with an extended theory. We will briefly discuss about inelastic tunneling in the next section. However, interested readers may refer to [53] for the detailed theoretical description of these.

The tunneling current can be expressed as:

$$I_t = \frac{4\pi e}{\hbar}\int_{-\infty}^{\infty} \rho_S(E_F - eV + \epsilon)\rho_T(E_F + \epsilon)(f(E_F - eV + \epsilon) - f(E_F + \epsilon))|M^2| d\epsilon \tag{2.8}$$

where V is the applied voltage. The quantity $f(E)$ is the Fermi-Dirac distribution function defined at energy E as:

$$f(E) = \frac{1}{1 + e^{(E-E_F)/k_B T}} \tag{2.9}$$

The quantities ρ_T and ρ_S define the density of states (DOS) of the tip and sample, respectively.

In the limit of very low temperature (close to zero Kelvin), $f(E)$ reduces to a step function. Moreover if the applied bias is small enough, $|M|$ can be considered as a constant. Under these approximations the expression for I_t simplifies to the following:

$$I \propto \int_0^{eV} \rho_T(\epsilon + E_F)\rho_S(\epsilon + E_F - eV)d\epsilon \tag{2.10}$$

where the energy at the Fermi level E_F is specified to 0. In summary, equation 2.10 states that I_t is the measure of total integrated DOS from the Fermi level to the chosen set-point bias V.

Another important measurable quantity is the differential conductance which is measured during STS and this can be expressed as:

$$\frac{dI}{dV} \propto \rho_T(E_F)\rho_S(E_F - eV) \tag{2.11}$$

This is a measure of local DOS (LDOS) as a function of energy V at a predefined spatial position (x, y), albeit convoluted with the DOS of the tip. Therefore STS measurements provide a direct access to the LDOS of the sample.

Inelastic electron tunneling spectroscopy (IETS)

So far we have considered only elastic processes (recall the presence of the Dirac delta function in equation 2.6). For elastic tunneling, it can be shown that the tunneling current I_e is linearly proportional to the tunnel voltage V. Inelastic processes can occur when the tunneling electrons arrive at the junction with sufficient kinetic energy eV such that they can trigger some internal (de)excitation in the adsorbate, *i.e.*, $eV \geq E_i$, where E_i denotes the characteristic energy needed to trigger the inelastic process (Figure 2.5 a). Such inelastic processes can be, for instance, (de)excitation of a vibrational mode in a molecule, or a magnetic (de)excitation in an atom. Since these inelastic processes act as additional means of (de)exciting the atom/molecule in the tunnel junction, on top of the already existing elastic processes, a sudden change of slope can be detected in the usual $I-V$ curve at the characteristic energy E_i, as depicted in Figure 2.5 b. The occurrence of the inelastic processes can be easily detected from the symmetrically positioned steps in the dI/dV spectra, which result in a pair of peak-dip feature in the corresponding d^2I/dV^2 spectra (Figure 2.5 c).

As the tunneling currents are usually very small, the inelastic features can be too weak to detect from the change of slope in the $I-V$ curve. Moreover the numerical derivation of the current signal might suffer from the so called $1/f$ (Schottky) noise [53]. Therefore Lock-in detection is employed to ease such measurements. For the Lock-in detection, the voltage is modulated

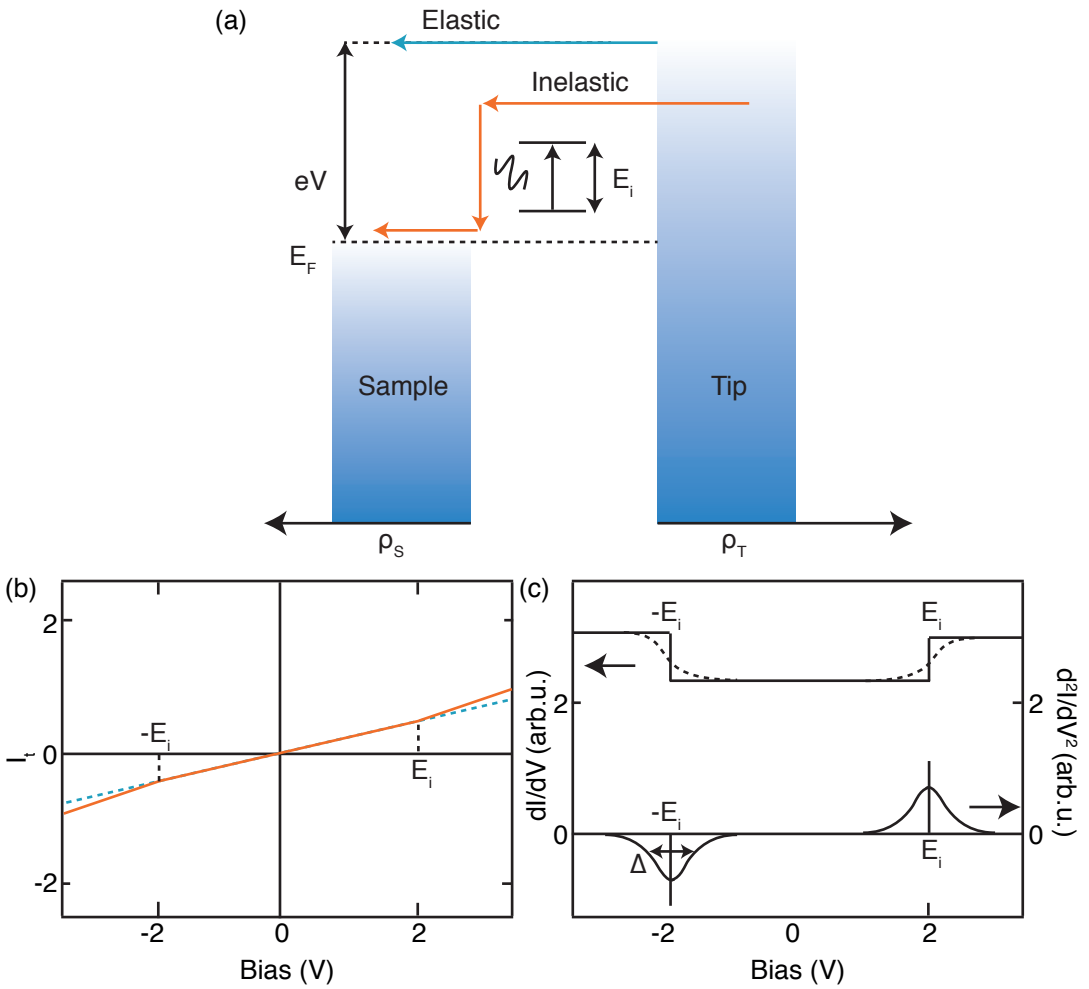

Figure 2.5: Adapted from ref. [53]: a schematic illustrating the (a) elastic (in cyan) and inelastic tunneling (in orange) processes and (b) the appearance of a typical $I-V$ curve indicating an inelastic process (in solid orange line) occurring at an energy $\pm E_i$. (c) The inelastic process can be detected from the symmetrically positioned step-like features of the dI/dV spectra, and the typical peak-dip features in the d^2I/dV^2 spectra. Both dI/dV and d^2I/dV^2 features are broadened (dotted curves) due to the intrinsic lifetime of the excited state, the finite measurement temperature, and the amplitude of the Lock-in modulation.

at a given frequency ω_m. The frequencies which are multiples of the main-line frequency (*e.g.* 50 Hz for Europe) have to be avoided in order to reduce the electrical noise. The output of the Lock-in signal which is frequency-locked with the reference signal at ω_m, is directly proportional to dI/dV with a high degree of accuracy. Note that the steps in the dI/dV and the peak-dip features in the d^2I/dV^2 signals can be broadened, as depicted schematically in Figure 2.5 c, due to (a) the intrinsic lifetime of the excited state, (b) the finite measurement temperature, and (c) the modulation amplitude introduced in the Lock-in detection technique. A highly illustrative mathematical description on the Lock-in detection as well on IETS

measurements can be found in ref [53].

In this thesis, STM has been used as both topographic as well as spectroscopic tool. We will present LT-STM measurements (0.4 and 4 K) in the relevant sections. In the following section we will describe how the information obtained from the LT-STM can be used to calibrate the coverage of all the RE samples.

Calibration of rare earth coverage

All coverages reported in this thesis are in units of ML, expressed as the number of RE adatom/substrate atoms. The covalent radius of the late lanthanides significantly exceeds the one of the TM substrates and the difference increases while moving from $5d$ to $3d$ metals. This implies that the REs cannot be packed with the same density imposed by the substrate. The corresponding packing factor needs to be taken into account for reporting the RE coverages in MLs. In the following paragraphs we will describe how to derive this packing factor and establish the coverage calibration. This calibration has been used for reporting all coverages in Chapter 3 and 4.

For all XMCD measurements, a variable temperature STM attached to the X-treme end station was used to map the area of the substrate covered by the RE islands for ≈ 0.5 ML sample at room temperature (RT). Subsequently, we measured the total XAS integral in order to correlate the XAS edge with the amount of RE present in the sample, as measured with the RT-STM in the previous step.

In order to understand how this compares with the coverage measurements done with a typical low temperature STM, we investigated several sub-ML coverages of Er on Cu(111). These coverages (Θ) can be easily calculated knowing the numbers of different oligomers of Er (single atoms, dimers, trimers, and so on) from apparent height histograms. Figure 2.6 a shows an example of such histogram extracted from an STM image using our home-made image analysis software (Simple, version 3.3) that identifies the atoms as protrusions and evaluates their apparent height with respect to the surrounding terrace. One clearly discerns three apparent height classes corresponding to monomers ($N = 1$), dimers ($N = 2$), and clusters larger than dimers ($N \geq 3$). Moreover, the shape analysis (as described in section 4.5.1 and illustrated in Figure 4.8 a) allows us to distinguish and therefore to quantify the densities of differently sized clusters corresponding to the $N \geq 3$ peak. With this, we measured the coverage of Er (defined as Er atoms/substrate atom) for all samples within 0.02 ML$\leq \Theta \leq$ 0.06 ML. We further established the calibration curve between the measured coverages and the deposition time as shown in Figure 2.6 b. This allows us to extrapolate the coverage for samples with $\Theta <$ 0.02 ML, where imaging of the monomers is very challenging due to their high mobility on the surface. The same was applied for $\Theta >$ 0.06 ML, where the presence of larger clusters prevents a direct coverage determination.

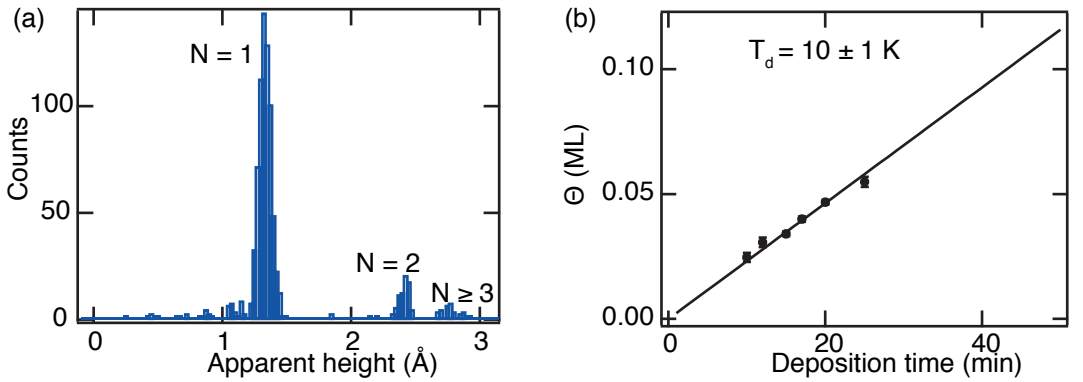

Figure 2.6: (a) Apparent height histogram of the Er related protrusions obtained from a 0.032 ML sample. (b) Coverage as a function of deposition time. T_d defines the deposition temperature. Dots: measurements, solid line: linear fit providing $F = (2.30 \pm 0.03) \times 10^{-3}$ ML/min and allowing extrapolation of the coverage for $\Theta < 0.02$ ML and $\Theta > 0.06$ ML.

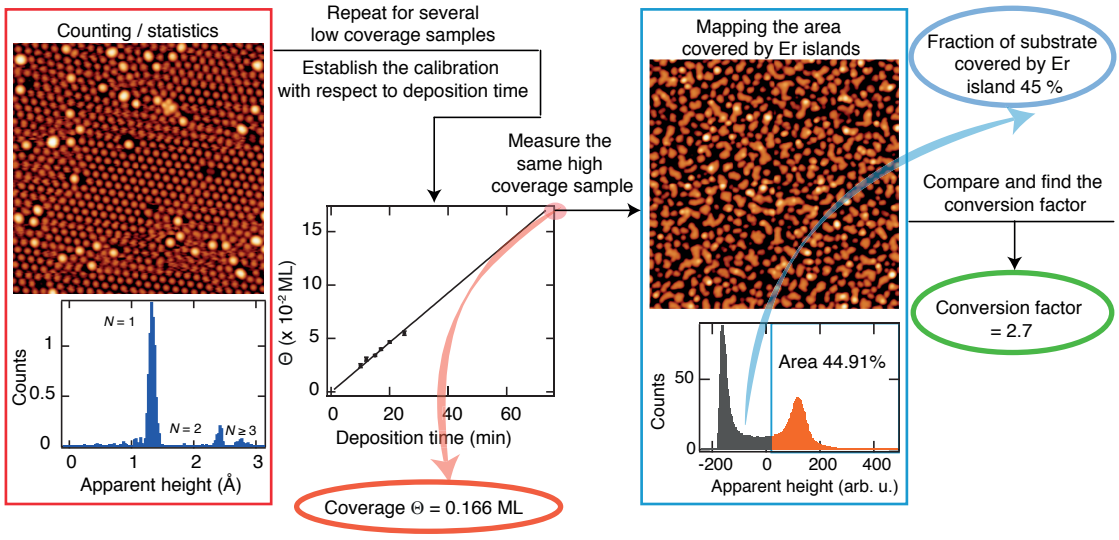

Figure 2.7: Schematic illustrating the method used for the calibration of the RE coverages. The left part shows how using LT-STM we establish the coverage calibration curve. This is detailed in Figure 2.6 and in the text. Further we use the calibration curve for correlating the coverages measured using a RT-STM.

Further to this, we prepared a sample with 0.17 ML coverage, where the coverage is determined through extrapolation, knowing the deposition time and the linearity relation established in the previous step (Figure 2.6 b). However, STM measurements show that 45% of the surface is covered by Er islands (Figure 2.7). This area is large by a factor of 2.7 compared to what is expected from the linear extrapolation for the coverage. We ascribe this difference to the significant mismatch in the covalent radius of Er and Cu, as mentioned in the beginning of this section. Therefore, we rescale the coverage-equivalent obtained from combining the XAS and RT STM measurements, by the packing factor of 2.7 to take this mismatch into account.

Note that this calibration method assumes flat lying geometry for all clusters.

In order to evaluate the coverage of RE atoms adsorbed on a different substrate we should also consider the difference in the lattice constants in addition to the previously determined packing factor of 2.7. For instance, for an identical XAS integral for Er on Cu(111) and on Pt(111) the effective packing factor on Pt(111) will be $2.7 \times (0.256/0.278)^2 = 2.3$, since the unit shell size of Cu(111) and Pt(111) are 0.256 nm and 0.278 nm respectively. In addition, we corrected for the different attenuation factors of the different substrates which affects the XAS pre-edge values. In case of a different RE, we also considered the change in the number of holes in the $4f$ shell since this directly affects the total absorption signal. The coverages reported in Chapter 3 and 4 include all these relevant factors.

2.2 Theoretical

2.2.1 Mean-field nucleation theory

The mean-field nucleation theory (MNFT) has been employed in order to characterize the coverage dependent growth of Er on Cu(111) in Chapter 4. This model can describe the density of differently sized clusters on the surface with the help of coupled differential equations (equation 2.12). Such rate equations for describing the growth model was first introduced by Zinsmeister [54, 55]. Excellent overview including several examples of implementing MNFT using the rate equations can be found in [56, 57].

$$\begin{aligned}
\frac{dn_1}{dt} &= F - 2\sigma_1 D n_1^2 - \sigma_x D n_1 n_x - \kappa_x F(Ft - n_1) - 2\kappa_1 F n_1 \\
\frac{dn_2}{dt} &= \sigma_1 D n_1^2 + \kappa_1 F n_1 - \kappa_2 F n_2 - \sigma_x D n_1 n_2 \\
\frac{dn_3}{dt} &= \kappa_2 F n_2 - \kappa_3 F n_3 + \sigma_x D n_1 n_2 \\
&\cdots
\end{aligned} \tag{2.12}$$

Equation 2.12 describes the time dependent density of monomers n_1 and differently sized clusters n_x, where $x, x \in \{1,2,3\cdots\}$ defines the size of the cluster in number of atoms, for a given deposition flux F (expressed in units of ML/s). These differential equations account for the growth as well as the loss of a particular size due to direct impingements or thermally induced lateral attachments. The cluster formation due to direct impingements onto adatoms or stable clusters can be described through $\kappa_1 n_1$ and $\kappa_x n_x$ terms respectively. Here $\kappa_n, n \in \{1, x\}$ is the impingement cross-section of a cluster of size n that captures deposited atoms by direct impingement [57]. The thermally induced growth of clusters *via* the lateral attachment of monomers or clusters during deposition is described through the capture rates $\sigma_n, n \in \{1, x\}$ and the diffusion term $D = \nu_0 \exp(\frac{-E}{k_B T_d})$, where ν_0 defines the attempt frequency and E the

effective attachment barrier [57].

In Appendix B, the equation 2.12 is reformulated with further approximations and modifications in order to adapt to the specific case of Er adatoms and clusters grown on Cu(111). In particular, (a) we define the growth rates with respect to coverage instead of time, (b) neglect the lateral attachment of adatoms through thermal diffusion (the second term in the expression of $\frac{dn_1}{dt}$) while allowing attachments of adatoms to stable clusters, (c) introduce modified impingement radii in order to describe the cluster formation in presence of the superlattice, (d) assume an uniform value of the capture rates σ_x for $x \geq 2$, and (e) incorporate the coalescence term [57, 58] $-2n_{\geq 3}(1 - \frac{dn_1}{d\Theta} - \frac{dn_2}{d\Theta})$. The coalescence term is added to accommodate our experimental evidence of decreasing $n_{\geq 3}$ beyond 0.10 ML of Er coverage.

After developing this model in Mathematica (version 9) and we have solved these coupled differential equations and obtained the densities of differently sized clusters ($n_x(\Theta)$). These densities are used to obtain the coverage dependent continuous functions $Q_N(\Theta)$, which are defined as the amount of Er present (in units of number of atoms) in a cluster of size N. These functions are used afterwards for simultaneous fitting the population distribution of differently sized clusters which were experimentally determined using LT-STM for two different deposition temperatures (T_d = 4 and 10 K).

2.2.2 Multiplet calculation

In Chapter 3 and 4 we will encounter the use of Multiplet calculation for simulating XAS and XMCD spectra. This is a well-known approach for calculating the energy level diagram of an atom subjected to a certain CF. The corresponding theory can be found in references [47, 59, 60]. Here we will briefly describe the underlying principle and its usefulness in the context of surface-supported RE atoms.

Simulation of XAS and XMCD spectra essentially requires the estimation of the total transition probability (W_{fi}) between an initial atomic configuration $|\Phi_{in}\rangle$ of energy E_i and final configuration $|\Phi_{fin}\rangle$ of energy E_f, upon absorbing an x-ray photon of energy $\hbar\omega$ (to recall the absorption process, see Figure 2.1 a). Within the approximation of electric dipole transition, this can be calculated following Fermi's golden rule as:

$$W_{fi} \propto \sum_q |\langle \Phi_{in}| \hat{e}_q \cdot \vec{r} |\Phi_{fin}\rangle|^2 \delta(E_f - E_i - \hbar\omega) \tag{2.13}$$

where $\hat{e}_q$ defines the polarization vector of the incident x-ray. Note that usually the wavefunctions $|\Phi_{in}\rangle$ and $|\Phi_{fin}\rangle$ are not known *a priori* and calculations of these require an in-depth understanding of the full Hamiltonian of the system.

In a typical multiplet calculation of the light elements (*e.g.* $3d$ metals), one can start by

considering the Hamiltonian of a free atom. Interactions such as spin-orbit coupling and the effects of the surrounding ligands (CF) are further added to this Hamiltonian as perturbations. However, since in the case of RE atoms, the spin-orbit coupling significantly outweighs the strength of the CF, the former should be treated as one of the principal parts of the initial Hamiltonian. Apart from the CF term, such a Hamiltonian ($\hat{H}$) of the free RE atom will contain only four terms, the kinetic energy of the electrons ($\hat{H}_{kin}$), the electrostatic interaction between the electrons and the nucleus ($\hat{H}_{coul}$), the pairwise electron-electron repulsion ($\hat{H}_{e-e}$), and the spin-orbit coupling (SO) ($\hat{H}_{SO}$):

$$\begin{aligned}\hat{H} &= \hat{H}_{kin} + \hat{H}_{coul} + \hat{H}_{e-e} + \hat{H}_{SO} \\ &= \sum_{i=1}^{N} \frac{p_i^2}{2m} + \sum_{i=1}^{N} \frac{-Ze^2}{\vec{r}_i} + \sum_{pairs} \frac{e^2}{\vec{r}_{ji}} + \sum_{i=1}^{N} \zeta(\vec{r}_i)\vec{l}_i \cdot \vec{s}_i\end{aligned} \tag{2.14}$$

Here N is the total number of electrons in the atom, m is the mass and e is the elementary charge of an electron, and Z is the number of protons in the nucleus. For each electron p_i defines the linear momentum whereas $\vec{l}_i$ and $\vec{s}_i$ are the orbital and spin angular momentum respectively, coupled via SO coupling of strength $\zeta(\vec{r}_i)$. The position of each electron from the nucleus is defined as $\vec{r}_i$ while $\vec{r}_{ji}$ defines the distance between the i^{th} and j^{th} electron in the atom.

The first two terms define the average energy H_{av} of a given atomic configuration. The spherical part of $\hat{H}_{e-e}$ can be separated from the non-spherical part and added to H_{av}. The non-spherical part of the $e-e$ repulsion term and the SO coupling determine the relative energy of different multiplets for a given atomic configuration.

The consideration of CF essentially extends the atomic Hamiltonian with an electrostatic interaction term.

$$\hat{H}_{CF} = -e\sum_{i=1}^{N} V(\vec{r}_i) \tag{2.15}$$

Besides these, one should also consider the Zeeman term of $\hat{H}_z = \sum_{i=1}^{N} (\mu_B/\hbar)\vec{B} \cdot (2\vec{s}_i + \vec{l}_i)$ type, in order to calculate the effects of a finite magnetic field (B).

One way of expressing the electrostatic potential function $V(\vec{r}_i)$ is to make full use of the symmetry arguments, the group theoretic concepts, and the well known Steven's operators. In this case $V(\vec{r}_i)$ can be separated in radial and spherical part and the latter can be further expressed in terms of spherical harmonics. The radial part determines the strength of the CF while the spherical part defines the spectral shape [59]. In this approach, the fully symmetrized

multi-electron wavefunctions (the Slater determinants) are used [40, 59].

The CF can also be expressed with an effective point charge approximation. In this approach an extended charge distribution of the surrounding ligands is approximated with a collection of point charges. The corresponding Hamiltonian is defined as:

$$\begin{aligned}\hat{H}_{CF} &= -e\sum_{i=1}^{N} V(\vec{r}_i) \\ &= -e\sum_{i=1}^{N}\sum_{m=1}^{N_{ions}} \frac{Q_m}{|\vec{r}_i - \vec{R}_m|}\end{aligned} \tag{2.16}$$

where Q_m is the strength of the m^{th} ligand charge placed at a distance $\vec{R}_m$ from the atom and N_{ions} is the total number of such surrounding ligands. In particular the point charge model of the CF potential is well suited for describing the $4f$ states of the RE elements since the highly localized nature of the $4f$ orbitals reduces the interaction of the REs with the surrounding environment to a purely electrostatic one [61, 62]. With only Q_m and $\vec{R}_m$ serving as the main degrees of freedom for simulating the required spectral shape, the point charge approach is more simplified compared to the conventional use of the Steven's parameters for describing the CF. Still it allows a quantitative analysis of the magnetic states of surface-supported RE atoms. For all the multiplet simulations presented in this work we have adopted the point charge approach and used the MultiX code developed by A. Uldry, F. Verney, and B. Delley [60] (apart from the ones presented in section 3.2). This code uses the atomic central field Dirac equations to obtain the antisymmetrized wavefunctions within the Density Functional Theory (DFT) formalism as explained in ref. [60]. Relevant specifics of this model and the typical parameters used for the simulations are provided in section 3.3.1 and Appendix A.

2.2.3 Effective spin-hamiltonian model

In Chapter 5 we will come across the use of effective spin Hamiltonian model for describing the experimentally observed spin-excitations in RE-TM heterodimers. The effective spin Hamiltonian model is frequently adopted for simplifying a rather complicated mathematics of a system consisting of N spins. In this model the individual contribution of orbital and spin moments are replaced by an effective spin moment S that obeys the same symmetry properties. This approach has been widely used for interpreting IETS measurements [28, 30, 63] and is also frequently used in molecular magnets [3, 64]. A typical spin Hamiltonian takes the following form:

$$\hat{H} = \hat{H}_{CF} + \hat{H}_{Zeeman} \tag{2.17}$$

There is a subtle difference between equation 2.17 and the Hamiltonian defined in section 2.2.2. Equation 2.17 only considers the lowest multiplet for which the set of levels can be described with an effective spin Hamiltonian. In particular, $\hat{H}_{CF}$ is an effective term that defines the CF symmetry around the magnetic element with an effective spin S and this term describes the splitting among the levels within the lowest multiplet. Depending upon the symmetry of the system, it is usually very convenient to use the standard Steven's operator equivalents to describe this term. For the four fold symmetric case, for instance the case of O-top site on MgO, $\hat{H}_{CF}$ takes the following form (up to the second order):

$$\hat{H}_{CF} = D\hat{S}_z^2 + D'\hat{S}_z^4 + C(\hat{S}_+^4 + \hat{S}_-^4) \tag{2.18}$$

Here, D, D', C are the anisotropy terms describing the CF environment. The z component of the spin operator $\hat{S}$ is defined as $\hat{S}_z$ whereas $\hat{S}_+$ and $\hat{S}_-$ are the spin ladder operators. The first two terms describe the components of the CF along the z axis, and these are responsible for splitting the magnetic levels that differ in S_z. The last terms, which stem from the four fold symmetry of the surface, describe the in-plane component of the CF, *i.e.*, they define the anisotropy in the xy-plane.

The Zeeman term of the spin Hamiltonian, describes the interaction of the effective spin with the external magnetic field B and this can be written as

$$\hat{H}_{Zeeman} = g\mu_B \vec{S} \cdot \vec{B} \tag{2.19}$$

Here g is a tensor that connects the magnetic field and effective spin vector and μ_B is the Bohr magneton.

In the following section, we will describe the use of spin Hamiltonian in dealing with a system of coupled angular momenta, as this will be the case for the exchange coupled RE-TM heterodimers introduced in Chapter 5. In addition to the terms already introduced in equation 2.17, we need to consider an exchange interaction term, $\hat{H}_{Exchange}$, for defining the interaction between the two effective spins of magnitude s_1 and s_2. In order to describe the coupled system including all the relative orientations of the two individual spins, we are going to employ density matrix formalism (see section 2.2.3). Within this formalism and according to the Heisenberg coupling scheme, $\hat{H}_{Exchange}$ can be expressed as:

$$\hat{H}_{Exchange} = J_c \hat{S}_1 \cdot \hat{S}_2 \tag{2.20}$$

where J_c is the coupling constant and $\hat{S}_1$ and $\hat{S}_2$ are the effective spin operators and are functions of s_1 and s_2. The definitions of $\hat{S}_1$ and $\hat{S}_2$ follow from the rigorous quantum mechanical description of a composite systems, *i.e.*, the density matrix formalism which is the focus of the following section.

Density matrix formalism

Density matrix or the density operator $\hat{\rho}$ was first introduced by the polymath mathematician and theoretical physicist Jon von Neumann in 1927. This formalism can be conveniently used for describing the quantum mechanics of a single isolated object, an ensemble of identical isolated objects, and a subsystem of a larger composite system with which the subsystem interacts. For a detailed description of the density matrix formalism readers may refer to references [65, 66]. The density matrix $\hat{\rho}$ is a self-adjoint, positive definite, linear operator, with unit trace (Tr). Unlike the state vector, the density matrix contains all the physically relevant information about the quantum mechanical system. For a composite system of n independent states $|\Psi\rangle_n$, each of which has a statistical weight W_n, the density matrix $\hat{\rho}$ is defined as the following:

$$\hat{\rho} = \sum_n W_n |\Psi\rangle_n \otimes \langle\Psi|_n \tag{2.21}$$

where, $\otimes$ defines the Kronecker product of the state vector $\langle\Psi|_n$ with the corresponding dual state vector $|\Psi\rangle_n$ and the summation extends over all states composing the mixture. For the case of two entangled spins of magnitude s_1 and s_2, we can define two density matrices, $\hat{S}_1$ and $\hat{S}_2$ respectively, each of which spans the composite space of $(2s_1+1)(2s_2+1)$ dimensionality (see equation 2.22). While describing these density matrices, we use the symbol S instead of ρ, only to recall that in our case the state vectors are defined according to the effective spin operators.

$$\begin{aligned} \hat{S}_{j1}(s_1, s_2) &= \hat{S}_j(s_1) \otimes \mathbb{1}_{2s_2+1} \\ \hat{S}_{j2}(s_1, s_2) &= \mathbb{1}_{2s_1+1} \otimes \hat{S}_j(s_2) \\ j &\in \{x, y, z\} \end{aligned} \tag{2.22}$$

where, $\mathbb{1}_d$ is a d x d identity matrix and with the subscripts $\{x, y, z\}$ we define the cartesian

components of the spin operators. Hence,

$$\begin{aligned}\hat{S}_x(s_1) &= (1/2)\{\hat{S}_+(s_1) + \hat{S}_-(s_1)\}\\ \hat{S}_y(s_1) &= -(i/2)\{\hat{S}_+(s_1) - \hat{S}_-(s_1)\}\\ \hat{S}_z(s_1) &= m \times \mathbb{1}_{2s_1+1}\end{aligned} \tag{2.23}$$

where $m \in \{-S_1, -S_1+1, ..., S_1 \in\}$ in steps of 1, are the eigen values of the $\hat{S}_z$ operator, and $\hat{S}_\pm$ are the so called ladder operators.

Therefore, given an example of $s_1 = 1/2$ and $s_2 = 3/2$, the density operators $\hat{S}_{j1}(s_1, s_2)$ and $\hat{S}_{j2}(s_1, s_2)$ are 8×8 matrices with the following forms:

$$\hat{S}_{x1} = \begin{pmatrix} 0 & 0 & 0 & 0 & \frac{1}{2} & 0 & 0 & 0 \\ 0 & 0 & 0 & 0 & 0 & \frac{1}{2} & 0 & 0 \\ 0 & 0 & 0 & 0 & 0 & 0 & \frac{1}{2} & 0 \\ 0 & 0 & 0 & 0 & 0 & 0 & 0 & \frac{1}{2} \\ \frac{1}{2} & 0 & 0 & 0 & 0 & 0 & 0 & 0 \\ 0 & \frac{1}{2} & 0 & 0 & 0 & 0 & 0 & 0 \\ 0 & 0 & \frac{1}{2} & 0 & 0 & 0 & 0 & 0 \\ 0 & 0 & 0 & \frac{1}{2} & 0 & 0 & 0 & 0 \end{pmatrix}, \hat{S}_{z1} = \begin{pmatrix} \frac{1}{2} & 0 & 0 & 0 & 0 & 0 & 0 & 0 \\ 0 & \frac{1}{2} & 0 & 0 & 0 & 0 & 0 & 0 \\ 0 & 0 & \frac{1}{2} & 0 & 0 & 0 & 0 & 0 \\ 0 & 0 & 0 & \frac{1}{2} & 0 & 0 & 0 & 0 \\ 0 & 0 & 0 & 0 & \frac{-1}{2} & 0 & 0 & 0 \\ 0 & 0 & 0 & 0 & 0 & \frac{-1}{2} & 0 & 0 \\ 0 & 0 & 0 & 0 & 0 & 0 & \frac{-1}{2} & 0 \\ 0 & 0 & 0 & 0 & 0 & 0 & 0 & \frac{-1}{2} \end{pmatrix} \tag{2.24}$$

$$\hat{S}_{y1} = i \begin{pmatrix} 0 & 0 & 0 & 0 & \frac{-1}{2} & 0 & 0 & 0 \\ 0 & 0 & 0 & 0 & 0 & \frac{-1}{2} & 0 & 0 \\ 0 & 0 & 0 & 0 & 0 & 0 & \frac{-1}{2} & 0 \\ 0 & 0 & 0 & 0 & 0 & 0 & 0 & \frac{-1}{2} \\ \frac{1}{2} & 0 & 0 & 0 & 0 & 0 & 0 & 0 \\ 0 & \frac{1}{2} & 0 & 0 & 0 & 0 & 0 & 0 \\ 0 & 0 & \frac{1}{2} & 0 & 0 & 0 & 0 & 0 \\ 0 & 0 & 0 & \frac{1}{2} & 0 & 0 & 0 & 0 \end{pmatrix}$$

$$\hat{S}_{x2} = \begin{pmatrix} 0 & \frac{\sqrt{3}}{2} & 0 & 0 & 0 & 0 & 0 & 0 \\ \frac{\sqrt{3}}{2} & 0 & 1 & 0 & 0 & 0 & 0 & 0 \\ 0 & 1 & 0 & \frac{\sqrt{3}}{2} & 0 & 0 & 0 & 0 \\ 0 & 0 & \frac{\sqrt{3}}{2} & 0 & 0 & 0 & 0 & 0 \\ 0 & 0 & 0 & 0 & 0 & \frac{\sqrt{3}}{2} & 0 & 0 \\ 0 & 0 & 0 & 0 & \frac{\sqrt{3}}{2} & 0 & 1 & 0 \\ 0 & 0 & 0 & 0 & 0 & 1 & 0 & \frac{\sqrt{3}}{2} \\ 0 & 0 & 0 & 0 & 0 & 0 & \frac{\sqrt{3}}{2} & 0 \end{pmatrix}, \hat{S}_{z2} = \begin{pmatrix} \frac{3}{2} & 0 & 0 & 0 & 0 & 0 & 0 & 0 \\ 0 & \frac{1}{2} & 0 & 0 & 0 & 0 & 0 & 0 \\ 0 & 0 & \frac{-1}{2} & 0 & 0 & 0 & 0 & 0 \\ 0 & 0 & 0 & \frac{-3}{2} & 0 & 0 & 0 & 0 \\ 0 & 0 & 0 & 0 & \frac{3}{2} & 0 & 0 & 0 \\ 0 & 0 & 0 & 0 & 0 & \frac{1}{2} & 0 & 0 \\ 0 & 0 & 0 & 0 & 0 & 0 & \frac{-1}{2} & 0 \\ 0 & 0 & 0 & 0 & 0 & 0 & 0 & \frac{-3}{2} \end{pmatrix}$$

$$\hat{S}_{y2} = i \begin{pmatrix} 0 & \frac{-\sqrt{3}}{2} & 0 & 0 & 0 & 0 & 0 & 0 \\ \frac{\sqrt{3}}{2} & 0 & -1 & 0 & 0 & 0 & 0 & 0 \\ 0 & 1 & 0 & \frac{-\sqrt{3}}{2} & 0 & 0 & 0 & 0 \\ 0 & 0 & \frac{\sqrt{3}}{2} & 0 & 0 & 0 & 0 & 0 \\ 0 & 0 & 0 & 0 & 0 & \frac{-\sqrt{3}}{2} & 0 & 0 \\ 0 & 0 & 0 & 0 & \frac{\sqrt{3}}{2} & 0 & -1 & 0 \\ 0 & 0 & 0 & 0 & 0 & 1 & 0 & \frac{-\sqrt{3}}{2} \\ 0 & 0 & 0 & 0 & 0 & 0 & \frac{\sqrt{3}}{2} & 0 \end{pmatrix} \tag{2.25}$$

For the specific case of Ho and Co atoms which are exchange coupled as a composite system (frequently referred as heterodimer in this work), we will consider the effective spins as $s_1 = 8$ and $s_2 = 3/2$ respectively (see section 5.3 for reasons behind these assumptions). In that case, one has to imagine the $\hat{S}_{j1}(s_1, s_2)$ and $\hat{S}_{j2}(s_1, s_2)$ operators as 68×68 dimensional matrices.

Finally, we define the total density matrix of the composite system as:

$$\begin{aligned} &\hat{S}_{jc}(s_1, s_2) = \hat{S}_{j1}(s_1, s_2) + \hat{S}_{j2}(s_1, s_2) \\ &j \in \{x, y, z\} \end{aligned} \tag{2.26}$$

Altogether these reduce the effective spin Hamiltonian for a system of two coupled spins subject to an out-of-plane (defined as the z axis) magnetic field B as:

$$\begin{aligned} \hat{H} = {} & D\hat{S}_{zc}^2 + D_1\hat{S}_{z1}^2 + D_2\hat{S}_{z2}^2 + D'\hat{S}_{zc}^4 + D_1'\hat{S}_{z1}^4 + D_2'\hat{S}_{z2}^4 + C(\hat{S}_{c+}^4 + \hat{S}_{c-}^4) + C_1(\hat{S}_{1+}^4 + \hat{S}_{1-}^4) + C_2(\hat{S}_{2+}^4 + \hat{S}_{2-}^4) \\ & + J_c(\hat{S}_1 \cdot \hat{S}_2) + \mu_B[g_1\hat{S}_{z1} + g_2\hat{S}_{z2}] \cdot \vec{B} \end{aligned} \tag{2.27}$$

where,

$$\hat{S}_1 \cdot \hat{S}_2 = \hat{S}_{x1} \cdot \hat{S}_{x2} + \hat{S}_{y1} \cdot \hat{S}_{y2} + \hat{S}_{z1} \cdot \hat{S}_{z2} \tag{2.28}$$

and the ladder operators for the composite and individual systems are respectively defined as

$$\begin{aligned} \hat{S}_{c\pm} &= \hat{S}_{1\pm} + \hat{S}_{2\pm} \\ \hat{S}_{1\pm} &= \hat{S}_{x1} \pm i\hat{S}_{y1} \\ \hat{S}_{2\pm} &= \hat{S}_{x2} \pm i\hat{S}_{y2} \end{aligned} \tag{2.29}$$

The parameters $D_1, D_2, D_1', D_2', C_1$, and C_2 characterize the anisotropy terms of the individual atoms while D, D', and C are the same for the heterodimer.

One of the most useful aspects of using density matrix formalism is realized while evaluating the expectation value of any observable Q. It can be easily shown that the expectation value is given by the trace of the product of $\hat{\rho}$ and $\hat{Q}$ [65].

$$\langle Q \rangle = Tr(\hat{\rho} \cdot \hat{Q}) \tag{2.30}$$

We can use this property in order to calculate the expectation values of the magnetic moments of Ho and Co atoms in the heterodimer. For this, we first diagonalize the spin Hamiltonian to obtain the eigen values and eigen vectors. Using the normalized eigenvectors $|\Phi\rangle_{norm}(j)$, we compute the expectation values of out-of-plane magnetic moments as

$$\begin{aligned} \langle \hat{S}_{z1} \rangle &= Tr[\{ |\Phi\rangle_{norm}(j) \otimes \langle\Phi|_{norm}(j)\} \cdot \hat{S}_{z1}] \\ \langle \hat{S}_{z2} \rangle &= Tr[\{ |\Phi\rangle_{norm}(j) \otimes \langle\Phi|_{norm}(j)\} \cdot \hat{S}_{z2}] \\ \langle \hat{S}_{zc} \rangle &= Tr[\{ |\Phi\rangle_{norm}(j) \otimes \langle\Phi|_{norm}(j)\} \cdot \hat{S}_{zc}] \\ j &\in \{1, 2, 3, ..., 68\} \end{aligned} \tag{2.31}$$

where $\langle \hat{S}_{z1} \rangle$ and $\langle \hat{S}_{z2} \rangle$ are the expected moments of the individual atoms while $\langle \hat{S}_{zc} \rangle$ is the same for the heterodimer.

Finally, the energy level distribution of the magnetic levels shown in Chapter 5 are produced by plotting the eigen values of the spin Hamiltonian as a function of the respective $\langle \hat{S}_{zc} \rangle$ moments.

3 Metal substrate: adatom-substrate interaction

Magnetism of rare earth single atoms on metal substrates

Research interests in surface-supported RE single atoms and small clusters are quite recent. This was initiated in 2004 with the studies of Ce superlattice on Ag(111) [67, 68]. The magnetic properties of the RE adatoms and small clusters were first brought up in 2012 with the report of large magnetic anisotropy in Gd dimers adsorbed on Pt(111) and Cu(111) [36] by Schuh *et al.*, albeit without the ultimate proof of magnetic origin of the observed spin-excitations in the dimers (B field dependence was not reported). Following this, the claim of long magnetic lifetime from Ho atoms adsorbed on Pt(111) caught major attention in this field [37]. Several aspects of this work are largely debated and provoke further questions. Is the CF symmetry enough to decide the magnetic properties or the CF strength also plays a role? Will different RE adatoms possess similar magnetic properties under the influence of the same CF? All these were unknown and yet to be understood.

The long magnetic lifetime of Ho atoms reported in ref. [37] was attributed to the combination of CF symmetry of Pt(111) and the magnetic ground state of the Ho atoms which was calculated from DFT as the maximum possible value of $J_z = 8$. However, as we will see from the first part of this chapter, our XAS and XMCD measurements on the same system reveal a ground state configuration with an intermediate value of $\langle J_z \rangle$, which is incompatible with long magnetic lifetime [40]. The second part of this chapter is focussed on the detailed investigation of Dy, Ho, Er, and Tm atoms adsorbed on Pt(111), Cu(111), Ag(100), and Ag(111). None of these REs exhibit magnetic hysteresis, indicating a magnetic lifetime shorter than tens of seconds. Moreover with the help of multiplet analysis, we will show that the magnetic properties of the RE single adatoms are determined from a delicate interplay between the adatom-substrate and adatom-adatom interaction. The results focussing on the magnetism of Ho atoms adsorbed on Pt(111) have been published in Physical Review Letters by F. Donati, A. Singha, S. Stepanow *et al.* [40]. The results on the $4f$ occupancy of the RE adatoms have been submitted for publication in Physical Review B (2017).

Work contribution

As part of a team led by Dr. Stefano Rusponi, I contributed to all the XMCD measurements presented in this chapter. I carried out the detailed sum rules analysis of the XMCD data presented in section 3.2 and part of the sum rules analysis required for the data presented in Table 3.4, 3.5, 3.6 was shared with Romana Baltic. I have participated in the STM measurements of Ho atoms on Pt(111) with Dr. Fabio Donati and analyzed the corresponding STM images presented in section 3.2. With supervisions from Dr. Fabio Donati and Dr. Stefano Rusponi and using an interactive Python code developed by Dr. Christian Wäckerlin, I have done the multiplet calculations presented in sections 3.3.2 and 3.3.3. The Ruderman-Kittel-Kasuya-Yosida (RKKY) exchange interaction model for Er adatoms on Ag(111) presented at the end of section 3.3.3 was developed with the help of Dr. Fabio Donati.

3.1 Experimental details

The sample preparation, experimental set up, and measurements of XAS, XMCD, and magnetization curves ($M(B)$) have been detailed in sections 2.1.1 and 2.1.2. All XAS and XMCD spectra are measured at 2.5 K and 6.8 T, with the x-ray beam aligned parallel to the external magnetic field (B). The sample preparation for the LT-STM measurements follows from the description in section 2.1.1.

3.2 Magnetic ground state of Ho adatoms on Pt(111)

The XAS and XMCD of Ho atoms adsorbed on Pt(111) are shown in Figure 3.1 a and b. These spectra are characterized by the two distinct edges, namely M_5 (within $1330-1345$ eV) and M_4 (within $1370-1380$ eV), and these are separated due to the SO coupling of the Ho adatoms. The lineshape of the XAS carries fingerprints of the valence shell electronic configuration. The experimental XAS shown in upper panel of Figure 3.1 a, is characteristic of a $4f^{10}$ configuration [69], implying number of holes $n_{\mathrm{h}} = 4$ in the open $4f$ shell of Ho. The XMCD (Figure 3.1 b, upper panel), first of all, shows same signs of dichroism at M_5 and M_4 edges, indicating that the orbital moment is parallel to the spin. Given the large SO coupling, this is very typical of the late lanthanides. Secondly, the angular dependence of the XMCD provides a qualitative idea about the magnetic anisotropy. We note that the Ho adatoms do not possess a large magnetic anisotropy since there is hardly any angular dependence in the measured XMCD. Using $n_{\mathrm{h}} = 4$ in the sum rules we obtain spin and angular momentum of the individual Ho atoms (Table 3.1) [48]. From these we decipher the expectation value of the projected total moment to be $\langle J_{\mathrm{z}} \rangle = 5.42$ in the ground state. This is significantly different than $J_{\mathrm{z}} = 8$ as reported in [37].

In order to understand the directional preference of the magnetization we acquired magnetization curves. $M(B)$ curves depict the behavior of the total magnetic moment projected along the field and beam axis. In normal incidence the magnetization curves saturate at $B > 1.5$ T

(Figure 3.1 c) which indicates that the magnetization prefers to orient along the out-of-plane direction. In grazing incidence $M(B)$ curves reach the same saturation level at the maximum applied field of 6.8 T (Figure 3.1 c). Once again this confirms the low magnetic anisotropy in the Ho atoms. These $M(B)$ curves neither show any opening of hysteresis nor any sign of remanence. Therefore we conclude that the magnetic lifetime is shorter than our experimental time resolution which is about 10 s.

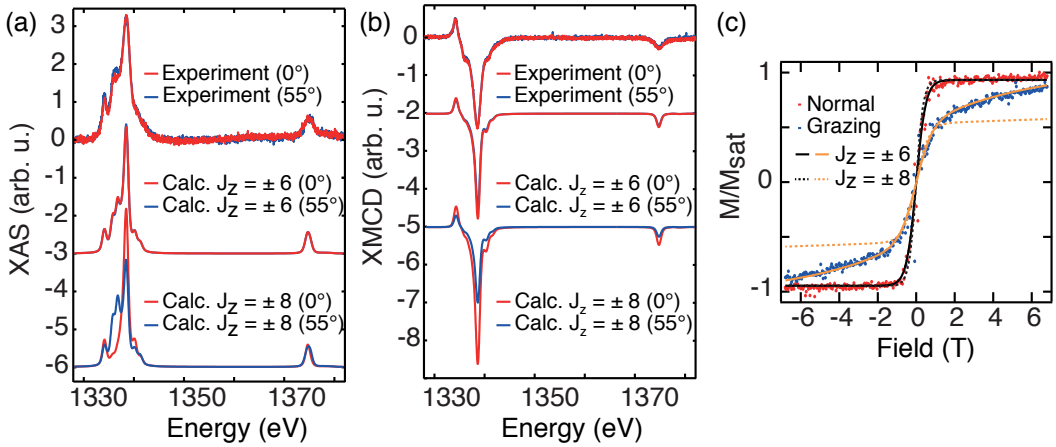

Figure 3.1: Adapted from [40]: Comparison between measured and simulated (a) XAS and (b) XMCD spectra of 0.011 ML Ho/Pt(111) ($B = 6.8$ T and $T = 2.5$ K). Multiplet calculations indicate good agreement with a ground state doublet of $J_z = \pm 6$ (CF parameters: $B_{20} = -140$ μeV, $B_{40} = 1$ μeV, $B_{43} = 0$ μeV). In contrast, the simulation for $J_z = \pm 8$ (considering the CF parameters used by Miyamachi *et al.* in ref. [37]) does not match with the measured spectra. (c) Magnetization curves of Ho/Pt(111): measurements (dots) and expectation values of the total magnetic moment $2\langle S_\theta(B)\rangle + 6\langle T_\theta(B)\rangle + \langle L_\theta(B)\rangle$ from multiplet calculations (solid and dashed lines).

To gain theoretical insight on the magnetic level structure and most importantly the ground state of the Ho atoms, a detailed ligand field multiplet analysis was performed by Dr. Sebastian Stepanow in the group of Professor Pietro Gambardella in ETH Zürich. He considered the C_{3v} symmetry at the adsorption site and employed the conventional Steven's parameters for such analysis. Further details on these calculations can be found in ref. [40] and the supplementary information therein. Leaving aside the detailed analysis, here we will only emphasize on the best fit produced by multiplet simulations for a magnetic ground state of

Table 3.1: In units of $\hbar$, effective spin and orbital magnetic moments ($\langle 2S_z + 6T_z\rangle$ and $\langle L_z\rangle$) for Ho atom adsorbed on Pt(111). Spin moments $\langle S_z\rangle$ are obtained assuming the same ratio of $\langle T_z\rangle/\langle S_z\rangle$ as calculated using the multiplet model [40]. $\langle J_z\rangle$ is obtained by summing the z component of the spin and orbital moments.

θ	$\langle 2S_z + 6T_z\rangle$	$\langle S_z\rangle$	$\langle L_z\rangle$	$\langle J_z\rangle$
0°	2.84 ± 0.13	1.14 ± 0.06	4.28 ± 0.06	5.42 ± 0.08
55°	2.91 ± 0.04	1.21 ± 0.04	3.81 ± 0.06	5.02 ± 0.07

$J_z = \pm 6$ (middle panels of Figure 3.1 a and b). The simulated J_z is in very good agreement with the experimentally determined value of $\langle J_z \rangle = 5.42$ at $\theta = 0°$. In contrast, the spectra simulated for $J_z = \pm 8$ strongly differs from the measured ones. In particular, this ground state would reflect a stronger angular dependence in XAS, XMCD, and $M(B)$ curves unlike what has been observed in our experiments (lower panels of Figure 3.1 a, b, and Figure 3.1c, respectively). In short, together with our measurements, these multiplet calculations suggest a general disagreement with the magnetic ground state predicted by Miyamachi *et.al.* [37]. Note that, the ground state with $J_z = \pm 6$ is incompatible with long magnetic lifetime since, in presence of the three-fold symmetry of Pt(111), these states will be largely mixed to a doublet of almost quenched J_z [40].

The striking difference between our measurements and the ones presented in ref. [37] do not stem from the significantly large Ho coverage used for the XMCD measurements. Firstly, this can be argued following our LT-STM measurements. Figure 3.2 a and b show the STM images of 0.004 and 0.02 ML Ho/Pt(111) acquired at 4.3 and 2.4 K, respectively. For both coverages we find a large majority of the adatoms, *i.e.*, $99 \pm 1\%$ and $93 \pm 1\%$ respectively, as isolated single atoms. The rest of the species exhibit an elongated shape with larger apparent heights (see the zoomed in part of Figure 3.2 b). We have identified them as non-compact Ho-Ho dimers for reasons that will become evident from the following paragraph.

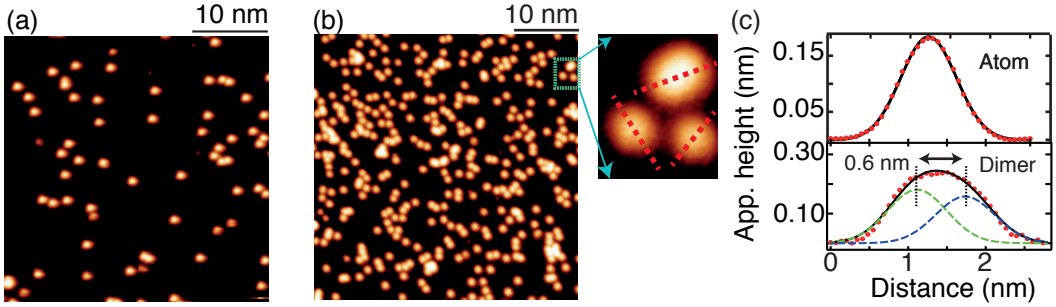

Figure 3.2: STM images of Ho/Pt(111) with (a) 0.004 and (b) 0.02 ML of Ho coverage ($T = 4.3$ K and 2.4 K, respectively). Tunneling parameters: $V_t = -50$ mV, $I_t = 100$ pA. Magnification of one region shown in (b) highlights the presence of an apparent Ho-Ho dimer together with two nearby single Ho atoms. The line profile of atom and the apparent dimer are shown in the upper and lower panel in (c), respectively. Red dots: experimental measures, solid lines: Gaussian fits.

We first fit a Gaussian to the line profile of the isolated adatoms. From the profile of 15 different single adatoms we find the full width at half maximum (FWHM) of the Gaussian to be 0.90 ± 0.05 nm and their apparent height is 170 ± 10 pm (Figure 3.2 c, upper panel). The error bar in each case is a measure of the standard deviation from measurements on several adatoms. Note that measured apparent height is in very good agreement with the one presented in ref. [70], however significantly deviates from the large value (≈ 220 pm) reported by Miyamachi *et al.* [37].

To evaluate the separation between the distinct entities within one elongated object, we fit a

double Gaussian to the line profile of the elongated objects. However, we constrain these fits such that the FWHM and height of each Gaussian are the same as found for the single atoms in the previous step (Figure 3.2 c, lower panel). Performing this analysis on 20 different elongated objects which showed similar spread in their cross-sectional profile, we find the separation of the individual Gaussian peaks to be always higher than 0.55 ± 0.03 nm. Considering the lattice spacing of Pt(111) to be 0.277 nm, this indicates that we do not image any close packed dimer at 0.02 ML. The appearance of the non-compact dimers indicates a short range repulsion between the Ho atoms on this substrate which restricts the formation of a "true" compact-dimer. This allows us to conclude that the magnetic properties of the Ho ensemble presented here are truly dominated by the characteristics of single Ho atoms.

Secondly, we have observed identical lineshape of the XAS and XMCD even after reducing the

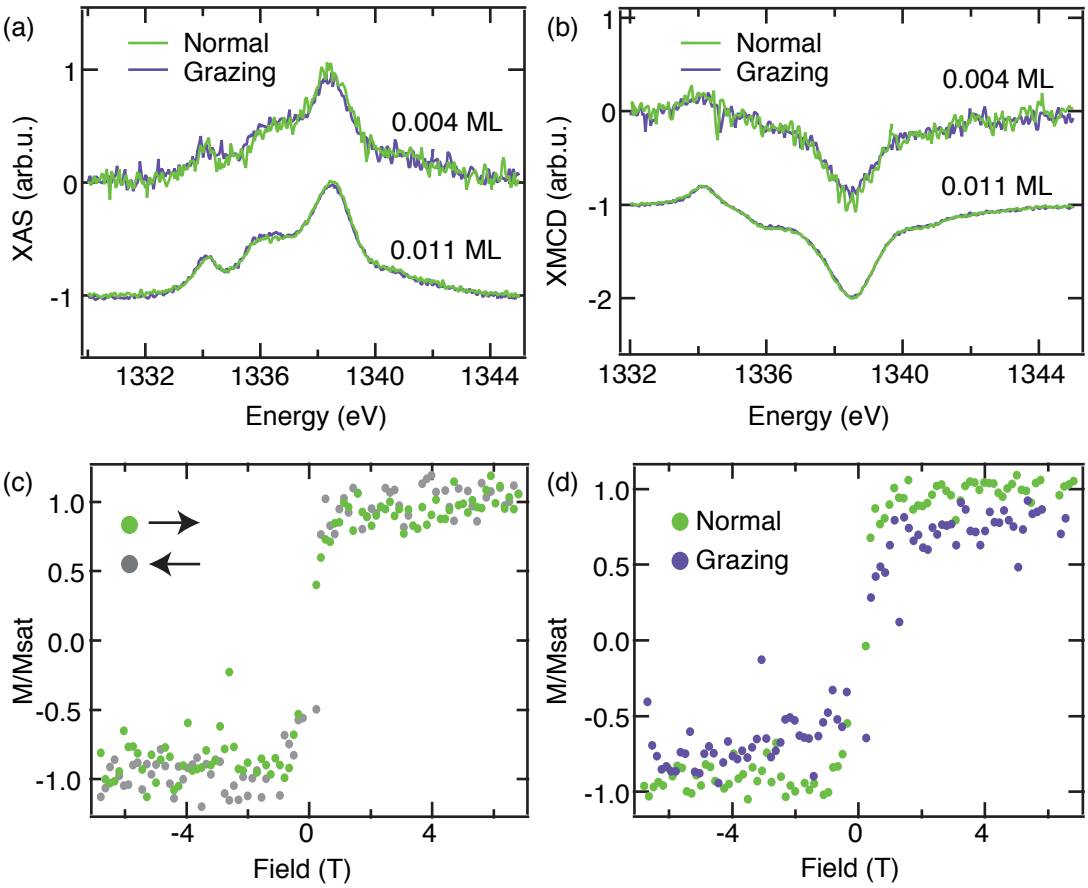

Figure 3.3: Zoom into the M_5 edge of the (a) XAS and (b) XMCD spectra of 0.004 ML Ho atoms adsorbed on Pt(111) showing identical lineshapes as in 0.011 ML case. The spectra are normalized to the total XAS and are offset for clarity. (c) The magnetization curves measured in normal incidence for both directions of the external field sweep highlighting the absence of hysteresis and (d) the magnetization curves for both normal and grazing incidence. $T = 2.5$ K for all panels.

Ho coverage almost by a factor of 3. Figure 3.3 a and b depict the XAS and XMCD (zoomed into the M_5 edge only) for a sample with 0.004 ML of Ho overlaid with the 0.011 ML data from Figure 3.1 a and b. The corresponding $M(B)$ curves of 0.004 ML are shown in Figure 3.3 d. A direct comparison with 0.011 ML XAS and XMCD data, and the $M(B)$ curves in Figure 3.1 c suggest that the angular anisotropies in XAS, XMCD, and $M(B)$ curves are not affected by the chosen Ho coverage, at least within this coverage regime. The XAS lineshape also remains identical. Most importantly, we do not have any evidence of magnetic remanence even at this low coverage as it can be noticed from the fully reversible magnetization curves in normal incidence (Figure 3.3 c). Therefore independently from the LT-STM and XMCD measurements as well as from the coverage-independent magnetic properties, we can unambiguously conclude that the reported $\langle J_z \rangle$ represents the true single atom signature of Ho adsorbed on Pt(111).

To summarize this section, we have shown that the individual Ho atoms adsorbed on Pt(111) possess $J_z = \pm 6$ instead of ± 8. In presence of the three-fold symmetry at the adsorption site, this ground state becomes incompatible with long magnetic lifetime [40]. This is in accordance with the fully reversible magnetization curves observed for the Ho atoms. Together with this work, the irreproducibility of the telegraphic signal by Steinbrecher *et al.* [70] questions the claims made in ref. [37].

It is interesting to note that the authors in ref. [70] also do not report any indirect exchange interaction generated from the Ho atoms on Pt(111) [a]. This may either indicate a weak overlap between the localized $4f$ state and the external $5d6s$ orbitals of the Ho atoms, or a weak hybridization between the $5d6s$ orbitals of Ho and the $5d$ bands of the Pt(111) substrate. However, as we are going to see in the following section, the latter can be excluded based on our XMCD measurements that suggest the evidence of trivalent RE adatoms on Pt(111). The trivalent state indicates a strong hybridization between the external orbitals of the RE atoms and the $5d$ bands of the underlying substrate (see Table 3.3). While the $4f$ electrons may still be well isolated, this strong hybridization can facilitate the promotion of a $4f$ electron to the RE-metal hybrid bands [b], stabilizing the RE in its trivalent state.

In the following we will explore other adatom-substrate combinations in further detail for understanding the effects of different electronic environment surrounding the RE atom. In particular we will focus on transition metal substrates namely Pt(111), Cu(111), two different symmetries of Ag substrate *i.e.*, Ag(100) and Ag(111). This specific choice of the substrates allows us to systematically explore the influence of density of states (DOS) at the Fermi level (E_f) as well as the effect of symmetry, in determining the $4f$ occupancy in RE adatoms.

[a] The strength of the RKKY interaction is below 100 μeV between Ho and Fe atom and below the detection limit for two adjacent Ho atoms. Moreover the induced magnetic moment on the Pt(111) substrate atoms due to Ho is only $0.05\mu_B$ compared to $0.72\mu_B$ induced by Fe atom on the same substrate.

[b] Note that there is a finite $4f-5d$ exchange coupling in trivalent REs [71, 72].

3.3 $4f$ occupancy in surface-supported RE atoms

The electronic configuration of the gas-phase late lanthanide atoms is given by [Xe]$6s^2 5d^0 4f^n$. It is well known that most of the late lanthanides change their $4f$ occupancy in bulk crystals [72–75]. Two distinct configurations have been identified as the most common, namely $[6s6p5d]^2 4f^n$ and $[6s6p5d]^3 4f^{n-1}$ addressed in the literature as divalent and trivalent states respectively. The nomenclature is based on the occupancy of the valence $[6s6p5d]$ band. The context becomes more intriguing in case of surfaces[76], thin films [77], small clusters [73, 78] and surface-adsorbed atoms due to their reduced coordination. Multiple examples of trivalent states of different REs have been reported for surface-supported low coordinated atoms [40–42, 79]. As for the divalent state only Tm on copper and Dy on graphene on Ir(111) have been reported so far [77, 80]. What triggers the different $4f$ occupancies in the surface-adsorbed REs has remained largely unexplored. In this part of the chapter, we are going to identify these factors by means of XAS, XMCD, and multiplet analysis. XAS and XMCD are elegant techniques that allow element specific detection of the magnetic states [40, 81] (see section 2.1.2 for further details). The line shape of the XMCD $M_{4,5}$ edges is the fingerprint of the occupancy of the $4f$ levels and therefore J of the RE under investigation. In addition, the XMCD sum rules [48, 49] and multiplet analysis can be used to estimate the corresponding $\langle J_z \rangle$ values.

3.3.1 Details of Multiplet calculation

In section 3.3.2 we will show that the $4f$ occupancy of a given RE adatom strongly depends on the chosen substrate. In order to verify the assignment of a specific $4f$ occupation we have compared the lineshape of our experimental spectra with XAS and XMCD spectra simulated using multiX software [60]. These calculations are performed for both trivalent and divalent forms of the free RE ions, *i.e.*, without any CF, at $B = 6.8$ T and $T = 2.5$ K. This approach works well as a first step since the XAS lineshape and, in particular, the position of the maximum of the XMCD of a given RE is mainly determined by the $4f$ occupancy [69].

In all the multiplet calculations, the experimental line broadening due to the finite lifetime of the core-hole state is modeled by convolution with a Gaussian of $\sigma = 0.3$ eV. Note that the multiX code relies on the radial functions derived from the corresponding neutral atoms [60]. Therefore the simulations of the free ions necessitate adjustments of all radial function dependent interactions, *e.g.*, the spin-orbit coupling and Coulomb interactions. The spin-orbit coupling of the core levels was scaled in order to match the experimentally observed splittings between the M_4 and M_5 edges (Table 3.2). The Coulomb interaction was scaled such as to reproduce the separations between the multiplet features within the M_5 edge (Table 3.2). The energy axes of all simulated spectra are offset such that they match with the experimental ones.

As we will find in section 3.3.2, we have encountered both trivalent and divalent states. Therefore we employed multiplet analysis to evaluate T_z for both types of $4f$ occupation for a given

Table 3.2: Multiplet simulation: the coulomb (CO), spin-orbit coupling for core (SO-core) and for valence (SO-val) states used for the simulations of XAS and XMCD spectra of each free ions of defined $4f$ occupancy. The parameters are expressed as % of the corresponding Hartee-Fock values. T_z is the estimated spin-quadrupole moment. S_z, l_z, and J_z are the maximum possible projections of the spin, orbital, and total magnetic moment respectively.

Rare earths	Valency → number of $4f$ electrons	MultiX Parameters CO	SO-val	SO-core	T_z ($\hbar$)	S_z ($\hbar$)	L_z ($\hbar$)	J_z ($\hbar$)
Tm	$4f^{n-1}$→12	0.85	0.93	0.93	−0.392	1.0	5.0	6.0
	$4f^{n}$→13	0.85	1.00	1.00	−0.308	0.5	3.0	3.5
Er	$4f^{n-1}$→11	0.85	0.97	0.97	−0.301	1.5	6.0	7.5
	$4f^{n}$→12	0.85	1.00	1.00	−0.394	1.0	5.0	6.0
Ho	$4f^{n-1}$→10	0.90	0.96	0.96	−0.086	2.0	6.0	8.0
	$4f^{n}$→11	0.80	1.00	1.00	−0.297	1.5	6.0	7.5
Dy	$4f^{n-1}$→9	0.75	0.85	0.95	+0.186	2.5	5.0	7.5
	$4f^{n}$→10	0.70	0.85	0.97	−0.106	2.0	6.0	8.0

RE. We use the spin sum rule to obtain the $\langle T_z \rangle$, *i.e.*, $\langle T_z \rangle = (2\langle S_z \rangle - \langle S_{eff} \rangle)/6$ [48, 49]. Here S_z is the spin moment generated by the multiX code for the simulated ground state of the free ion while $\langle S_{eff} \rangle$ is obtained by applying the sum rules on the simulated spectra (see section 2.1.2 for the sum rules). Note that the estimated $\langle T_z \rangle$ values of the trivalent REs are in very good agreement with the values reported in ref. [82]. These T_z values will be used later to evaluate the J_z in the ground state (Table 3.4).

Later in this Chapter we are going to present additional multiplet simulations including the effects of the CF for the specific case of Er. These calculations are aimed at determining the quantum level structure of Er adatoms subject to different CF environments. In this case, the experimental XAS, XMCD, and the magnetization curves are reproduced by modeling the effect of the ligand field generated by the interaction with the surface. The ligand field is simulated as point charges underneath the adsorbed Er atom which is positioned at the center of the coordinate system [60]. The x and y coordinates of the ligand charges are derived from the bulk lattice spacing of the substrates while the vertical separation of the Er atom (z) from these charges as well as the value of the ligand charges are optimized by applying least square fits (Table 3.7). SO and CO parameters are kept the same as in the case of free ion simulation (Table 3.2).

3.3.2 Experimental results and discussions

Valency of RE adatoms

Figure 3.4-3.7 show the characteristic XAS and XMCD spectra of an ensemble of individual Er, Ho, Dy, and Tm atoms on different non-magnetic surfaces. Each RE has characteristic multiplet structure mostly visible at the M_5 edge originating from the dipole allowed $3d$→$4f$

transitions with the following selection rules: $\Delta J = 0, \pm 1$ [83].

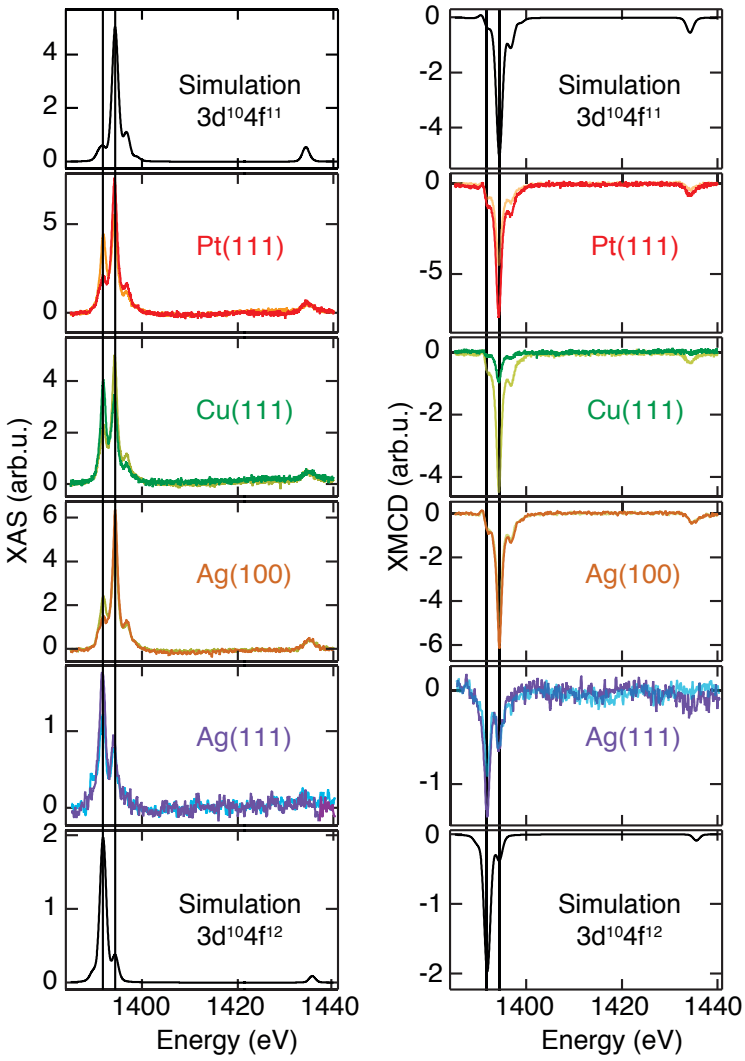

Figure 3.4: XAS and XMCD spectra of 0.018, 0.013, 0.014, and 0.005 ML Er on Pt(111), Cu(111), Ag(100), and Ag(111) respectively. Er/Ag(111) is measured at 5 T due to technical reasons. Normal (grazing) incidence spectra are shown in darker (lighter) color. Multix simulations are shown in top and bottom panels for comparison.

(a) Erbium (Er): The XAS line shapes of Er atoms adsorbed on Pt(111), Cu(111), and Ag(100) are in very good agreement with the spectra simulated for the $4f^{11}$ configuration (Figure 3.4) as well as with previous reports for trivalent Er [19, 69]. On the other hand the lineshape obtained for adsorption on Ag(111) significantly differs from the rest. In particular the central XMCD feature is downshifted in energy. This lineshape matches well with the spectra simulated for a free ion of $4f^{12}$ configuration (bottom panels of Figure 3.4), which indicates that the large majority of the Er atoms is in the divalent state on Ag(111). Since CF alone cannot account for this large energy shift, we attribute the observed shift in the central XMCD feature to an overall change in the $4f$ occupancy. The same is applicable for all the RE-substrate

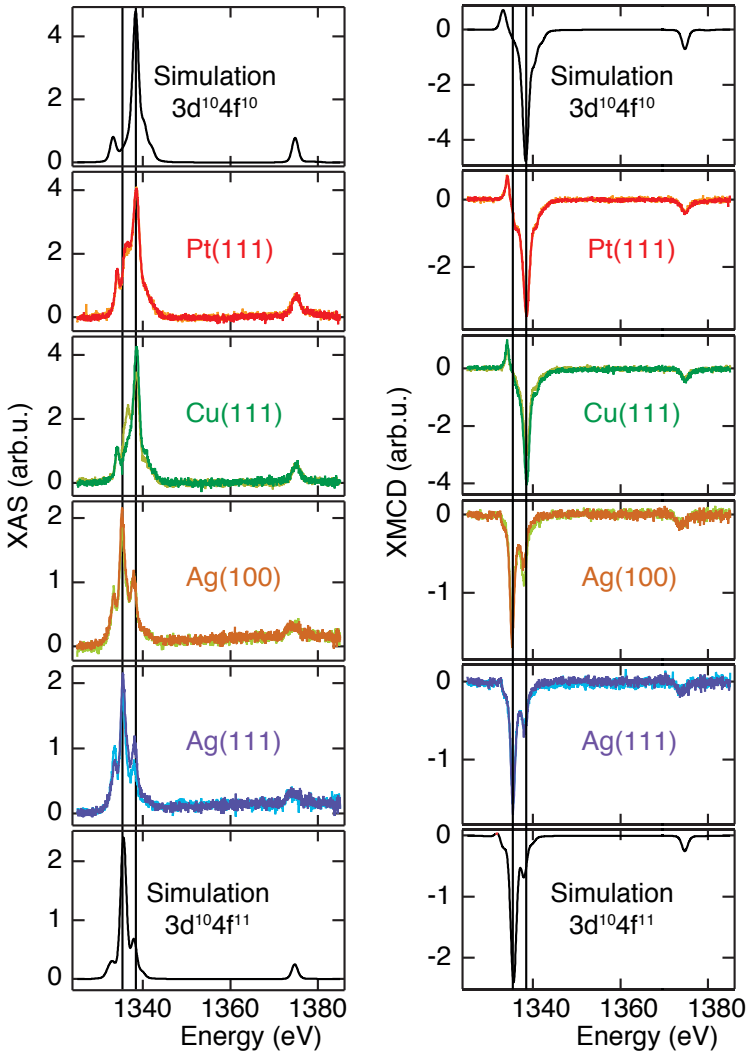

Figure 3.5: XAS and XMCD spectra of 0.011, 0.009, 0.006, and 0.005 ML Ho on Pt(111), Cu(111), Ag(100), and Ag(111) respectively. Normal (grazing) incidence spectra are shown in darker (lighter) color. Simulations are shown in top and bottom panels for ease of comparison.

combinations discussed hereafter. Note that, we can not exclude the possibility of having a mixed valence case. Even at a coverage as small as 0.005 ML we detect a non-vanishing contribution to the XMCD at 1394 eV which corresponds to the position of the trivalent peak. The amplitude of this peak is higher than the corresponding peak at the simulated divalent spectra (bottom panel of Figure 3.4). This might arise from some fractions of the Er atoms in trivalent configuration either due to contamination or formation of clusters. However, within the scope of our measurement and analysis we can not estimate the exact contribution from the trivalent fraction.

(b) Holmium (Ho): The $4f$ occupancy of Ho is verified following the shape of the simulated XAS and XMCD spectra. A trivalent configuration of Ho, *i.e.*, $4f^{10}$ can be identified for adsorp-

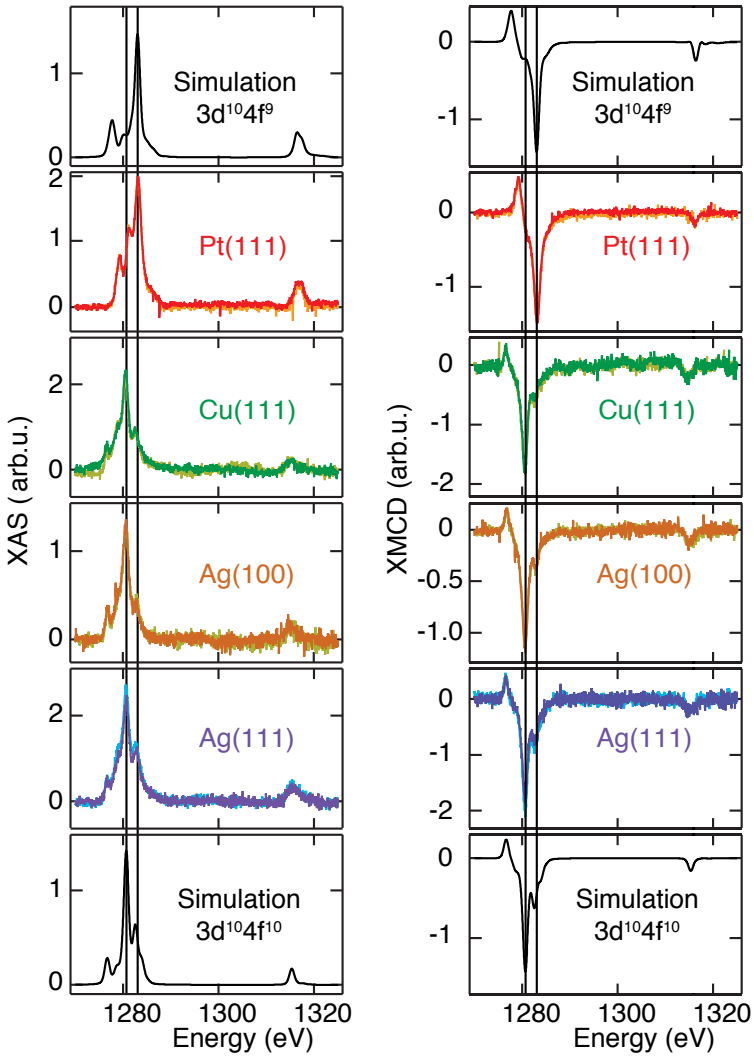

Figure 3.6: XAS and XMCD spectra of 0.004, 0.009, 0.003, and 0.006 ML Dy on Pt(111), Cu(111), Ag(100), and Ag(111) respectively. Dy/Cu(111) and Dy/Ag(111) are measured at 5 T due to technical reasons. Normal (grazing) incidence spectra are shown in darker (lighter) color. Simulations are shown in top and bottom panels.

tion on the Pt(111) and Cu(111) substrates (Figure 3.5) [40, 69]. Unlike Er, Ho shows a divalent configuration ($4f^{11}$) on both crystallographic faces of Ag.

(c) Dysprosium (Dy): The trivalent ground state of Dy, *i.e.*, $4f^9$ occupation [69] is observed only when it is adsorbed on Pt(111) (Figure 3.6). The divalent configuration, i.e., $4f^{10}$ occupation is observed for adsorption on all the three other metals.

(d) Thulium (Tm): The absence of the M_4 peak in the Tm spectra obtained for adsorption on Cu(111) indicates its divalent state which has only one hole in the $4f$ shell [69, 84]. This is further confirmed by comparing the spectra with simulations obtained for both trivalent and divalent cases (Figure 3.7).

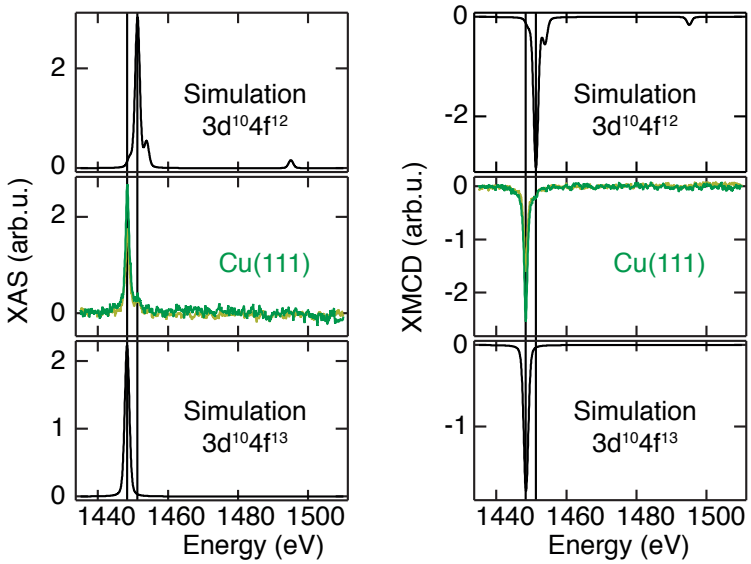

Figure 3.7: XAS and XMCD spectra of 0.010 ML Tm on Cu(111). Normal (grazing) incidence spectra are shown in darker (lighter) color. The top and bottom panels show simulations.

The mechanism which drives the preference towards a particular valency can be explained using an energy level scheme as shown in Figure 3.8. The preference is essentially determined by two relevant quantities: (a) the promotion energy (E_{fd}), and (b) the binding energy (E_b). The former is defined as the difference between $4f^n$ and $4f^{n-1}$ configuration due to the excitation of one electron from $4f$ to $5d$ state in the free atom. The latter is defined as an energy gain upon surface adsorption. According to these definitions, relatively larger value of E_{fd} would suggest a more stable divalent form. However if this can be surpassed by a large gain in energy due to the surface adsorption, the ground state can have a trivalent configuration. In most of the bulk REs, the presence of an additional electron in the $5d$ orbitals allows the binding energy term to largely overcome the promotion energy, hence the energy of the trivalent configuration $E(III)$ is commonly lower than the divalent one $E(II)$ [72, 74]. On the other hand, in low coordinated systems such as clusters [73, 78] or single atoms at surfaces, E_b becomes comparable to E_{fd} and both divalent and trivalent states have been observed [40, 41, 79, 80].

Table 3.3 summarizes the experimentally observed trends in the $4f$ occupation for all the RE adatoms, together with the calculated values of E_{fd} as reported in ref. [72]. The highest E_{fd} for Tm suggests that it is unlikely to have a trivalent configuration for this element. On the contrary E_{fd} for Er, Ho, and Dy are quite similar. Therefore their valency will strongly depend on the net energy gain upon surface adsorption, *i.e.*, surface binding energy E_b. In absense of the information about E_b for every adatom-substrate combinations we have explored, the corresponding trend can be inferred from the respective cohesive energy, which increases from Dy to Er [85]. Consequently we can expect that the trivalent state is the most likely case for Er, less likely for Dy, while this should be intermediate for Ho. The tabulated values of net

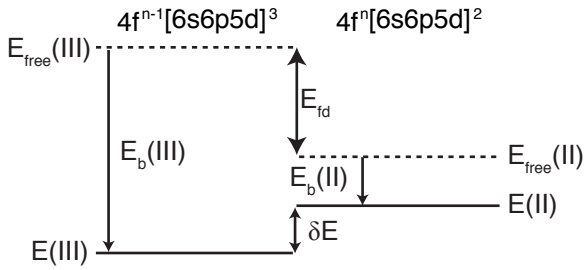

Figure 3.8: Schematic illustrating the two possible $4f$ occupancies in the REs. Whether $4f^n$ or $4f^{n-1}$ is going to be the occupation in the ground state is solely determined by the interplay between two energies, *i.e.*, E_{fd} and the binding energy in the respective valency, $E_b(III)$ and $E_b(II)$. The ground state of the free RE atoms in each configuration is shown as dotted lines while the solid lines indicate the true ground state upon surface adsorption.

energy balance $\delta E = E(II) - E(III)$, which takes into account both promotion and cohesive energy terms in bulk, suggests the same trend [72, 74] (Table 3.3 and Figure 3.8). In agreement with this description, Er is found mostly in the trivalent state while the occurrence of the divalent configuration increases with decreasing δE (Table 3.3).

Table 3.3: $4f$ occupations of the REs on different metal substrates. Here the divalent and trivalent states are addressed as $4f^n$ and $4f^{n-1}$ respectively. E_{fd} is the $4f-5d$ promotion energy whose values are taken from ref. [72]. $\delta E = E(II) - E(III)$ defines the energy difference between divalent and trivalent state. These values are taken from ref. [74].

Rare earths	$4f$ occupancy n	E_{fd} ev	δE eV	Substrates Pt(111)	Cu(111)	Ag(100)	Ag(111)
Er	12	0.89	1.62	$4f^{n-1}$	$4f^{n-1}$	$4f^{n-1}$	$4f^n$
Ho	11	1.04	1.43	$4f^{n-1}$	$4f^{n-1}$	$4f^n$	$4f^n$
Dy	10	0.94	1.30	$4f^{n-1}$	$4f^n$	$4f^n$	$4f^n$
Tm	13	1.63	0.78	–	$4f^n$	–	–

In Table 3.3 the substrates are sorted by the DOS evaluated at the Fermi level E_f as reported in [86]. Interestingly we notice that the $4f$ occupancy of the REs also strongly depend on the supporting substrate, namely all REs possess $4f^{n-1}$ configuration on Pt(111) while they prefer $4f^n$ occupation on Ag substrates. This can be rationalized by recalling the role of substrate DOS. All the substrates considered in this work possess wide s and p bands while the contribution of the relatively narrower d bands to the total DOS at E_f decreases from Pt to Ag [86, 87]. The hybridization between the outer $6s6p5d$ orbitals of the RE with the substrate conduction electrons produces hybrid RE-metal bands, whose DOS at E_f is enhanced when substrate d bands are available. Additionally, the presence of unfilled d orbitals increases from Ag to Pt and enhances the availability of the surface to from stronger bonds with adsorbates. Higher degree of such hybridization leads to larger stability of the trivalent state (Figure 3.8), which requires one of the $4f$ electrons to be promoted to these hybrid RE-metal bands. In good agreement with this picture, we observe that Pt(111) promotes the trivalent states in all

REs while Ag(111) induces the divalent states (Table 3.3).

The $4f$ occupations might differ even in presence of seemingly identical DOS as evidenced for Er atoms on the two crystallographic faces of Ag (Table 3.3). This arises due to the differences in the local coordinations giving rise to different values of binding energy. Specifically, E_b is expected to be larger on Ag(100) with respect to Ag(111) due the higher coordination of the RE atom on Ag(100). Consistent with this description, the RE with the highest δE, *i.e.* Er, shows a trivalent state on Ag(100) and a divalent one on Ag(111). The different binding environment also produces different strength of the CF as detailed in section 3.3.3.

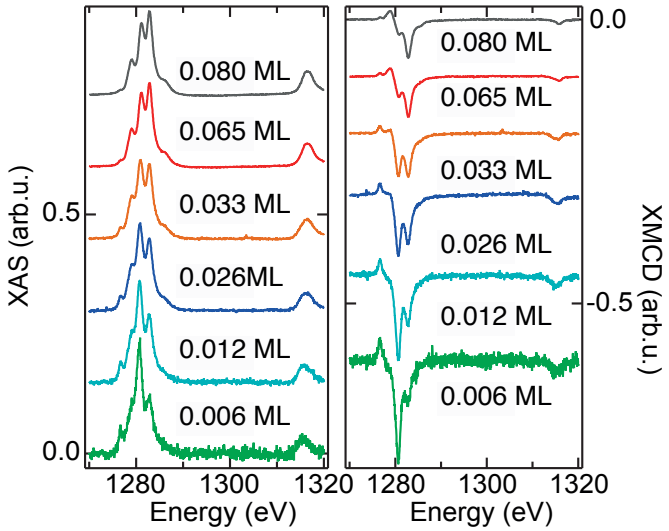

Figure 3.9: Coverage dependent XAS and XMCD measurement of Dy on Ag(111) at normal incidence. Hybridization with the surrounding RE atoms increases at larger Dy coverages and this stabilizes the trivalent state. Spectra are normalized to the total XAS and are offset for clarity.

The correlation between increasing binding energy and stability of the trivalent state is further evident from the XAS and XMCD as a function of RE coverage for Dy and Er on Ag(111) (Figure 3.9 and 3.10). These atoms are mostly divalent in the form of monomers *i.e.*, for coverages below 0.02 ML (Figure 3.6 and 3.5), whereas the signature of the trivalent state becomes more pronounced with increasing coverage (Figure 3.9 and 3.10).

Larger coverages imply increased abundance of RE clusters formed by statistical growth. The increased coordination among the RE atoms enables the formation of RE-RE valence bands, which allows efficient transfer of one electron from the $4f$ to the $[6s6p5d]$ bands [73], and therefore it promotes the formation of a trivalent state. Note that for surface-adsorbed atoms which are already trivalent, the $4f$ occupancy does not change with increasing coordination at larger coverages, as it will be shown for Er on Cu(111) in Chapter 4 [40, 42].

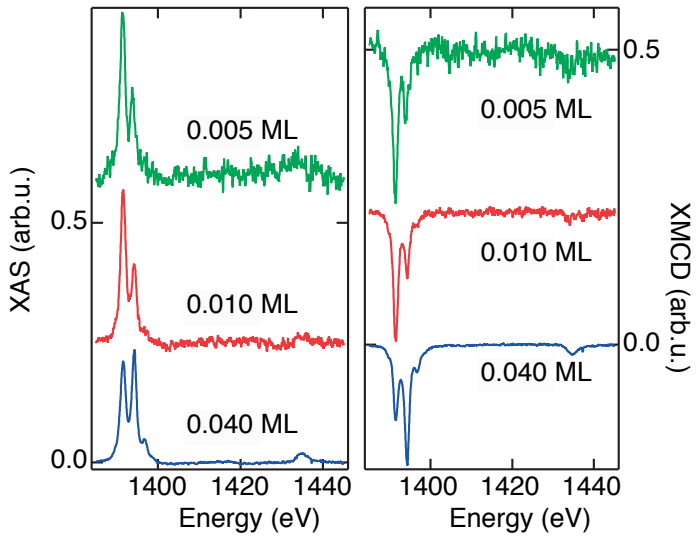

Figure 3.10: Coverage dependent XAS and XMCD studies of Er on Ag(111) at normal incidence. The divalent state is observed up to 0.01 ML while a larger contribution from the trivalent state is observed at 0.04 ML. Spectra are normalized to the total XAS and are offset for clarity.

Magnetic moment and anisotropy

In order to extract the spin and orbital magnetic moments per atom from XAS and XMCD spectra, we apply sum rules. For the different RE-substrate combinations, the $\langle J_z \rangle$ values are presented in Table 3.4 for the two angles of incidence while their detailed sum rule analysis is shown in Table 3.5 and 3.6. The upper bound of these moments correspond to those of the free atoms presented in Table 3.2.Note that for Er/Ag(111) and Tm/Cu(111) we observe strong angular dependence in total XAS (Figure 3.4 and 3.7). Therefore the assumption of isotropic absorption does not hold true for them [88] and additional theoretical knowledge is required to extract the true J_z for such cases as it will be shown in section 3.3.3.

Table 3.4: $\langle J_z \rangle$ values given in units of $\hbar$ derived from the sum rules for the REs on different metal substrates at the two angles of incidence.

Rare earths	θ	Substrates			
		Pt(111)	Cu(111)	Ag(100)	Ag(111)
Er	0°	5.6 ± 0.1	1.0 ± 0.1	6.1 ± 0.1	3.9 ± 0.2
	60°	3.7 ± 0.1	5.0 ± 0.2	5.7 ± 0.1	3.5 ± 0.1
Ho	0°	5.5 ± 0.1	6.9 ± 0.2	4.4 ± 0.1	6.5 ± 0.2
	60°	5.1 ± 0.1	4.9 ± 0.1	4.6 ± 0.1	6.0 ± 0.1
Dy	0°	6.8 ± 0.2	6.3 ± 0.2	6.3 ± 0.2	6.0 ± 0.1
	60°	6.8 ± 0.2	5.9 ± 0.2	6.4 ± 0.2	6.4 ± 0.2
Tm	0°	–	2.2 ± 0.2	–	–
	60°	–	1.9 ± 0.1	–	–

To decipher the orientation of the magnetic easy axis, (a) we measure the angular dependence

Table 3.5: Sum rule analysis: magnetic moments of different RE atoms adsorbed on different substrates: expectation values of effective spin $\langle S_{eff}\rangle = 2\langle S_z\rangle + 6\langle T_z\rangle$, spin $\langle S_z\rangle$, orbital $\langle L_z\rangle$, and total $\langle J_z\rangle$ magnetic moments are expressed in units of $\hbar$. $\theta = 0°$.

Rare earth	Substrate	Moments in $\hbar$			
		$\langle S_{eff}\rangle$	$\langle S_z\rangle$	$\langle L_z\rangle$	$\langle J_z\rangle$
Er	Pt(111)	3.5 ± 0.2	1.1 ± 0.1	4.5 ± 0.1	5.6 ± 0.1
	Cu(111)	1.0 ± 0.1	0.3 ± 0.0	0.7 ± 0.1	1.0 ± 0.1
	Ag(100)	3.8 ± 0.1	1.2 ± 0.0	4.9 ± 0.1	6.1 ± 0.1
	Ag(111)	2.4 ± 0.2	0.5 ± 0.1	3.3 ± 0.2	3.9 ± 0.2
Ho	Pt(111)	2.8 ± 0.1	1.3 ± 0.1	4.3 ± 0.1	5.5 ± 0.1
	Cu(111)	3.8 ± 0.2	1.7 ± 0.1	5.3 ± 0.2	6.9 ± 0.2
	Ag(100)	2.8 ± 0.1	0.9 ± 0.0	3.6 ± 0.1	4.4 ± 0.1
	Ag(111)	3.9 ± 0.2	1.2 ± 0.1	5.2 ± 0.1	6.5 ± 0.2
Dy	Pt(111)	4.1 ± 0.2	2.7 ± 0.1	4.1 ± 0.2	6.8 ± 0.2
	Cu(111)	3.8 ± 0.2	1.6 ± 0.1	4.7 ± 0.2	6.3 ± 0.2
	Ag(100)	3.7 ± 0.4	1.6 ± 0.2	4.8 ± 0.2	6.3 ± 0.2
	Ag(111)	4.2 ± 0.1	1.8 ± 0.1	4.3 ± 0.1	6.0 ± 0.1
Tm	Cu(111)	1.9 ± 0.0	0.3 ± 0.0	1.9 ± 0.0	2.2 ± 0.0

Table 3.6: The same as in Table 3.5 for $\theta = 60°$.

Rare earth	Substrate	Moments in $\hbar$			
		$\langle S_{eff}\rangle$	$\langle S_z\rangle$	$\langle L_z\rangle$	$\langle J_z\rangle$
Er	Pt(111)	2.5 ± 0.2	0.8 ± 0.1	2.9 ± 0.1	3.7 ± 0.1
	Cu(111)	3.2 ± 0.1	1.0 ± 0.1	4.0 ± 0.2	5.0 ± 0.2
	Ag(100)	3.7 ± 0.1	1.1 ± 0.1	4.6 ± 0.1	5.7 ± 0.1
	Ag(111)	2.7 ± 0.1	0.6 ± 0.1	2.4 ± 0.1	3.0 ± 0.1
Ho	Pt(111)	2.9 ± 0.1	1.3 ± 0.0	3.8 ± 0.1	5.1 ± 0.1
	Cu(111)	2.6 ± 0.2	1.1 ± 0.1	3.8 ± 0.1	4.9 ± 0.1
	Ag(100)	2.8 ± 0.1	0.8 ± 0.0	3.7 ± 0.1	4.6 ± 0.1
	Ag(111)	4.0 ± 0.1	1.2 ± 0.0	4.8 ± 0.1	6.1 ± 0.1
Dy	Pt(111)	4.1 ± 0.2	2.7 ± 0.1	4.1 ± 0.2	6.8 ± 0.2
	Cu(111)	3.6 ± 0.1	1.5 ± 0.0	4.4 ± 0.2	5.9 ± 0.2
	Ag(100)	3.2 ± 0.2	1.4 ± 0.1	5.0 ± 0.2	6.4 ± 0.2
	Ag(111)	4.0 ± 0.1	1.7 ± 0.1	4.7 ± 0.2	6.4 ± 0.2
Tm	Cu(111)	1.7 ± 0.1	0.3 ± 0.0	1.7 ± 0.1	2.0 ± 0.0

of the magnetization curves $M(B)$ (Figure 3.11) and (b) we follow the trend of $R = \frac{\langle M_{tot}\rangle @ 0°}{\langle M_{tot}\rangle @ 60°}$ (Figure 3.12).

$M(B)$ curves illustrate the field dependence of the total magnetic moment of the atom under investigation. Therefore, angular contrast observed in $M(B)$ contains information about the magnetic anisotropy of the system (see section 2.1.2 for the detailed method). On the other hand R is a quantity that can be related to the MAE and can be calculated from sum rule values

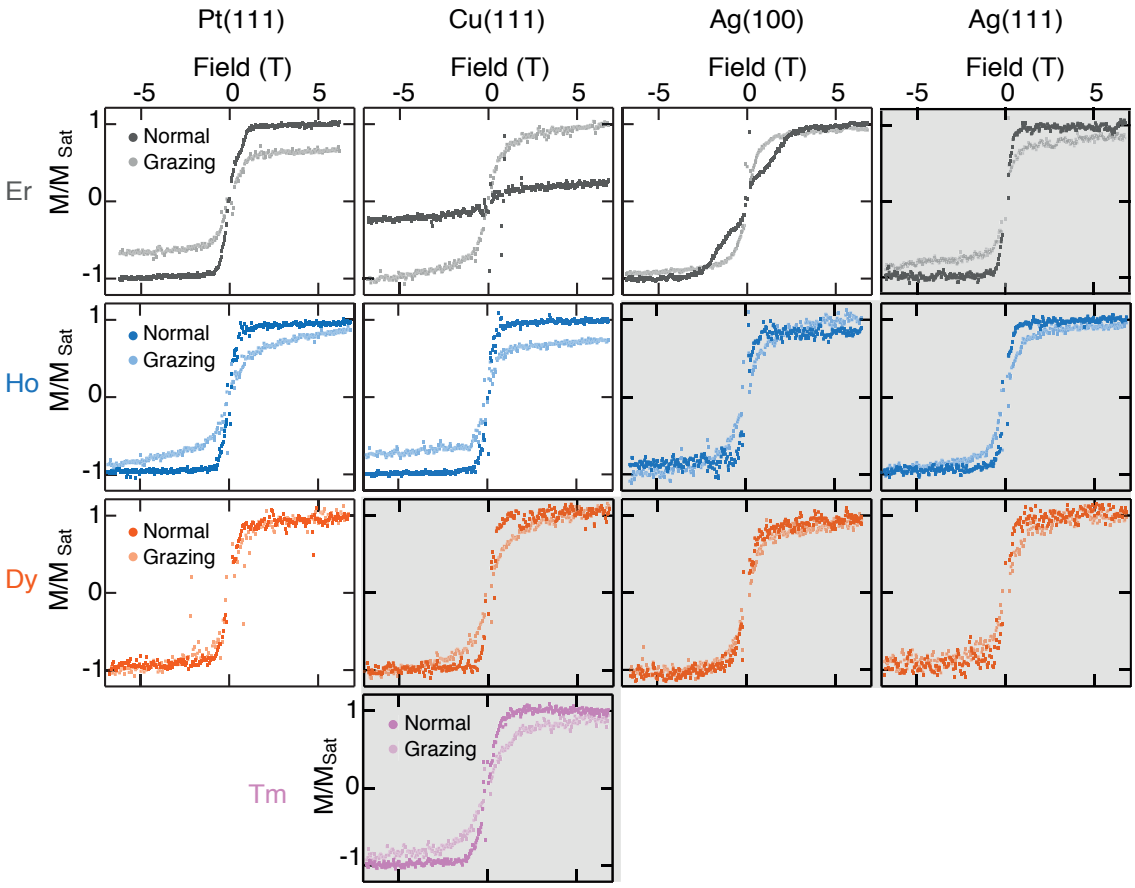

Figure 3.11: Magnetization curves measured for different adatom-substrate combinations. RE coverages are the same as mentioned earlier in Figure 3.4-3.6 for the respective samples. The magnetization curves shaded in grey are from REs in $4f^n$ configuration, while the rests are for REs in $4f^{n-1}$ configuration.

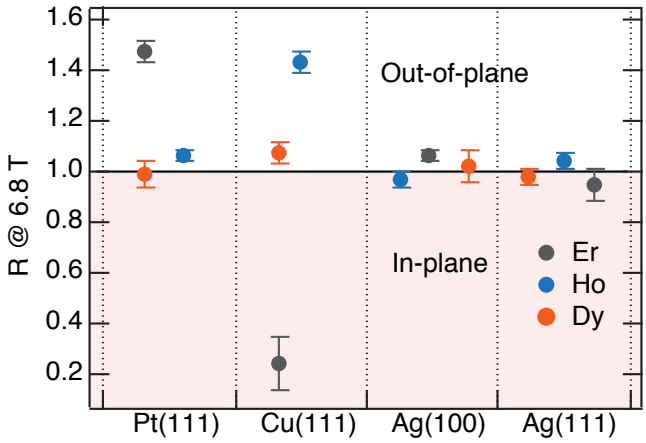

Figure 3.12: $R = \frac{\langle M_{tot}\rangle @0^\circ}{\langle M_{tot}\rangle @60^\circ}$ as obtained for different adatom-substrate combinations at 6.8 T. The shaded region indicates the values of R which correspond to in-plane magnetization.

obtained previously at 6.8 T. Values of $R \approx 1$ indicate very low MAE, while $R > 1$ and $R < 1$ correspond to out-of-plane easy and hard axis respectively [c].

From Figure 3.11 and 3.12 one can immediately discern that the rare earth atoms have low anisotropy on surfaces that mostly promote the divalent state, such as Ag(111) and Ag(100). On the contrary, high anisotropy is observed only for Pt(111) and Cu(111), which exhibit the tendency to stabilize the trivalent state. This can be rationalized considering that surfaces like Pt and Cu provide larger E_b, as discussed in section 3.3.2. A larger binding energy generally corresponds to a shorter adsorption distance from the surface [89], which allows a larger overlap of valence RE orbitals with the substrate electron states. In turn, this generates a stronger CF interaction and a larger splitting of the magnetic levels. In addition, for adsorption on a given substrate, the MAE increases along the lanthanide series from Dy to Er. This also correlates with the increase of cohesive energy along the series of these three elements, as reported in [85].

3.3.3 Hybridization and valency: Er atoms on Ag(100) and Ag(111)

In order to gain insight into the interplay between surface binding, $4f$ occupation of the RE adatom, and strength of the CF, we employed multiplet analysis for Er adatoms on Ag(100) and Ag(111). In this approach we can model the effective crystal field generated by the ligand charges at the surface as point charges (Table 3.7) and gain insight into the quantum level structures of Er atoms exposed to different CF environments. The CF potential, which is given by the position and strength of such point changes, is a measure of RE-substrate interaction. In particular this approach is best suited for the $4f$ states as their highly localized nature reduces the interaction of the REs with the surrounding atoms to a purely electrostatic one [61, 62]. Moreover, Er is the ideal prototype for such analysis since it exhibits different valencies on the two surface terminations of Ag and this further allows us to gain insight into the effects of CF and coordination.

(a) Er on Ag(100)
This system exhibits a change of the slope in the normal incidence $M(B)$ curves at around 1.2 T. This feature hints to a switch of the magnetic ground state from low to high J_z triggered by the Zeeman energy. Similar evidences of such field induced switching of magnetic quantum state have been reported in molecular magnets [90, 91] and Fe atoms on Pt(111) [92]. The peculiar shape of the magnetization curves, as well as the XAS spectra acquired at different fields allow us to determine the magnetic level splitting with very high accuracy.

The results of simultaneous fitting of all experimental XAS and XMCD spectra are presented in Figure 3.13 (a-c). Application of sum rules on the spectra simulated for 6.8 T yields comparable total magnetic moments $\langle M_{tot} \rangle = 2\langle S_z \rangle + 6\langle T_z \rangle + \langle L_z \rangle$ (Table 3.8). Magnetization curves are

[c] Note that an out-of-plane (in-plane) system is identified from a stronger out-of-plane (in-plane) signal in the $M(B)$ curves at the highest applied magnetic field of 6.8 T. Therefore this nomenclature remains valid even if we observe an out-of-plane to in-plane crossover in the $M(B)$ curves (for example, Er and Ho on Ag(100)).

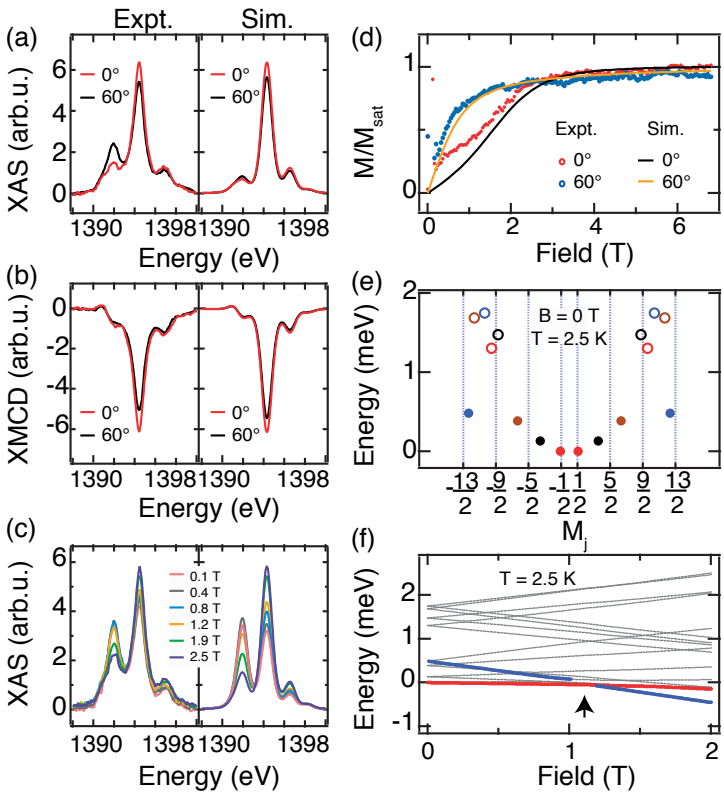

Figure 3.13: Er/Ag(100): Comparison between experimental and simulated (a) XAS, (b) XMCD at $B = 6.8$ T, (c) XAS for different B at $\theta = 0°$, and (d) magnetization curves. (e) Energy splitting of the ground state multiplet calculated for $B = 0$ T and (f) the Zeeman level diagram for the same. Arrow indicates the sharp change in the magnetic moment at $B = 1.16$ T. $T = 2.5$ K.

Table 3.7: Crystal field used for the multiplet simulations of Er atoms on Ag(100) and Ag(111).

Substrates	x Å	y Å	z Å	Charge e
Ag(100)	2.04	2.04	−2.40	−0.6
	−2.04	2.04	−2.40	−0.6
	2.04	−2.04	−2.40	−0.6
	−2.04	−2.04	−2.40	−0.6
	0.0	0.0	−4.48	0.375
Ag(111)	1.669	0.0	−0.61	−0.0115
	−0.834	1.445	−0.61	−0.0115
	−0.834	−1.445	−0.61	−0.0115

simulated by calculating the maximum XMCD at the M_5 edge as a function of B (Figure 3.13d). The simulated curve at $\theta = 0°$ reproduces the change of slope at around 1.2 T very well. The curves at grazing incidence are also very well matched. Additional confirmation of our model comes from the excellent agreement between experimental and calculated field dependent

Table 3.8: Comparison between experimental and simulated moments in $\theta = 0°$ at $B = 6.8$ T for Er atoms adsorbed on Ag(100) and Ag(111). The $\langle M_{tot} \rangle$ values are obtained from sum rules applied on the experimental and simulated spectra.

Substrate	$\langle M_{tot} \rangle$ (μ_B)		$\langle J_z \rangle$($\hbar$)	
	Expt.(Table 3.5)	Sim.	Expt. (Table 3.4)	Sim.
Ag(100)	8.8 ± 0.1	9.8	6.1 ± 0.1	7.4
Ag(111)	5.7 ± 0.3	5.7	3.9 ± 0.2	6.0

XAS (see Figure 3.13c). As expected for a paramagnetic system, the corresponding XMCD signal also showed a monotonic increase of the central peak at 1394.3 eV (data are not shown). As the only discrepancy, the simulations cannot capture the sharp step at 0.2 T in 0°. The vertical mismatch is about 25% of the saturation. We ascribe this effect to the presence of statistically grown small clusters (*e.g.* dimers), the amount of which can be about 10% at this coverage [80, 93]. This can contribute up to 20% of the total absorption signal (assuming all of them as dimers). The magnetization curves of such clusters are likely to exhibit steeper slopes around 0 T owing to their larger moments [d]. Since both atoms and clusters are trivalent on this surface, their XMCD signatures appear at the same energy. Consequently the overall signal is a superposition of the two relative contributions (Figure 3.4). This explains the complex shape of the normal incidence $M(B)$ curve, as well as the discrepancy with simulations.

The corresponding level distribution of the ground state multiplet for $B = 0$ T indicates a ground state with $\langle J_z \rangle = \pm 0.6$ (Figure 3.13e). The overall energy splitting is about one order of magnitude smaller than those reported for Er adsorbed on Pt(111) and Cu(111) [40]. In particular, the proximity of excited states with larger $\langle J_z \rangle$ suggests the potential level crossing in presence of a finite magnetic field. The field dependence of the magnetic quantum levels sketched in Figure 3.13f indicates that this level crossing occurs at $B = 1.16$ T as marked by the black arrow. Consequently the ground state $\langle J_z \rangle$ changes from ± 0.6 at 0 T to ± 7.4 at 6.8 T (Table 3.8). Note that the simulated ground state of $\langle J_z \rangle = \pm 7.4$ at 6.8 T is different than the maximum $J_z \approx \frac{13}{2}$ presented in Figure 3.13 e for $B = 0$ T. At zero field, the magnetic levels are mixed and therefore none of the magnetic levels in Figure 3.13 e correspond to the ideal half-integer J_z. The finite B field breaks this mixing and therefore we observe the almost maximum value achievable within the $J = 15/2$ multiplet of Er in $4f^{11}$ configuration.

(b) Er on Ag(111)

Similarly, multiplet calculations were done for Er atoms adsorbed on Ag(111) by comparing simulations and experiments as shown in Figure 3.14a, b. The excellent match between the values of $\langle M_{tot} \rangle$ obtained by applying sum rules on both simulated and experimental spectra at 6.8 T further confirms the accuracy of our simulations (Table 3.8). The resulting ground state at the maximum field has $\langle J_z \rangle = 6.0$ (Table 3.8), corresponding to the maximum value of $\langle J_z \rangle$ for the $4f^{12}$ configuration. The three fold symmetry of Ag(111) quenches the $\langle J_z \rangle = \pm 6$

[d] Magnetic properties of surface-supported RE atoms (*e.g.*, magnetic moment and easy axis) can differ from the small clusters (see Chapter 4 and ref. [42]).

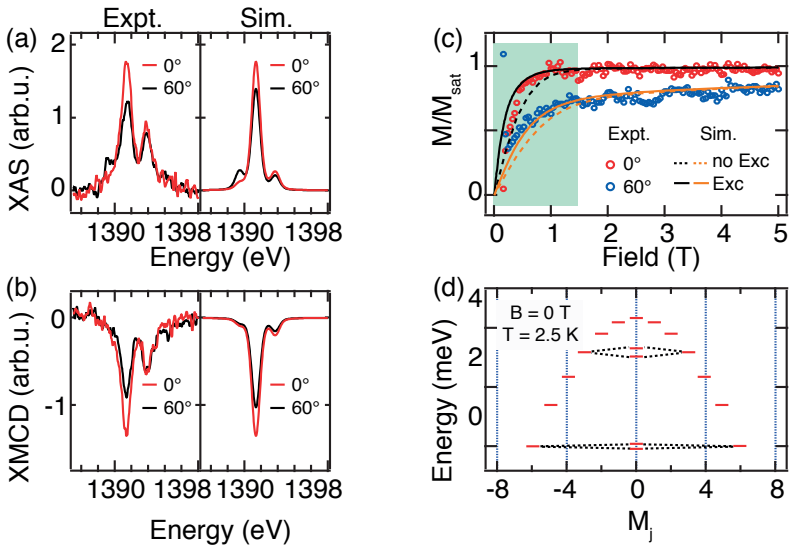

Figure 3.14: Er/Ag(111): Comparison between experimental and simulated (a) XAS, (b) XMCD, and (c) magnetization curves. The region of the $M(B)$ curves shaded in light green highlights the effect of ferromagnetic exchange coupling among the Er atoms. (d) Energy splitting of the magnetic quantum levels.

and ± 3 states (indicated in black dotted lines in Figure 3.14d). These result into two pairs of mixed states with $\langle J_z \rangle = 0$ which are split by 2.2 μeV and 0.3 meV respectively. Note that the simulated J_z at 6.8 T significantly differs from what can be derived using the experimental sum rules (Table 3.8). We attribute this discrepancy to the less accurate estimation of sum rules due to the angular anisotropy observed in the corresponding XAS. Hence for such cases sum rule analysis is not enough for drawing meaningful conclusion on the magnetic ground state, rather a detailed multiplet analysis is strictly required.

The zoomed magnetization curves of this system are shown in Figure 3.14c. Similar to the case of Er/Ag(100) the simulated $M(B)$ curves perfectly match with the measured saturated magnetization at the highest applied field. However, the slopes of $M(B)$ in low fields are not captured at both normal and grazing incidence. The difference between the simulation and the experimental curve is about 0.35 T at 90% of the saturation in normal incidence. The presence of statistically grown clusters can not account for this discrepancy because, differently from the measurements on Ag(100), the signal coming from atoms and clusters can be easily identified, thanks to their two characteristic energies in the XMCD (Figure 3.10). In particular, the clusters contribute to the signal at 1394.3 eV which corresponds to the trivalent peak, while the $M(B)$ curves are acquired at 1391.4 eV corresponding to the divalent peak (Figure 3.10).

Therefore we attribute the discrepancy to the presence of a possible ferromagnetic exchange interaction among the atoms. For atoms adsorbed on a metallic surface, substrate mediated interactions such as the RKKY are activated [94, 95]. The RKKY exchange interaction is spatially

modulated as $J_0 \frac{cos(2rk_F)}{(2rk_F)^2}$ where J_0 represents the interaction strength, r is the distance among the atoms within the superlattice, and k_F is the Fermi wave vector [68, 96, 97]. Thus, for statistically adsorbed single atom distributions the effect is frequently negligible due to the random and large distances among the atoms. For atoms deposited on Ag(111) the situation is different. The surface state electrons of Ag(111) promote a regular arrangement of the Er atoms thus ordering them in a superlattice [42, 67, 68]. The superlattice introduces coherent interactions among atoms thus leading to a magnetic ordering of the Er atoms on Ag(111). Therefore we recalculate the $M(B)$ curves including such exchange interaction. Given the low magnetic anisotropy of the system, we consider Heisenberg coupling among the spins as it has been shown by Umbach *et al.* [97]. Within the mean-field description the effective magnetic field B_{eff} in presence of such exchange interaction can be written as:

$$\begin{aligned} B_{eff} &= B + B_{exc} \\ &= B + \kappa \times g\langle J_z(B_{eff})\rangle \mu_B \\ &= B + \kappa \times M(B_{eff}) \end{aligned} \tag{3.1}$$

Here κ is an empirical constant defining the proportionality between the exchange field B_{exc} and the expectation value of the field-dependent magnetic moment $g\langle J_z(B_{eff})\rangle$. In saturation, the value of the latter is 6.0 $\hbar$ as obtained from simulation. Moreover we can use $g = 7/6$ for the $4f^{12}$ configuration of Er.

Equation 3.1 makes $M(B_{eff})$ implicit function of B_{eff}. Therefore we need to iteratively solve for $M(B_{eff})$ following the set of equations presented in 3.2, until we find the best agreement with the experimental data.

$$\begin{aligned} &1^{st} \text{ iteration:} \\ &B_{eff} = B + \kappa \times M(B) \\ &M(B_{eff}) = M\{B + \kappa M(B)\} \\ \\ &n^{th} \text{ iteration:} \\ &B^n_{eff} = B + \kappa \times M(B^{n-1}_{eff}) \\ &M(B^n_{eff}) = M\{B + \kappa \times M(B^{n-1}_{eff})\} \end{aligned} \tag{3.2}$$

The iteration starts with the $M(B)$ curves obtained from multiX simulations (the dotted curves in Figure 3.14c) and subsequently continues with the iterative calculations of B_{eff} in each step, until the solution converges, *i.e.*, the difference between B^n_{eff} and B^{n+1}_{eff} is less than a set tolerance limit. The best fit provides $B_{exc} = 0.35$ T in saturation (Figure 3.14c), which corresponds to $\kappa = 0.05\ \mathrm{T}/\mu_B$. With this B_{exc} we calculate the total exchange energy $J_{exc} = B_{exc} \times g\langle J_z(B)\rangle \mu_B = 0.142$ meV. Considering that each Er atom has six neighbors, the onsite pair

exchange energy reduces to $J_i = J_{exc}/6 = 0.024$ meV. This exchange interaction corresponds to a Curie temperature of $\sum_{i=1}^{6} J_i/3k_B = 0.55$ K [97]. From the similarly steep $M(B)$ curves measured for both Ho and Dy on Ag(111), one can also speculate the presence of the same effect on those systems (Figure 3.11).

In contrast, we can reproduce the magnetization curves of Ho and Er atoms on Cu(111) using multiplet calculations without introducing any ferromagnetic exchange [40, 42]. This indicates that the strength of such interaction, if any, is well below the measurement temperature for these elements on Cu(111). Since an ordered superlattice with period $r = \pi/k_F$ also forms on this surface, the absence of ferromagnetic exchange on Cu(111) hints towards the fact that J_0 of Ag(111) is larger than the one of Cu(111). Evaluation of J_0 is not very straightforward and it involves complex calculations [94]. Therefore within the scope of this work, we can only attribute the difference in the RKKY strength to the type of adatom-substrate interaction which eventually leads to different fillings of the $4f$ orbitals.

Finally, to pinpoint the effect of different CFs on the magnetic states of Er adatoms, we compare the strength of the CF potential generated by the two substrates. Within the point charge approximation this is defined as $V(r) = \sum_{m=1}^{N_{ions}} (Q_m/|r - R_m|)$ [60], where N_{ions} is the total number of Q_m point charges each at position R_m from the atom of interests (see section 2.2.2 for further details on the point charge model). Using the values presented in Table 3.7, we obtain $|V(r)| = 0.55$ e/Å and 0.02 e/Å for Ag(100) and Ag(111), respectively, confirming stronger interaction potential on Ag(100). Interestingly, the higher coordination offered by the Ag(100) surface is responsible for stabilizing the trivalent state as well as for inducing a stronger CF potential. These effects follow from the larger E_b inferred for this surface compared to Ag(111), which ultimately leads to a stronger RE-metal hybridization and a significantly different charge distribution (Table 3.7).

Chapter summary

- Ho atoms adsorbed on Pt(111) exhibit a ground state with $\langle J_z \rangle = \pm 6$.
- RE atoms can possess either $4f^n$ or $4f^{n-1}$ occupation when adsorbed on metal substrates. The $4f^{n-1}$ configuration is favored in case of
  - low $4f-5d$ promotion energy (E_{fd}).
  - strong binding with the surrounding environment.
- REs exhibit stronger magnetic anisotropy on surfaces that promote the $4f^{n-1}$ configuration.
- Among all the RE adatoms investigated here, Er shows the highest propensity towards the $4f^{n-1}$ configuration.
- None of the four different kinds of RE atoms studied here, namely, Ho, Er, Dy, and Tm, showed magnetic hysteresis or remanence on Pt(111), Cu(111), Ag(111), and Ag(100), indicating magnetic lifetimes shorter than tens of seconds at 2.5 K.

4 Metal substrate: adatom-adatom interaction

Magnetic Hysteresis in Er Trimers on Cu(111)

The results presented in this chapter involve studies of Er atoms and atomic-scale clusters adsorbed on Cu(111). We will present the size-dependent magnetic properties of the Er clusters by combining XAS, XMCD, STM, and mean-field nucleation theory (MNFT). The central focus of this chapter is the adatom-adatom interaction within an Er cluster. This work has been published by A. Singha, F. Donati, C. Wäckerlin *et al.* in Nano Letters [42].

Work contribution

The STM measurements presented here were performed by myself under the supervision of Dr. Marina Pivetta and Dr. Fabio Donati. I also contributed to the XMCD measurements in a team led by Dr. Stefano Rusponi. I have carried out the analysis of the STM as well as the XMCD data and developed the interpretative model for understanding the growth of the Er clusters, under the supervision of Dr. Fabio Donati. I have also performed the multiplet calculations presented in appendix A, under the joint supervision of Dr. Fabio Donati and Dr. Stefano Rusponi.

4.1 Principle concept

From the previous chapter we have learnt that the magnetic properties of surface-supported RE atoms, *i.e.*, $4f$ occupation, orientation of the magnetic easy axis, and the amount of magnetic anisotropy, are closely related to the adatom-substrate interaction. The most compelling example of this is Er atoms adsorbed on Pt(111) and Cu(111). On the former substrate Er shows out-of-plane easy axis while on the latter it is strongly in-plane [40]. In presence of the delocalized $4s$ states of Cu(111), the Er atoms can optimize the electrostatic interaction with the substrate by adapting to the most oblate $4f$ charge distribution, which corresponds to the minimum J_z configuration of Er [98]. On the contrary, the presence of the $5d$ states of Pt(111)

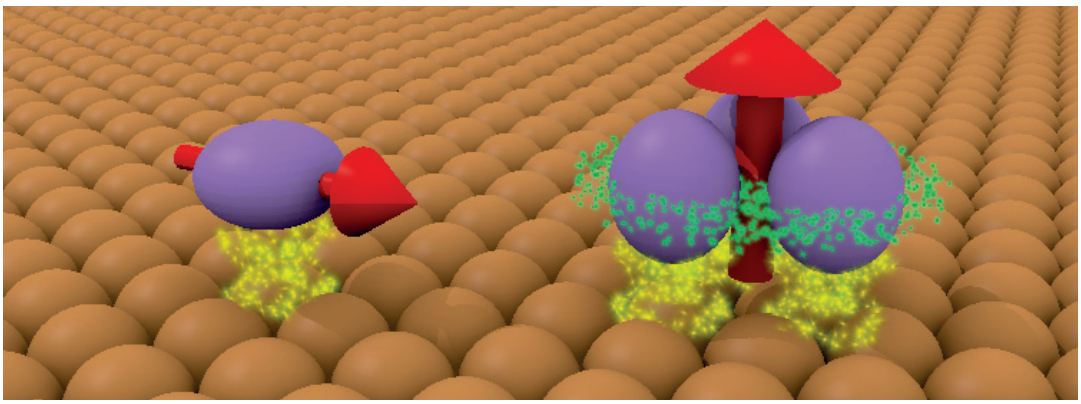

Figure 4.1: Schematic showing two regimes of magnetic anisotropy: in-plane magnetization for single atoms and out-of-plane easy axis for the Er trimers on Cu(111). Red arrows indicate the orientation of the easy axis. Speckles in yellow indicate the interaction between Er and Cu atoms, while the interaction amongst the Er atoms within a trimer is visualized by green speckles.

provides a directional ligand field and induces a prolate charge distribution which corresponds to the maximum J_z [40]. Given this conjecture, we can device a way to engineer the magnetic ground state of surface-supported low-coordinated RE atoms. This is achieved by introducing adatom-adatom interaction which becomes effective in case of small clusters. In addition to the pre-existing adatom-substrate interaction, the individual atoms within a cluster will feel the presence of all other neighboring atoms and therefore they will try to minimize the electrostatic interaction among themselves. In the limit where the adatom-adatom interaction will dominate over the adatom-substrate interaction, we can eventually expect a change in the $4f$ charge distribution from oblate to prolate, which, in other words, will shift the ground state J_z from minimum to its maximum value. This is the central concept of this chapter and is schematically depicted in Figure 4.1.

4.2 Sample preparation: coverage dependent study of Er on Cu(111)

The Cu(111) single crystal was cleaned *in situ* by several Ar^+ sputtering (4 μA/cm^2, 300 K, 1.2 keV, 30 min) and annealing cycles (up to 800 K for 20 min). For the XMCD measurements, we evaporated Er from an e-beam evaporator with a high purity Er rod (99.9 %) onto the substrate held at 3.5 K. The background pressure during deposition was $\leq 4 \times 10^{-11}$ mbar. For the low temperature STM measurements, the deposition was done from a similar Er rod with the substrate kept at either $T_d = 4 \pm 1$ or 10 ± 1 K at a background pressure of 2×10^{-10} mbar. The Er flux and deposition times were carefully controlled to obtain different coverages on the surface.

4.3 Flowchart of our measurements and data analysis

Figure 4.2 shows a schematic summarizing the work flow for the data analysis. This is prepared for ease of going through the delicate sequence of the analysis presented in this chapter.

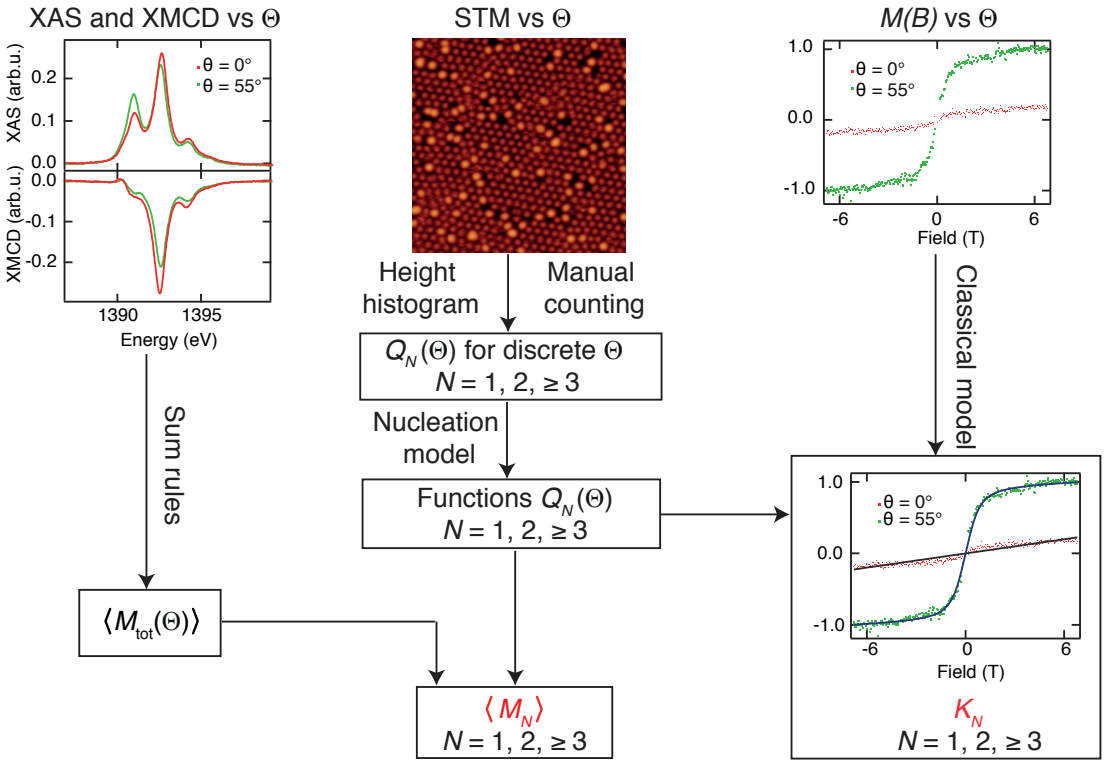

Figure 4.2: Schematic showing the different steps involved in the data analysis. Θ stands for the coverage in ML, $Q_N(\Theta)$ denotes the relative amount of Er present in clusters containing N number of atoms, $\langle M_{\text{tot}}(\Theta)\rangle$ is the expectation value of the total magnetic moment for discrete coverages Θ obtained from the sum rule analysis. $\langle M_N\rangle$ and K_N are the expectation value of the magnetic moment and anisotropy per atom for clusters of size N.

- **XAS and XMCD:** By applying the sum rules to the XMCD spectra, we obtain the total magnetic moment of the Er cluster ensemble as a function of coverage Θ and angle with respect to the surface normal θ.
- **Low temperature STM:** From STM measurements, we get the abundance Q_N of the three cluster-size classes: monomers ($N = 1$), dimers ($N = 2$), and larger clusters ($N \geq 3$).
- **Mean-field nucleation theory:** Since the coverages investigated with the STM do not coincide with, and are not as numerous as the ones investigated by XMCD, we apply mean-field nucleation theory to get continuous functions $Q_N(\Theta)$ to describe the amounts of Er present in the form of monomers (Q_1), dimers (Q_2), and larger clusters ($Q_{\geq 3}$).

- **Estimation of size-dependent magnetic moment:** Using these $Q_N(\Theta)$, we subsequently fit the coverage-dependent total magnetic moments $\langle M_{tot}(\Theta)\rangle$ with the expectation value of the moment/atom for each cluster-size class ($\langle M_N\rangle$, $N \in 1, 2, \geq 3$) as free parameters.
- **Semi-classical fits to $M(B)$:** In addition, from the fits of the magnetization curves at both incident angles and various coverages, we get the magnetic anisotropy energy/atom for each size class (K_N, $N \in 1, 2, \geq 3$).

The rest of this chapter contains the results with the details of all these steps of analysis. Concluding remarks are appended at the end.

4.4 Magnetic properties *vs.* Er coverage

4.4.1 XAS and XMCD

Figure 4.3 a, b show the coverage-dependent XAS at the M_5 edge, for normal and grazing incidence for a selection of Er coverages. Corresponding XMCD spectra were normalized to the total XAS integrated over the entire $M_{4,5}$ edge and are shown in Figure 4.3 c, d. The

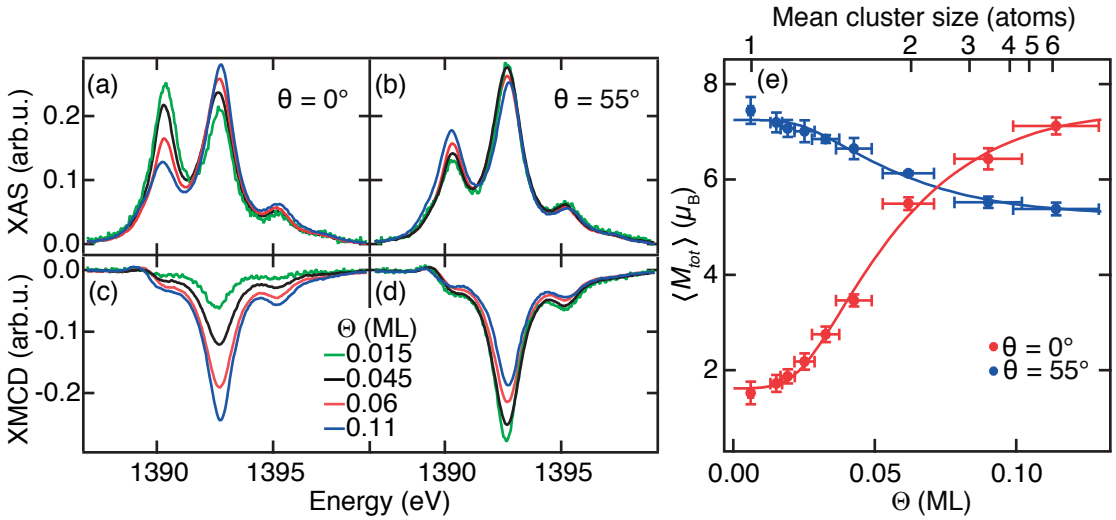

Figure 4.3: (a, b) Coverage dependent XAS and (c, d) XMCD at the M_5 Er edge in normal and grazing incidence ($T = 2.5$ K, $B = 6.8$ T). (e) Out-of-plane ($\theta = 0°$) and close to in-plane ($\theta = 55°$) components of the total magnetic moment as a function of coverage (bottom) and mean cluster size (top), deduced from the XMCD sum rules assuming $n_h = 3$. Solid lines are fits with moments of atoms, dimers and bigger clusters as fit parameters as presented in section 4.6.

overview of all XAS and XMCD acquired for various Er coverages studied during this project is given in Figure 4.4. The triple-peak feature at the M_5 edge corresponds to the dipole allowed

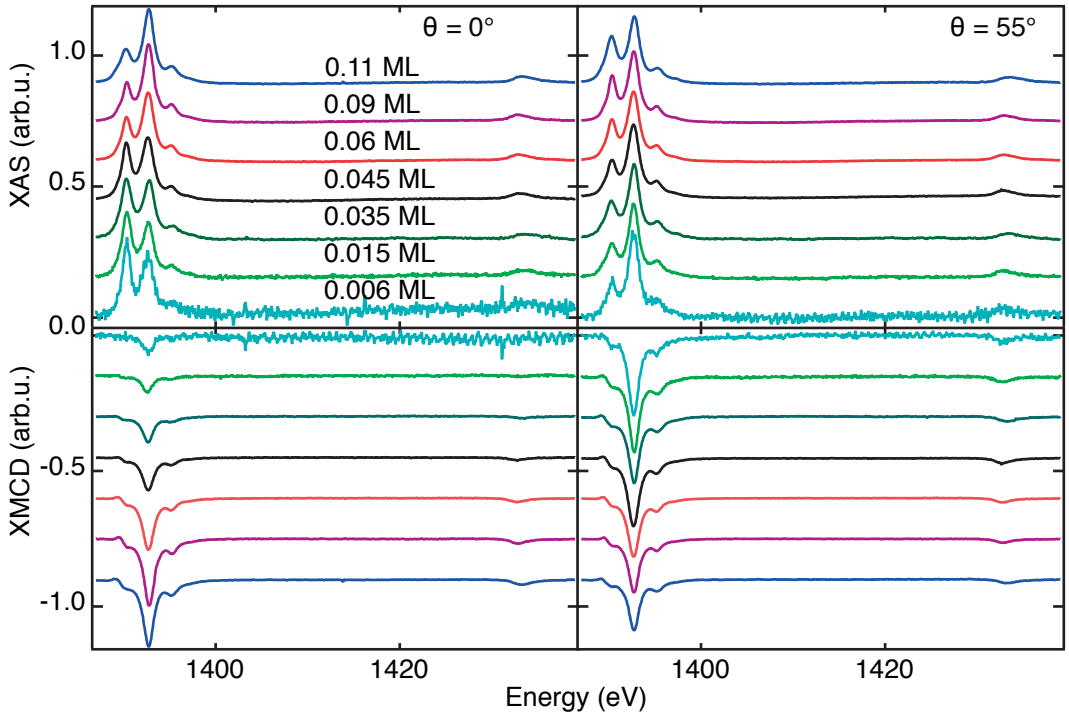

Figure 4.4: Coverage-dependent XAS and XMCD measurements for out-of-plane (left) and close to in-plane (right) x-ray incidence and magnetic field. The spectra are normalized to the integrated XAS and offset for clarity ($T = 2.5$ K, $B = 6.8$ T).

transitions [83] ($\Delta J = 0, \pm 1$) from the filled $3d$ to the open $4f$ shell of Er. Interestingly, a monotonic increase (decrease) of the out-of-plane (in-plane) XMCD is observed with increasing coverage Θ (Figure 4.3 c, d).

The XAS lineshape is the characteristic of a $4f^{11}$ configuration [40, 69] implying 3 holes in the $4f$ shell, $n_h = 3$ independent of the coverage, and therefore a total angular momentum $J = \frac{15}{2}$ following Hund's rules. Apart from the experimental lineshape, the invariance of n_h with Θ is concluded from the absence of spectral shifts [84], and from our multiplet simulations (see Appendix A for the details). Note that this is different than what has been observed for Er clusters on Ag(111) (see the coverage dependent XMCD measurements in Figure 3.10 and the related discussion at the end of section 3.3.2). In that case the $4f$ occupancy and therefore J changes at larger coverages due to stronger hybridization with the surrounding atoms within the cluster.

We applied sum rules to quantify the expectation values of the orbital and effective spin magnetic moments per atom projected onto the beam axis, $\langle L_z \rangle$ and $\langle 2S_z + 6T_z \rangle$, respectively [48, 49]. These values are tabulated in Table 4.1 for all Θ. Summing these two moments, we obtain the expectation value of the effective total moment $\langle M_{tot}(\Theta) \rangle$ projected along the beam (Figure 4.3 e). The solid lines in Figure 4.3 e are fits to the data, details of which are presented in section 4.6. Apart from the $\langle 6T \rangle$ contribution, $\langle M_{tot} \rangle$ corresponds to $g\langle J \rangle$, with $g = 1.2$ the

electron Landé factor. The out-of-plane projected component of $\langle M_{\mathrm{tot}} \rangle$ increases gradually with Θ, reaching a maximum of $7.1 \pm 0.2\ \mu_{\mathrm{B}}$/atom at 0.11 ML. This value is slightly lower than $8.0\ \mu_{\mathrm{B}}$/atom measured in Er crystals along the C-axis at 4.2 K [99]. We attribute this difference to the interaction with the Cu(111) substrate.

Table 4.1: Expectation values of orbital and effective spin magnetic moments/atom in μ_{B} ($n_h = 3$).

Θ (ML)	$\langle L_z \rangle$ $\theta = 0°$	$2\langle S_z \rangle + 6\langle T_z \rangle$ $\theta = 0°$	$\langle L_z \rangle$ $\theta = 55°$	$2\langle S_z \rangle + 6\langle T_z \rangle$ $\theta = 55°$
0.006	0.78 ± 0.19	0.74 ± 0.14	4.09 ± 0.09	3.37 ± 0.27
0.015	0.73 ± 0.14	0.99 ± 0.11	3.97 ± 0.15	3.23 ± 0.14
0.02	0.88 ± 0.11	0.98 ± 0.12	3.89 ± 0.13	3.18 ± 0.12
0.025	1.28 ± 0.10	0.90 ± 0.14	3.83 ± 0.13	3.18 ± 0.18
0.035	1.49 ± 0.10	1.27 ± 0.13	3.89 ± 0.07	2.96 ± 0.05
0.045	1.93 ± 0.09	1.53 ± 0.09	3.75 ± 0.13	2.89 ± 0.18
0.06	3.07 ± 0.10	2.43 ± 0.09	3.42 ± 0.03	2.71 ± 0.03
0.09	3.61 ± 0.14	2.82 ± 0.16	3.11 ± 0.09	2.40 ± 0.08
0.11	3.96 ± 0.12	3.16 ± 0.14	2.94 ± 0.09	2.44 ± 0.09

The growing out-of-plane magnetization with increasing Er coverage can be rationalized by considering the modified effective ligand field created by the increased atomic coordinations at higher coverages (Figure 4.1). For rare earths, the magnetic ground states are closely related to the shape of the $4f$ charge distribution, which for Er is prolate for the maximum and oblate for the minimum possible out-of-plane magnetic moment [98]. The ligand field of the underlying Cu(111) substrate induces an oblate shape of the localized $4f$ charge distribution of single Er atoms, causing the in-plane magnetization observed at the lowest coverages [40]. In contrast, atoms within an Er cluster see the neighbors as equatorially placed charges. To minimize the electrostatic interaction with the ligands, the $4f$ charge distribution modifies to a prolate shape, leading to the observed increase in the out-of-plane magnetization (Figure 4.1). This reorientation of the easy axis in presence of equatorial ligands is further supported by our multiplet simulations. For the theoretical accounts on multiplet simulation the readers are referred to Chapter 2, while the details of the multiplet analysis relevant to the coverage dependent studies of Er is presented in Appendix A.

4.4.2 Magnetization curves $M(B)$ and magnetic relaxation time τ

To explore the magnetic stability and to quantify the MAE of Er clusters of different size, we acquired magnetization curves by recording the field-dependent maximum XMCD at the M_5 edge (Figure 4.5 (a-e) and methods in Chapter 2). No magnetic hysteresis is evident up to 0.035 ML, at which the first butterfly-shaped hysteresis becomes visible in normal incidence (inset in Figure 4.5 b). The hysteresis area increases at higher coverages and the magnetization curves start to exhibit remanence for $\Theta > 0.06$ ML (Figure 4.5 e). Note that the solid lines overlaid with $M(B)$ in Figure 4.5 (a-c) are semi-classical fits to the data as explained

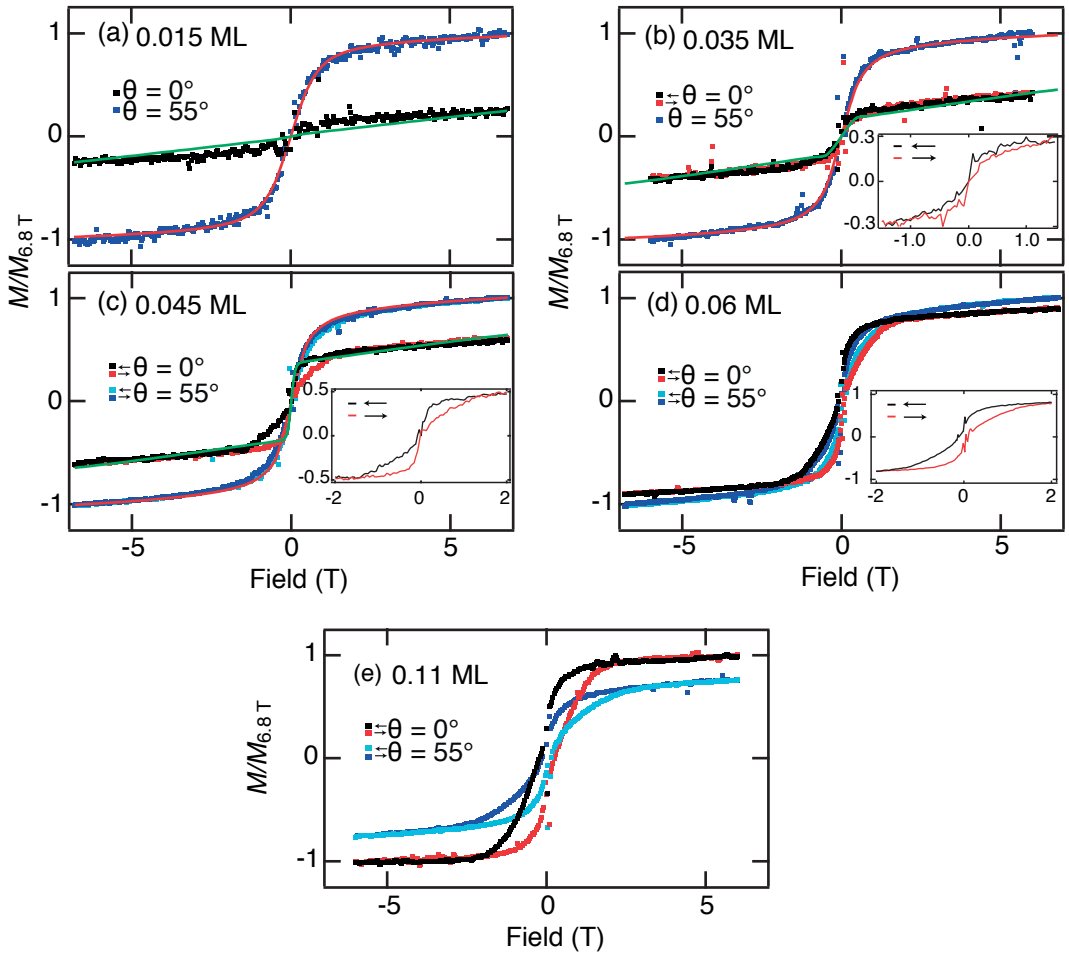

Figure 4.5: (a-e) Magnetization curves. Solid lines are the magnetization curves simulated assuming thermodynamic equilibrium, using the cluster size distributions deduced from the STM measurements and their magnetic properties, as described in the text. Insets in (b-d) show zooms of the magnetic hysteresis in normal incidence at the corresponding coverages ($T = 2.5$ K, $\dot{B} = 12.5$ mT/s).

in section 4.6.2.

The open hysteresis loop at the employed sweep rate of 12.5 mT/s indicates that the magnetization lifetime τ is longer than tens of seconds. To quantify τ, we first magnetized the sample at 3 T and subsequently reduced the field down to 0.1 T, where we recorded the temporal decay of the maximum XMCD. Exponential fits to these data indicate similar values of τ for 0.045 ML, $\tau = 114 \pm 19$ s, and for 0.06 ML, $\tau = 130 \pm 7$ s (Figures 4.6 a, b). The measured τ is expected to be limited by the x-ray induced demagnetization [100] which can be relevant at the employed photon flux of 2×10^{10} photons mm^{-2} s^{-1}. Therefore, these values of τ represent the lower bound to the intrinsic magnetization lifetime. Note that the reported magnetic properties are characteristics of individual atoms and clusters as the distance dependent magnetic interactions, *e.g.*, dipolar and Ruderman-Kittel-Kasuya-Yosida (RKKY) can be neglected in the

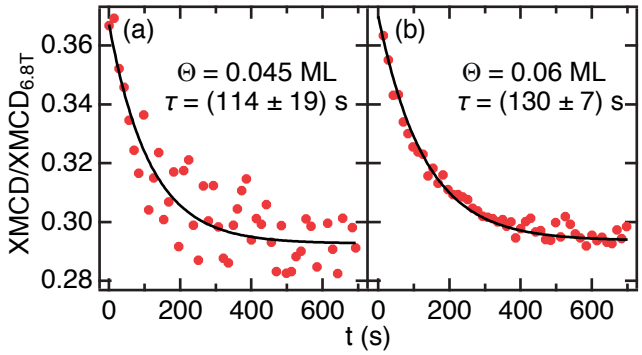

Figure 4.6: Measured time evolution of XMCD. Magnetic relaxation time $\tau = 114 \pm 19$ s and 130 ± 7 s respectively for 0.045 and 0.06 ML Er. Solid lines are exponential fits. ($B = 0.1$ T, $T = 2.5$ K, x-ray flux 2×10^{10} photons mm^{-2}s^{-1}).

present experimental conditions, as mentioned in section 4.6.2.

In the following we will show how to recognize the differently sized Er cluster and given that knowledge, how to identify the minimum cluster size that defines the onset of out-of-plane easy axis and the magnetic hysteresis.

4.5 Low temperature STM measurements

4.5.1 Determination of cluster-size

We characterized the growth of Er on Cu(111) for several coverages Θ using low temperature STM measurements. Figure 4.7 (a-e) show STM images for coverages close to those of the magnetization curves shown in Figure 4.5 (a-e). At the lowest coverage (0.02 ML), most of the Er atoms arrange in a honeycomb lattice with a period of 2.81 ± 0.04 nm (Figure 4.7 a). With increase in coverage, we observe a long range ordered hexagonal superlattice of 1.38 ± 0.04 nm period (Figure 4.7 b). Adatom superlattices form on Ag(111) and Cu(111) surfaces due to a combination of short range repulsion among the single atoms and long range oscillatory interaction mediated by the surface state electrons [58, 68, 96, 101, 102]. The former defines an effective barrier for cluster formation through lateral attachment of adatoms to each other. The first minimum of the latter dictates the equilibrium distance among the single atoms within the superlattice. In the present case, the period is slightly larger than for the formerly studied 3*d* elements on Cu(111) [58, 101] but similar to the one reported for Ce on Cu(111) [96], due to a strong dipolar contribution to the short range repulsions for the lanthanides. Note that a high tunnel resistance was crucial for non-perturbative imaging of the superlattices, as also observed for other RE superlattices on noble metal surfaces [68, 96, 102].

The ordered structure of the superlattice is perturbed by Er clusters whose relative abundance and size increases with coverage (Figure 4.7 (a-e)). To identify their size, we analyzed their characteristic shape and apparent height profiles. Figure 4.8 a illustrates the shapes of the

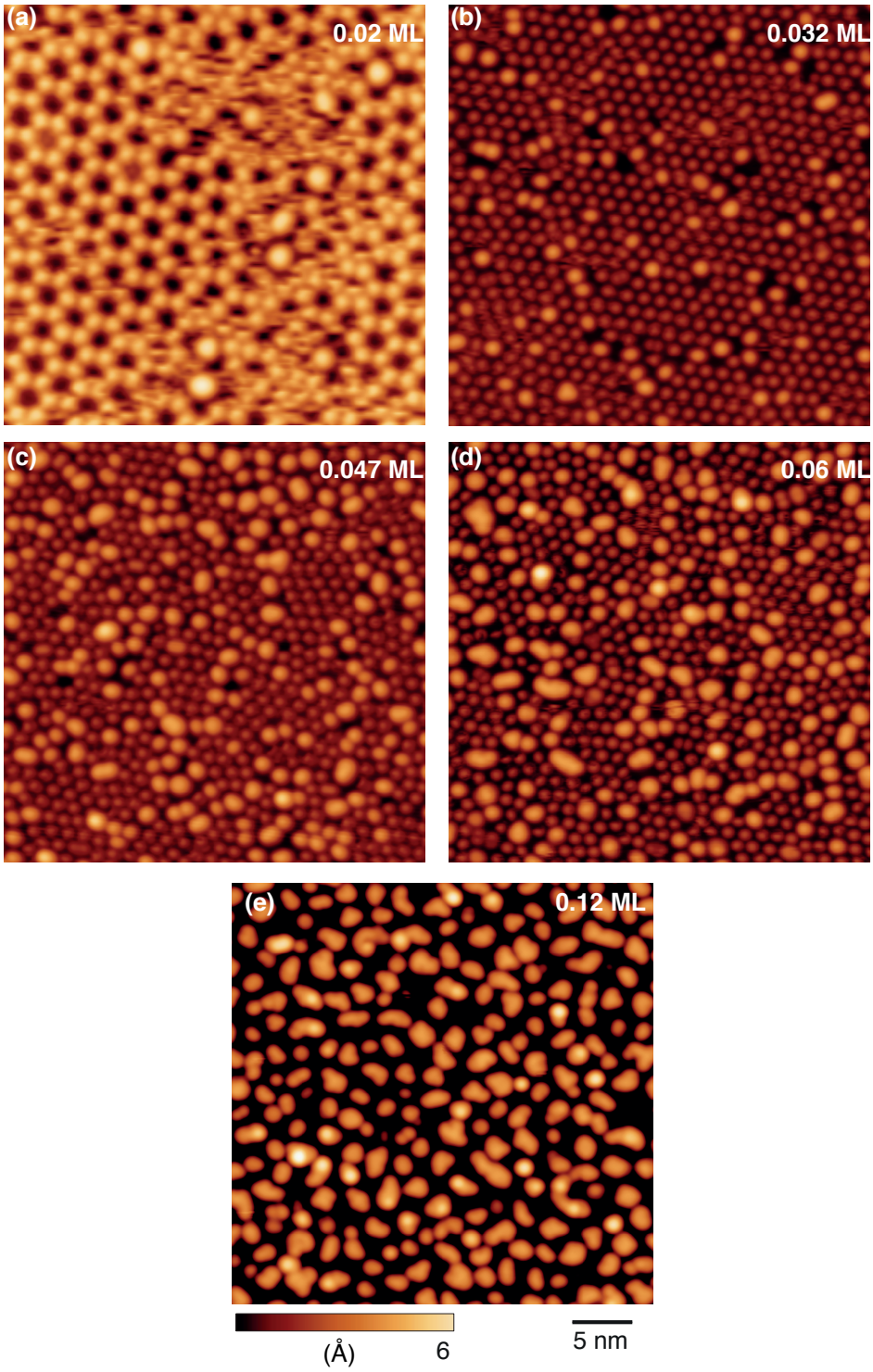

Figure 4.7: (a-e) STM images at coverages close to the ones for which the magnetization curves in Figure 4.5 (a-e) were recorded. For (a-d) the deposition temperature was $T_d = 4 \pm 1$ K and the STM measurement temperature was $T = 4.4$ K. The imaging parameters were: (V_t, I_t) = (1.8 V, 10 pA), (−30 mV, 100 pA), (−50 mV, 100 pA) and (−300 mV, 500 pA) respectively. For (e): $T_d = 10 \pm 1$ K, $T = 5$ K, and (V_t, I_t) = (100 mV, 20 pA).

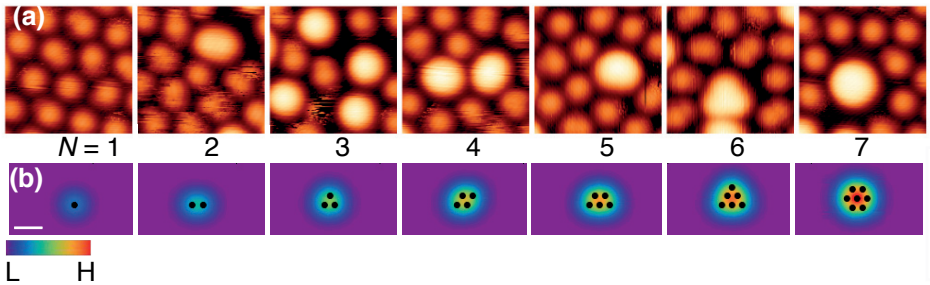

Figure 4.8: (a) Shape of the observed Er species with size of N atoms (Image size: 5×5 nm^2, $V_t = -30$ mV, $I_t = 100$ pA, and $T = 4.4$ K). (b) Simulated shapes with the positions of the constituent atoms marked as black dots. Scale bar is 1 nm.

observed Er species as function of the number of constituent atoms, N. These shapes are well reproduced assuming 2D gaussian profiles of the constituent atoms with their centers separated by the nearest neighbor distance of bulk Er (355 pm) (Figure 4.8 b).

In addition, the apparent height profiles clearly differentiate the $N = 1, 2$ and ≥ 3 species [21, 36, 70, 103, 104] (Figure 4.9 a). These three size groups also possess distinct electronic properties as demonstrated by our scanning tunneling spectroscopy (STS) measurements (Figure 4.9 b). Note that the tunneling current for these STS measurements is low and larger set points induce adatom hopping.

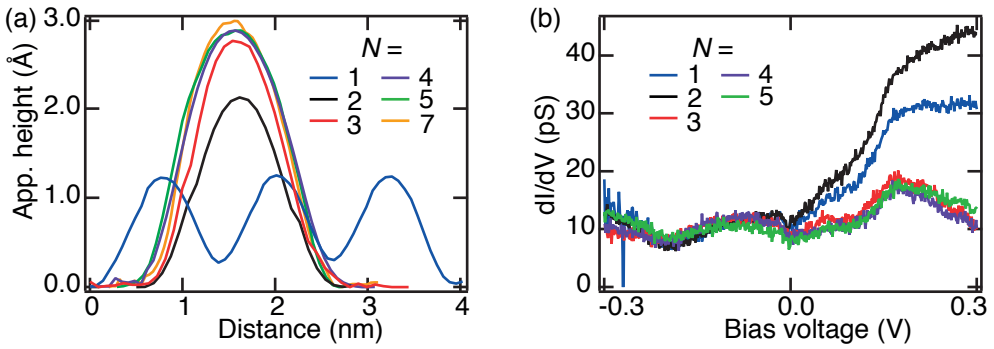

Figure 4.9: (a) Apparent height profiles of different Er species. (b) STS measurements showing contrast in the electronic properties among $N = 1$, 2 and ≥ 3 species ($V_t = -300$ mV, $I_t = 300$ pA, lock-in modulation $V_{mod} = 10$ mV peak-to-peak at a frequency $f = 2687$ Hz, and $T = 4.4$ K).

A sharp contrast between $N = 2$ and ≥ 3 species is also evident from their distinct stability towards dissociation induced by the tunneling electrons from the STM tip. Figure 4.10 (a-c) display a sequence of STM images showing the creation of a dimer and a trimer and the subsequent split of the dimer. The cluster formation is accomplished by approaching the tip with typical tunneling parameters ($V_t = 10$ mV, $I_t = 10$ pA) and subsequently increasing the set point current of the feedback loop until a sudden change in the tip height occurs. The dimer is split by applying 600 mV with the tip placed on top (Figure 4.10 c). The trimers and larger clusters cannot be dissociated, they remain intact up to at least 2 V, beyond which we have

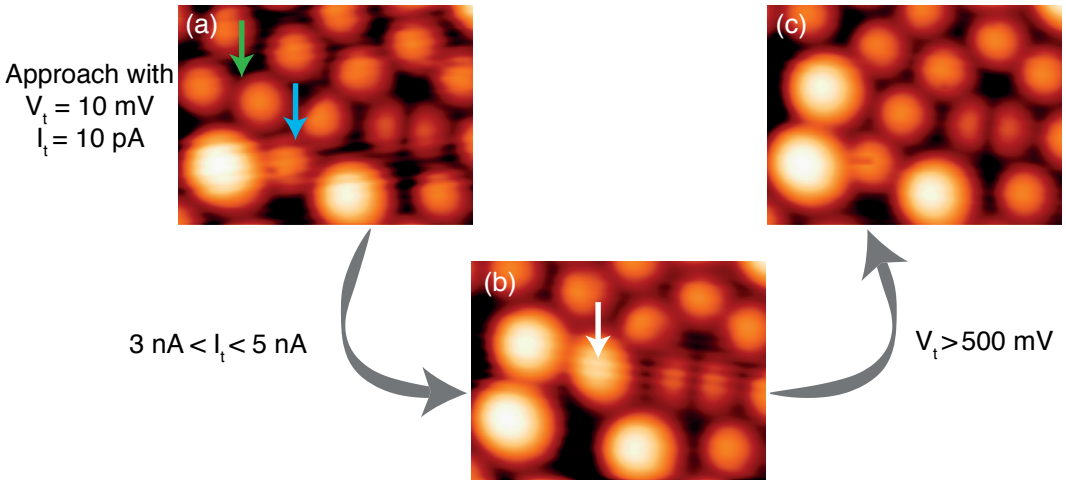

Figure 4.10: Sequence of STM images showing, from (a) to (c): creation of a dimer (trimer) by atomic manipulations at the two locations marked with cyan (green) arrows in (a); from (b) to (c): the dimer splits into two monomers by applying 600 mV with the tip positioned at the white arrow. (Image size: 6×4.5 nm^2, $V_t = -300$ mV, $I_t = 100$ pA, and $T = 4.4$ K).

observed uncontrolled modifications of the surface. These observations indicate that dimers are much less stable than all bigger clusters.

The distinct electronic and structural properties of $N = 1, 2$ and ≥ 3 species suggest the distinction of these three size classes as a first approach. In the following we are going to illustrate how to quantify their relative abundance $Q_N(\Theta)$ from their apparent height distribution extracted from the STM images. This quantity is directly related to the contribution from each cluster-size class in the measured total XMCD signal.

4.5.2 Estimation of $Q_N(\Theta)$

Estimations of Q_N require a prior knowledge of the population distribution at a given coverage. This is obtained from the apparent histograms extracted from the STM images as illustrated in Figure 2.6. Further details on this can be found in section 2.1.3. Knowing this distribution, $Q_N(\Theta)$ for $N \in 1, 2$ can be calculated by multiplying the abundance of a certain cluster type with the respective size N for a given coverage Θ. To obtain $Q_{\geq 3}$ we calculated $(1 - Q_1(\Theta) - Q_2(\Theta))$. For applying the four population nucleation and growth model (discussed in appendix B.2), we first calculate $Q_3(\Theta)$ separately for the trimers and then $Q_{\geq 4}(\Theta)$ is obtained as $(1 - Q_1(\Theta) - Q_2(\Theta) - Q_3(\Theta))$.

In order to explore the effect of thermally induced cluster formation during deposition, we prepared two sets of samples characterized by their deposition temperatures, namely $T_d = 4 \pm 1$ K and 10 ± 1 K. This produced lower or higher relative amounts of $N \geq 3$ clusters by thermally activated adatom-to-cluster attachment. Q_N for the two deposition temperatures are shown in Figure 4.11 a and b. Note that by definition they always add up to 100 % for a

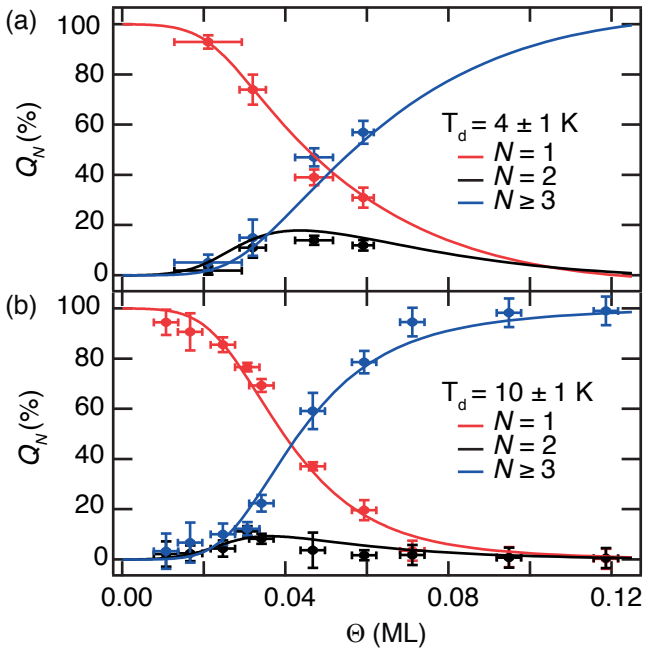

Figure 4.11: Coverage dependence of Q_N, the fraction of Er present in N-sized cluster for Er deposition at (a) 4 K and (b) 10 K. Dots: data deduced from the apparent heights in the STM images; full lines: results from mean-field nucleation theory with the parameters discussed in appendix B.1.

given coverage Θ. From 0.03 ML onwards, $Q_{\geq 3}$ is higher for $T_d = 10 \pm 1$ K.

Since the STM and XMCD measurements were not taken at the same coverages, and with the aim of achieving a more quantitative understanding of the growth of this system, we simulated the observed trends of $Q_N(\Theta)$ by modeling the nucleation and growth with rate equations from MNFT (see section 2.2.1 for further details on this). This model accounts for the particularities of the present system, namely, the presence of an attachment barrier as well as the large and coverage-dependent cross-sections for nucleation by direct impingement [56, 57]. For most purposes, we have adopted the three population growth model where we consider three types of Er clusters, namely, monomer ($N = 1$), dimer ($N = 2$), and bigger clusters ($N \geq 3$). Solid lines in Figure 4.11 a and b are fits to the data using the three population growth model. One can appreciate that the experimental results are very well reproduced for both deposition temperatures evidently with a single set of parameters. Only for some specific purposes we have considered the four population growth model describing the densities of monomer ($N = 1$), dimer ($N = 2$), trimer ($N = 3$), and bigger clusters ($N \geq 4$). Further details on these growth models can be found in appendix B.1 and B.2.

4.6 Cluster-size dependent magnetic properties

4.6.1 Magnetic moments of different size groups

The knowledge of $Q_N(\Theta)$ allows us to quantify the expectation value of the magnetic moment/atom $\langle M_N \rangle$ for each cluster size N for normal and grazing incidence. For this we fit the measured $\langle M_{\text{tot}}(\Theta) \rangle$ using the following equation:

$$\langle M_{\text{tot}}(\Theta) \rangle = \sum_{N=1,2,\geq 3} \langle M_N \rangle Q_N(\Theta) \tag{4.1}$$

The solid lines in Figure 4.3 e are these fits from which we extract the six values on the left hand side of Table 4.2. These values suggest a larger in-plane than out-of-plane moments for $N \leq 2$. On the contrary, the trimers and bigger clusters posses larger out-of-plane moment indicating that the trimers to be the threshold size where out-of-plane magnetization appears.

In addition to the estimation of magnetic moment/atom, we fit the full $M(B)$ curves with a semi-classical model to extract magnetic anisotropy of each cluster size classes. As this is an independent approach to determine the easy axis, it is discussed separately in the next section.

Table 4.2: Magnetic moment ($\langle M_N \rangle$) and anisotropy (K_N) of the three cluster sizes. $\langle M_N \rangle$ and K_N are calculated from the fit of $\langle M_{\text{tot}}(\Theta) \rangle$, and of the magnetization curves, respectively.

N	$\langle M_N \rangle$ $\theta = 0°$ (μ_B/atom)	$\langle M_N \rangle$ $\theta = 55°$ (μ_B/atom)	Anisotropy K_N (meV/atom)	Orientation of easy axis/plane
1	1.6 ± 0.1	7.2 ± 0.1	-9.9 ± 0.9	In-plane
2	4.6 ± 0.8	6.4 ± 0.8	-1.9 ± 0.5	In-plane
≥ 3	7.2 ± 0.2	5.3 ± 0.2	2.9 ± 0.5	Out-of-plane

4.6.2 Semi-classical magnetic moment and anisotropy of different size groups

The descriptions of magnetic moment and effective anisotropy barrier for quantum systems such as single atoms and small clusters are conventionally done using an effective-spin Hamiltonian formalism [21, 105]. However, the presence of differently sized clusters at each coverage would require a separate set of exchange coupling and crystal field parameters for each size group. Therefore, the fitting of the magnetization curves using an effective-spin Hamiltonian approach would be largely overparametrized. As a convenient alternative, we adopt a semi-classical approach (see equation 4.2) where we assume ferromagnetic exchange interaction among the atoms within a cluster, and we replace the whole set of crystal field parameters with an average value of the magnetic anisotropy/atom [23]. This is justified

since Er single crystals are ferromagnetically ordered [99] below 19 K. Also note that, all magnetic clusters are considered as isolated and non-interacting objects. This is because the substrate mediated RKKY interactions amongst them are expected to be almost hundred times lower than what is known for the transition metals, as recently reported by Steinbrecher *et al.* from their investigations of Ho and Fe atoms on Pt(111) [70]. Knowing that the strength of RKKY interaction is as low as ≈ 0.1 meV for Fe atoms on Cu(111) [95], we can expect similar interactions among RE atoms on this substrate to be within an energy scale of μeV. Therefore they can be safely neglected for the temperature and magnetic fields used in this work. In addition we assume a constant modulus of the total moment/atom (Figure 4.5(a-c) and 4.12). With these assumptions, the magnetization curve for an ensemble of Er atoms and clusters reduces to:

$$M(B,\theta_0) = \sum_{\mathrm{N}=1,2,\geq 3} Q_N(\Theta)\widetilde{M}\frac{\int_0^{2\pi} d\phi \int_0^{\pi} \sin\theta\cos\theta \exp\left(E(B,\theta_0,\theta,\phi)/k_{\mathrm{B}}T\right)d\theta}{\int_0^{2\pi} d\phi \int_0^{\pi} \sin\theta \exp\left(E(B,\theta_0,\theta,\phi)/k_{\mathrm{B}}T\right)d\theta}, \tag{4.2}$$

where

$$E(B,\theta_0,\theta,\phi) = \overline{N}_N(\Theta)\widetilde{M}B\cos\theta + \overline{N}_N(\Theta)K_N(\sin\theta_0\sin\theta\cos\phi + \cos\theta_0\cos\theta)^2. \tag{4.3}$$

Here, $Q_N(\Theta)$ can be obtained from the three population growth model. The azimuthal and polar coordinates, respectively ϕ and θ, define the orientation of the semi-classical total magnetic moment/atom $\widetilde{M}$, which can be interpreted as the equivalent of $g\sqrt{J(J+1)}$. The quantity θ_0 defines the orientation of the B field with respect to the surface normal.

The total energy in equation 4.3 is the sum of the Zeeman and uniaxial anisotropy. The classical MAE/atom for a species of average size $\overline{N}_N(\Theta)$ is given by K_N. The average cluster size is 1 for the monomers and 2 for the dimers, while $\overline{N}_{\geq 3}$ was quantified in a coverage-dependent manner from our STM images, *i.e.*, $\overline{N}_{\geq 3} = 3.1 \pm 0.1$, 3.5 ± 0.1, 3.7 ± 0.1, and 4.1 ± 0.3 atoms, respectively for $\Theta = 0.02$, 0.032, 0.047, and 0.06 ML. Note that a positive (negative) K_N indicates an out-of-plane (in-plane) anisotropy.

According to our growth models, at $\Theta = 0.006$ ML 99.6% of the Er population is in the form of monomers. Therefore, the magnetization curves shown in Figure 4.12 give explicit access to their magnetic properties. Note that this coverage is amongst the smallest ones ever investigated with XMCD [23, 81]. So to quantify the semi-classical magnetic moment and anisotropy of the monomers, we performed a simultaneous fit to the full magnetization curves acquired at 0.006 ML using equation 4.2 (Figure 4.12). For the semiclassical magnetic moment ($\widetilde{M}$) and anisotropy (K_1) of the monomers we find $\widetilde{M} = 9.5 \pm 0.2\ \mu_{\mathrm{B}}$ and $K_1 = -9.9 \pm 0.9$ meV. This $\widetilde{M}$ is in perfect agreement with its theoretical value of $g\sqrt{J(J+1)} = 9.6\ \mu_{\mathrm{B}}$ with $J = \frac{15}{2}$ and

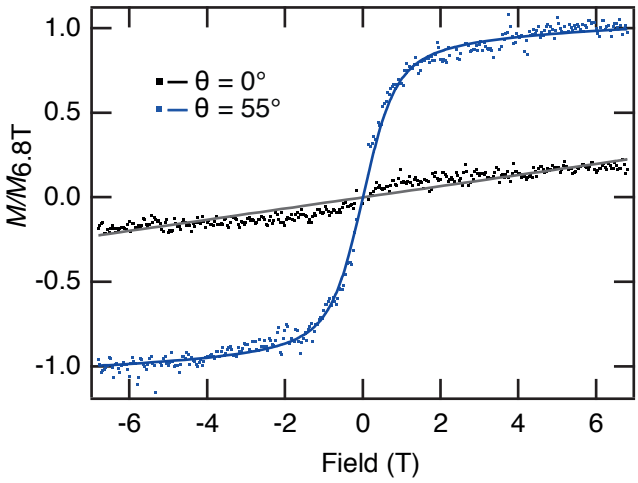

Figure 4.12: Magnetization curves at 0.006 ML. The large majority (99.6%) of the population is in the form of Er-monomers at this coverage. Dots: measurements; solid lines: semiclassical fits ($T = 2.5$ K).

$g = 1.2$.

The moment $\widetilde{M}$ can be interpreted as the semiclassical equivalent of $g\sqrt{J(J+1)}$. This should not be directly compared with the $\langle M_{tot} \rangle$ obtained from the sum rules, which is instead a component of the total moment projected along the beam. Similarly, the classical anisotropy barrier K_1 should be interpreted as an estimate of the energy between the lowest and the highest state within a given multiplet for systems with purely uniaxial anisotropy. Hence this is not comparable to the zero field splitting (ZFS) which corresponds to the energy difference between ground state and first excited state.

Since J remains constant irrespective of the cluster size, and so does the semi-classical magnetic moment/atom $\widetilde{M}$, we fix $\widetilde{M} = 9.5\ \mu_B$ for all size groups as the one found for the monomers. With this, we extract the MAE/atom of the dimers (K_2) and bigger clusters ($K_{\geq 3}$) from the simultaneous fit of the magnetization curves for $\Theta = 0.015$, 0.035, and 0.045 ML for the two angles of incidence. Solid lines in Figure 4.5 (a-c) are these fits and the corresponding MAE values are tabulated in Table 4.2.

To summarize, larger in-plane than out-of-plane moment is obtained for $N \leq 2$. This is also coherent with the corresponding negative values of K_N which imply out-of-plane hard axis for these species. In contrast, clusters with $N \geq 3$ possess larger out-of-plane moment and positive K_N, indicating an out-of-plane easy axis. Note that the MAE/atom of the Er dimers is significantly lower than the one of the single atoms, in contrast to what has been reported for Gd dimers on the same substrate [36].

4.6.3 The minimum cluster size required for magnetic hysteresis

To identify the minimum cluster size that causes magnetic hysteresis, we quantified the coverage dependent area of the hysteresis loops at $\theta = 0°$ (Figure 4.13). Since the magnetization is in-plane for $N \leq 2$ while the maximum opening of the hysteresis is observed in the out-of-plane direction, monomers and dimers cannot be the origin of hysteresis. To understand whether $N = 3$ belongs to the size group causing hysteresis, we used the four population growth model considering $N = 1, 2, 3$, and ≥ 4. A careful analysis of the apparent cluster heights and shapes allows us to clearly distinguish the trimers from $N \geq 4$ species as shown in Figure B.5. Interested readers may refer to appendix B.2 for further details and the validity of the four population growth model.

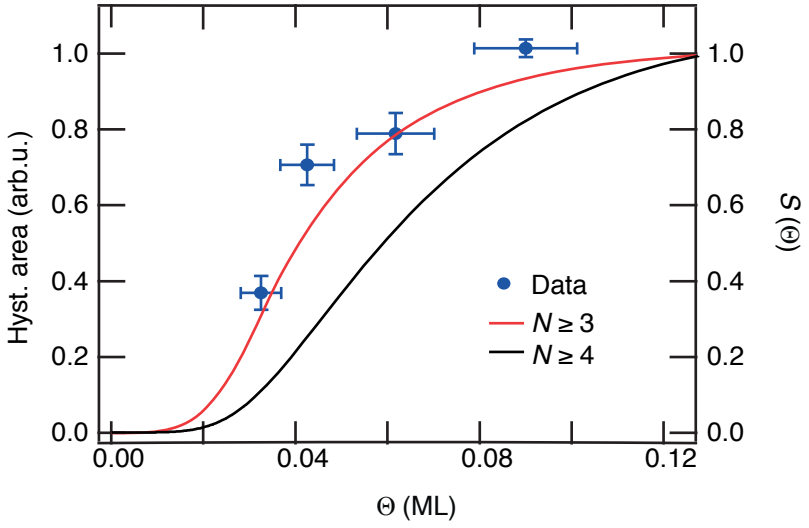

Figure 4.13: Comparison of the hysteresis area (dots) with the weighted contribution to the total XMCD in normal incidence, $S(\Theta)$, for $N \geq 3$ and $N \geq 4$ (full lines).

In order to correlate the onset of hysteresis with the appearance of a given cluster size, we calculated the contributions to the out-of-plane XMCD from clusters with $N \geq 3$ and $N \geq 4$ weighted by their relative abundance $Q_N(\Theta)$. We define this as $S(\Theta)$, where

$$S(\Theta) = \begin{cases} Q_{\geq 3}(\Theta)\,\frac{\langle M_{\geq 3}\rangle}{\langle M_{\mathrm{tot}}(\Theta)\rangle} & \text{for } N \geq 3 \\ Q_{\geq 4}(\Theta)\,\frac{\langle M_{\geq 4}\rangle}{\langle M_{\mathrm{tot}}(\Theta)\rangle} & \text{for } N \geq 4 \end{cases} \tag{4.4}$$

Here $\langle M_{\geq 3}\rangle$ and $\langle M_{\geq 4}\rangle$ are the values obtained from the fits of $\langle M_{\mathrm{tot}}(\Theta)\rangle$ using the three and four population model. Figure 4.13 shows that the signal expected from the species with $N \geq 3$ has excellent agreement with the onset and the overall trend of the hysteresis opening. Exclusion of the trimers shows a hysteresis onset at significantly higher coverage than the one observed experimentally. This implies that all clusters bigger than dimers contribute to the

observed magnetic hysteresis, the trimers ($N = 3$) being the smallest of all.

As a final verification, we checked whether the MAE/atom for the $N \geq 3$ species is consistent with the observed magnetic hysteresis. This is done by extracting $K_{\geq 3}$ from the experimentally observed switching fields [106] assuming ferromagnetic exchange interaction within a cluster. The switching fields can be expressed as,

$$H_{\text{switch}} = \frac{2K_{\geq 3}}{\widetilde{M}} \left(1 - \sqrt{\frac{k_{\text{B}} T}{\overline{N}_{\geq 3}(\Theta) K_{\geq 3}} \log \frac{t}{\tau_0}} \right) \tag{4.5}$$

Here, H_{switch} is the field at which the hysteresis closes and t defines the time required for the acquisition of a magnetization curve between 0 T and H_{switch} which is 2.7 minutes in our case. Knowing $\widetilde{M}$ and $\overline{N}_{\geq 3}(\Theta)$ and assuming the prefactor $\tau_0 = 10^{-10}$ s [107], we obtain $K_{\geq 3} = 2.4 \pm 0.1$ meV/atom. This estimation is independent of the growth model and yet is in good agreement with the value obtained from the fits to the full magnetization curves (Table 4.2). Therefore it confirms the consistency of our analysis.

Chapter summary

- The easy magnetization axis of Er on Cu(111) changes from in-plane for the single atoms ($N = 1$) and dimers ($N = 2$) to out-of-plane for trimers ($N = 3$) and bigger clusters ($N \geq 3$).
- The observed change in the easy axis occurs due to the modified ligand field environment induced by the increased atomic coordination [98].
- The trimer ($N = 3$) is the threshold size for the onset of magnetic hysteresis. The out-of-plane magnetization, the ferromagnetic exchange interaction among the atoms, and a MAE barrier of 2.9 meV/atom in the trimers, introduce a magnetic lifetime of 2 minutes at 2.5 K and 0.1 T.
- Together with Fe trimers on Pt(111) [70, 108], the Er trimers on Cu(111) reported here constitute the smallest surface-adsorbed stable ferromagnets directly adsorbed on a metal substrate.

5 Insulating substrate: spin-excitations in RE-TM heterodimers

In the previous chapters we have demonstrated the effects of RE-RE interactions as well as RE-substrate interaction in determining the magnetic properties of the RE atoms absorbed on metal substrates. Now we will focus on the magnetic properties of low-coordinated RE atoms adsorbed on thin insulting layers of MgO(100) grown on top of Ag(100) substrate. The corresponding manuscript "Spin-excitations in $4f-3d$ heterodimers adsorbed on MgO/Ag(100)" by A. Singha, F. Donati, C. Wäckerlin *et al.*, is in preparation.

Work contribution

I have performed the STM experiments presented in this chapter under the supervision of Dr. Fabio Donati. The spin Hamiltonian model presented in section 5.3 was realized with the help of Dr. Fabio Donati. The preliminary DFT calculation mentioned in section 5.3 was performed in collaboration with the group of Professor Ž. Šljivančanin in Vinča Institute of Nuclear Sciences, Serbia.

5.1 Introduction

As explained in the Introduction of this thesis, RE atoms are arguably one of the most appealing candidates for studying quantum magnetic properties in low dimensional systems. However the $4f$ electrons that carry the magnetic signature of the REs are hardly accessible with conventional scanning probes owing to their highly localized nature. Recent studies using STM indicates that it is unlikely to have a significant contribution from the $4f$ electrons in the tunnelling current [70, 71], although, the spin contrast in the $4f$ shell can be indirectly probed via the polarized external spd shells. This has been measured as the telegraphic signals by Natterer *et al.* [109]. Moreover, indirect measurements of the magnetic moment is possible through dipolar coupling between the RE and TM atom placed nearby as it has been recently demonstrated using single-atom electron paramagnetic resonance (EPR) technique [109]. A direct access to the magnetic levels' splitting and therefore to the origin of magnetic anisotropy

of surface-supported single atoms can be obtained from spin-excitation spectroscopy (SES). However, no SES of surface-supported REs has been clearly demonstrated yet [37, 70].

The $4f$ electrons in the REs can be coupled through exchange interaction to their external $5d$ electrons [110]. Moreover the previous works on RE-TM compounds suggest that the REs can couple to $3d$ atoms typically through $5d$-$3d$ hybridization [71, 110]. This invokes the idea of studying the properties of $4f$ electrons with STM using surface-supported $4f$-$3d$ heterodimers. The key difference between this approach and the one used in ref. [109] is that the $4f$ element is an integral part of the heterodimer and is directly probed instead of an indirect, non-local measurement through a nearby $3d$ atom. For this we chose Ho-Co dimers as a model system and studied them by adsorbing on an insulating layer of MgO on a Ag(100) substrate. The key purpose of the insulating layer is to decouple the magnetic states from the scattering of substrate's conduction electrons and phonons. This is further elaborated in sections 6.1 and 6.2. The rationale behind choosing the Ho and Co atoms on this particular substrate are listed in the following:

- We have recently achieved record large magnetic hysteresis for single Ho atoms on MgO/Ag(100) (interested readers may refer to section 6.1, ref. [41], and the supplementary information therein, for further details).
- Co atoms on MgO show record high anisotropy of 58 meV [33].
- For the particular choice of the substrate, the spectroscopic signature of Co atoms and dimers are already well known [33, 34]. This reduces the number of unknowns in identifying the Ho-Co heterodimers on this surface.

5.2 Low temperature STM Measurements

5.2.1 Ho atoms adsorbed on MgO/Ag(100)

For the STM measurements on the Ho-Co dimers, we first deposited Ho atoms on MgO layers grown on Ag(100) single crystal. Details of the MgO growth are provided in section 2.1.1 and in references [41, 111]. Depending on the adsorption site, the Ho atoms can posses different apparent heights as evident from Figure 5.1 a. The Ho atoms adsorbed on O-top site appear smaller than those adsorbed on the bridge sites. The former will be called as Ho^{Top} and the latter as Ho^{Bridge} hereafter. On thicker MgO layers ($\geq$ 2 ML) the abundance of Ho^{Top} is significantly larger than Ho^{Bridge} (see references [41, 112] for further illustration). We have also encountered some Ho-Ho dimers grown either by statistical means or by tip-induced manipulation of the local surface area. The Ho-Ho dimers can be easily recognized from their characteristic inelastic step in the conductance at around $\pm$85 meV. This will be discussed later in section 5.4.2. In contrast, the Ho atoms are devoid of any inelastic structure irrespective of their adsorption site, possibly due to the poor accessibility of the inner shell $4f$ electrons (Figure 5.1 b).

5.2.2 Addition of Co atoms

Upon characterizing the sample with Ho-only species, we subsequently deposit Co atoms on the same surface. This enables us to obtain three more different species: Co atoms, Co-Co dimers, and Ho-Co heterodimers (Figure 5.1 a). The Co atoms and Co-Co dimers can be easily identified from their known spectroscopic features [33]. The spin-excitation of Co atoms (appearing as a step jump at around 58 meV in Figure 5.1 b) has already been reported by Rau *et al.* in ref. [33]. The corresponding homodimers (Co-Co) also show an inelastic step at around 13 meV. This was first mentioned in the thesis of Dr. Sausanne Baumann [34]. However the magnetic origin of this step has not been demonstrated yet and this will be discussed in section 5.4.1.

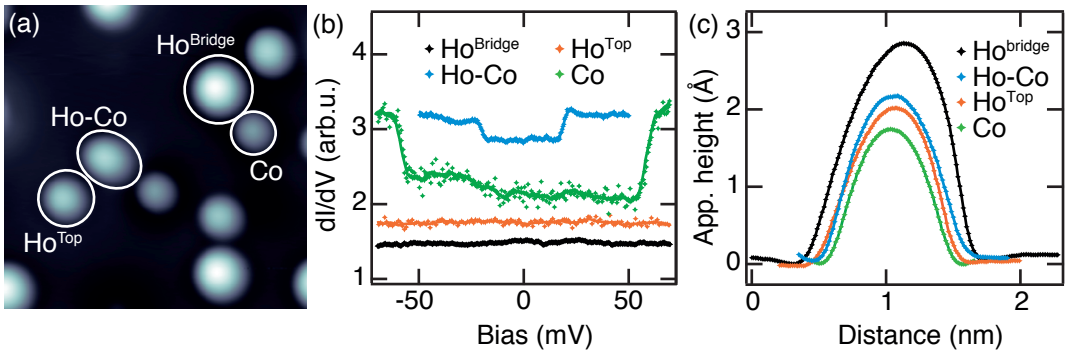

Figure 5.1: (a) STM image showing the different species adsorbed on 1 ML of MgO/Ag(100). V_t = 100 meV, I_t = 50 pA, B = 6 T, T = 4.3 K, and the image size is 6 × 6 nm^2. (b) dI/dV spectroscopy of Ho^{Top}, Ho^{Bridge}, Co atom, with V_t = 100 meV and I_t = 500 pA and Ho-Co dimer with V_t = 40 meV and I_t = 250 pA. For all spectra V_{mod} = 1 meV peak-to-peak, and T = 4 K. Spectra are vertically offset for clarity. (c) The apparent height profiles of Ho^{Bridge}, Ho^{Top}, Co, and Ho-Co dimer.

5.2.3 Identification of Ho-Co dimers

The most compelling fingerprint of the Ho-Co heterodimer comes from its characteristic dI/dV spectra. Distinct from the spectroscopic signatures of all the other species, the heterodimers exhibit an inelastic step at around ±20 meV (Figure 5.1b). In addition, STM provides further details of the apparent heights, structure, and orientations of the Ho-Co dimers with respect to the underlying MgO lattice. We can distinguish the Ho-Co dimers from the Ho^{Bridge}, Ho^{Top}, and Co atoms using their distinct apparent heights as shown in Figure 5.1 c. Overlaying an atomic resolution image of MgO with a larger scan area containing a heterodimer reveals that the dimer-axis is aligned with MgO sublattice (Figure 5.2 a). Moreover we notice a characteristic asymmetry in its shape. Due to the four-fold symmetry of MgO(100), only four orientations are viable for these Ho-Co heterodimers. These different orientations can also be identified following the shape asymmetry as shown in Figure 5.2 b.

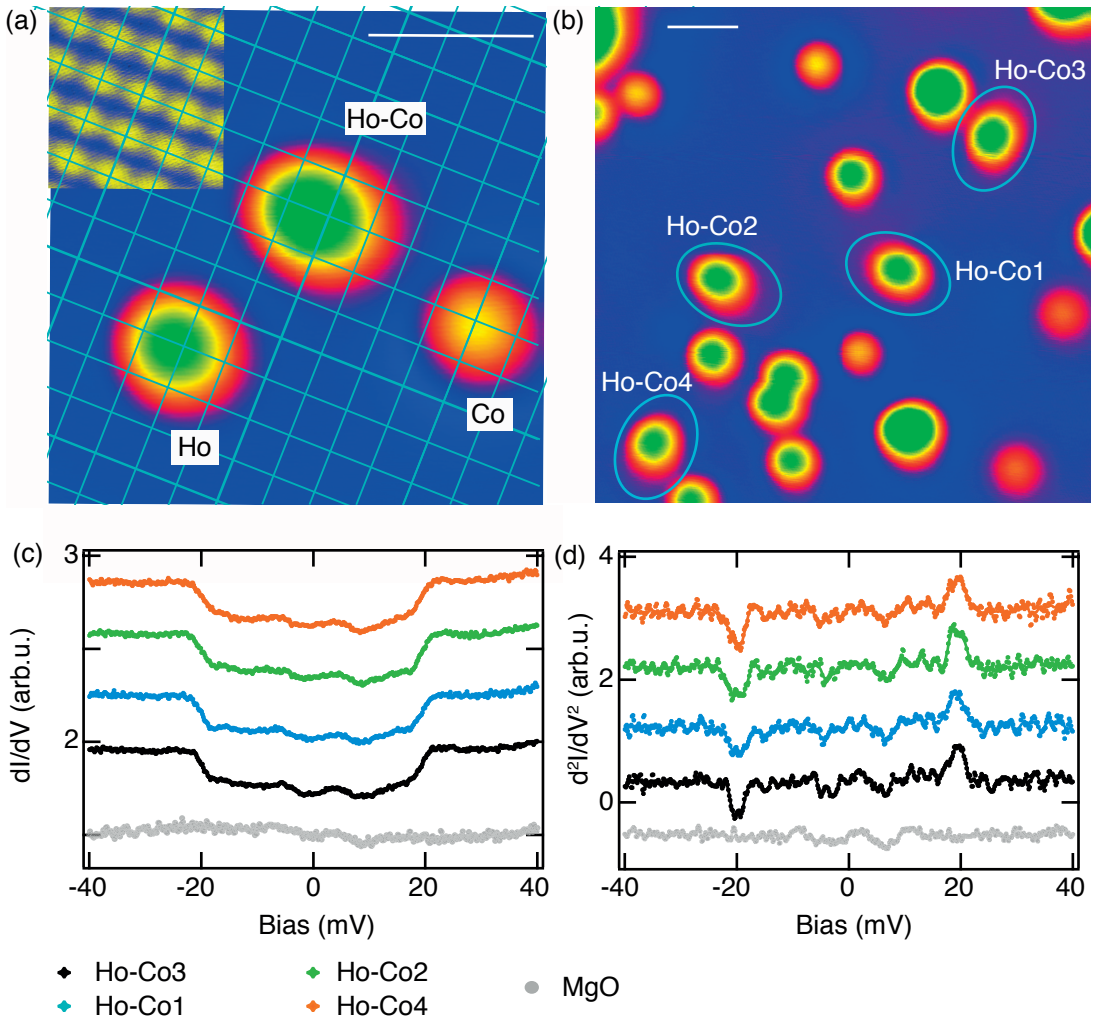

Figure 5.2: (a) STM image highlighting the characteristic asymmetric shape of a Ho-Co dimer, and (b) the four possible orientations of the heterodimers on the MgO/Ag(100) surface. Inset shows an atomic resolution image of a small 2 ML patch of MgO. The cyan grid is aligned to match the center of the Co atom, thus marking the O sites of the MgO substrate. For the inset $V_t = 10$ meV, $I_t = 8$ nA. For the rest of the panels $V_t = 100$ meV, $I_t = 50$ pA, and $B = 6$ T, and the scale bars indicate 1 nm. (c) dI/dV spectroscopy on the four differently oriented Ho-Co dimers shown in (b). (d) d^2I/dV^2 spectra numerically derived from (c). Spectra are offset for clarity. $V_t = 40$ meV, $I_t = 250$ pA, $V_{mod} = 1$ meV peak-to-peak, and $B = 8$ T. $T = 4.3$ K for all panels. Each dI/dV spectra represents an average of 5 acquisitions on the same Ho-Co dimer.

The inelastic feature at ±20 meV is present in all the four heterodimers with the different orientations, as illustrated in Figure 5.2c. From numerical derivation of such spectra, we obtain the corresponding d^2I/dV^2 signals (Figure 5.2d). The steps observed in the dI/dV appear as a pair of peak-dip feature in the d^2I/dV^2, symmetrically positioned around the zero bias. From Gaussian fits to these peak-dip features we obtain the precise position of the

Table 5.1: Energy position of the inelastic step obtained for the four Ho-Co dimers shown in Figure 5.2 b. $B = 8$ T, $T = 4.3$ K. Error bars account for the standard deviation obtained from at least five acquisitions on the same heterodimer.

Ho-Co dimers	E (meV)
Ho-Co1	19.70 ± 0.05
Ho-Co2	19.73 ± 0.05
Ho-Co3	19.48 ± 0.13
Ho-Co4	19.40 ± 0.09

steps. These are reported in Table 5.1. Note that the species identified as Ho-Co dimers are not present unless both Ho and Co are evaporated. This provides further certainty for them to be the heterodimers.

5.2.4 Spin-excitations in Ho-Co dimers

We have confirmed the magnetic origin behind the observed inelastic step by studying the field-dependent dI/dV spectra. This inelastic step progressively shifts in presence of an out-of-plane magnetic field (B). Figure 5.3 a highlights the shift by zooming in the dI/dV spectra measured at 0.4 K. From the numerically derived d^2I/dV^2 spectra, we have quantified a shift of 1.1 meV for $\delta B = 7$ T at $T = 4$ K.

In order to calculate the g factor for these heterodimers, we have gathered statistics on the B field-dependent spin-excitations on several heterodimers. Figure 5.3 b shows the spin-excitation step positions E *vs.* B. Each points on this plot is obtained by averaging the positive and negative values of the bias which were known from the Gaussian fits to the corresponding peak-dip features in the d^2I/dV^2 signal. The calculation of the g factor then follows from the

Table 5.2: The g factors measured for the different heterodimers adsorbed on 1 and 2 ML of MgO. The values obtained from the linear regression of the data shown in 5.3(b) are presented in the 3^{rd} column along with the uncertainties on the corresponding fits σ_i. The last column shows the mean value of the g factor together with the corresponding standard deviation calculated as $\sqrt{\sum_i^N (\sigma_i^2/N)}$, where N denotes the total number of cases.

MgO thickness (ML)	Species	g factor	average g factor
1	Ho-Co1	2.9 ± 0.3	3.1 ± 0.3
	Ho-Co2	2.9 ± 0.2	
	Ho-Co3	3.4 ± 0.3	
	Ho-Co4	3.2 ± 0.2	
2	Ho-Co5	2.4 ± 0.4	2.5 ± 0.6
	Ho-Co6	2.5 ± 0.4	
	Ho-Co7	2.8 ± 0.9	

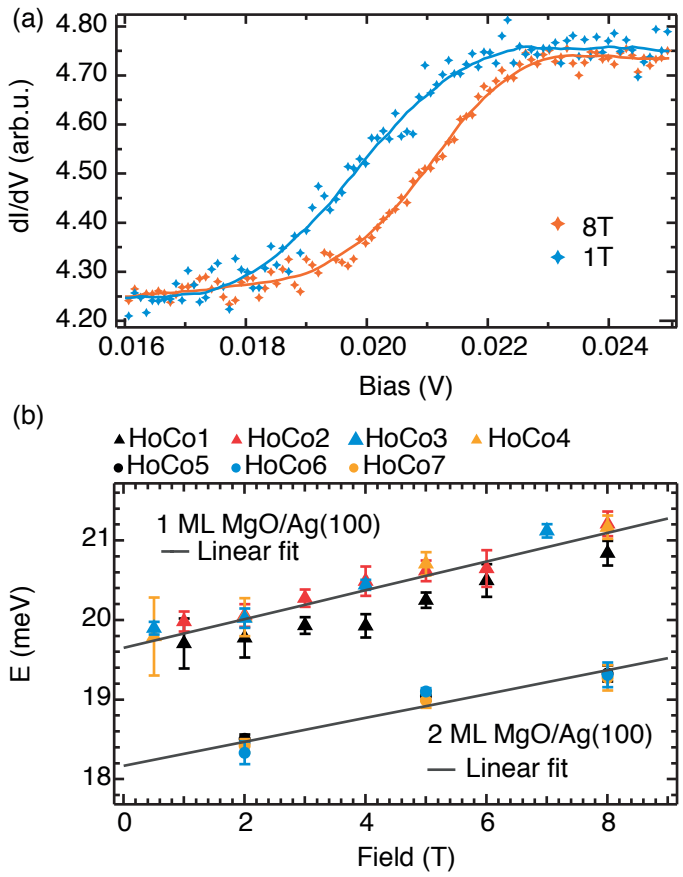

Figure 5.3: Magnetic field dependence of the inelastic step shown by zooming on the characteristic (a) dI/dV (dots: raw data; lines: smoothened). Each dI/dV spectra represents an average of 10 acquisitions on the same Ho-Co dimer. $V_t = 30$ meV, $I_t = 750$ pA, $V_{mod} = 500$ μV peak-to-peak, and $T = 0.4$ K. The full Zeeman plot is shown in (b) for four Ho-Co dimers adsorbed on 1 ML of MgO/Ag(100) and three Ho-Co dimers on 2 ML of MgO/Ag(100). Gray lines are the mean slopes in each case. Error bars shown in represent the standard deviation from at least 5 measurements on the same heterodimer. $T = 4$ K for (c) and (d).

linear regression of this data using the following expression: $E = \Delta J_z \times g \times B \times \mu_B$. Here μ_B is the Bohr magneton. We determine an average value of $g = 3.1 \pm 0.3$, considering an inelastic transition that changes J_z by $\Delta J_z = 1$ (Table 5.2). The obtained g factor strongly differs from the free electron g value of 2, however, notably this only represents an effective g factor for the transition. Note that the inelastic step of Ho-Co2 is systematically shifted by about -0.2 meV compared to the rest of the heterodimers adsorbed on 1 ML MgO. This is only 10% of the change expected to arise from the difference in the MgO thickness (described in the next paragraph). We can ascribe this to the difference in the local environment of this heterodimer compared to the rests.

We also observe marked dependence of the threshold energy for the inelastic transition on

the MgO thickness. Our measurements on several heterodimers adsorbed on both 1 ML and 2 ML MgO evidence that the positions of the spin-excitation steps are systematically down shifted in energy when the heterodimers are adsorbed on 2 ML MgO (Figure 5.3 b). At 8 T the difference in the step position is about 1.7 meV. The difference in the spin-excitation energy as a function of MgO thickness has also been reported for Fe atoms adsorbed on MgO/Ag(100) by Paul *et al.* [113] and this has been attributed to the local changes in the CF parameters on the thicker layers. We also obtain a slightly different value of the g factor, *i.e.*, $g = 2.5 \pm 0.6$ (Table 5.2). Consistent with the case of 1 ML MgO, this mean g factor is different from the free electron's g value of 2. The large g factors can be reproduced following an effective spin Hamiltonian model. This will be described later in section 5.3.

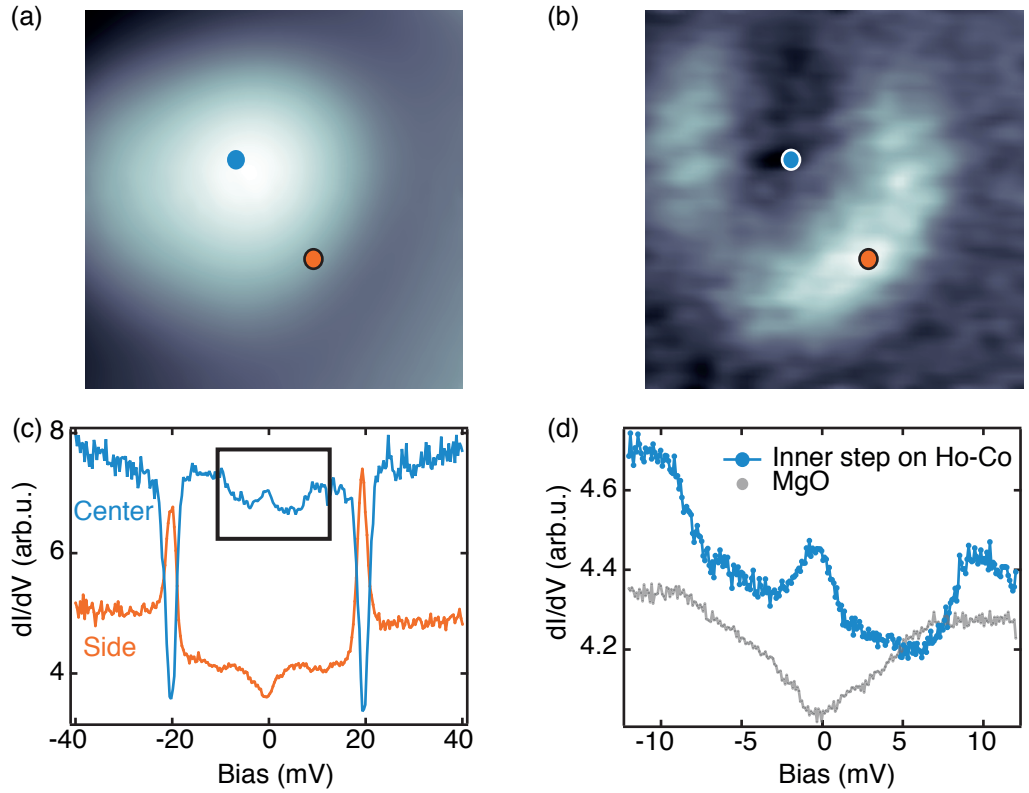

Figure 5.4: (a) STM image of a Ho-Co dimer and the (b) dI/dV map of the same. $V_t = 20$ meV and $I_t = 100$ pA. Image size 1.5×1.5 nm^2. (c) dI/dV spectra measured with a spin-polarized tip on the different spots of the Ho-Co dimer shown in (a). In addition to the jagged inelastic features at ± 20 meV, a pair of inner steps are detected at about ± 8 meV. $V_t = 40$ meV, $I_t = 1$ nA, and $V_{mod} = 500$ μV peak-to-peak. (d) The zoom on the inner step shown in (c) with $V_t =$ 15 meV, $I_t = 300$ pA, and $V_{mod} = 200$ μV peak-to-peak. $B = 8$ T and $T = 0.4$ K for all panels.

We have also explored the spin-excitation of these heterodimers using a spin-polarized tip (SP-tip). The spin-polarized tip can be easily made by picking up multiple Co atoms from the same surface. The spin-polarization of the tip can be confirmed by checking the "overshooting" in the Co spectra at 58 meV. The "overshooting" comes from the spin-pumping as explained in

the doctoral thesis of Dr. Sausanne Baumann [34], and this provides information about the lower bound of the lifetime of the excited state. Figure 5.4 a shows the STM image of a Ho-Co heterodimer using such SP-tip. The corresponding dI/dV map is shown in Figure 5.4 b. One can immediately discern that the different parts of the heterodimer appears with different contrast due to the varied degree of overlap of the tip wavefunction with the ones of the heterodimer. We also see that the appearance of the dI/dV spectra changes depending upon the spatial location of the tip during the acquisition of the spectra. When the tip is placed close to the center of the heterodimer, a pair of symmetrically positioned dips are found at the position of the inelastic steps (±20 meV). We name this as the "negatively jagged" case (Figure 5.4 c). In contrast, two strongly peaked features are found at the same energy when the tip is placed at the side. We can call this as "positively-jagged" case (Figure 5.4 c). Interestingly only for the "negatively jagged" case, we have identified an additional pair of inner steps in the conductance at around ±8 meV, which are symmetrically positioned around the zero bias. For the "positively jagged" case, these steps are barely detectable (Figure 5.4 c). Moreover, these inner steps were absent when probed with a non SP-tip. This indicates that the corresponding transition intensity is too weak to be detected as inelastic steps using a non SP-tip. In section 5.3 we are going to find out that these inner steps eventually arise from another inelastic transition within the same ground state multiplet of the heterodimers.

5.3 Spin-excitations in Ho-Co: the spin Hamiltonian approach

We have employed an effective spin Hamiltonian model in order to identify whether the evidence of spin excitation in the Ho-Co dimers at 20 meV reflects the magnetic anisotropy energy or the strength of the exchange coupling between Ho and Co atom within the dimer. A detailed mathematical description of the spin Hamiltonian formalism is provided in section 2.2.3.

The spin Hamiltonian describing two exchanged coupled spins, $\hat{S}_1$ and $\hat{S}_2$ respectively, can be expressed as the following:

$$\hat{H} = D\hat{S}_{zc}^2 + J_c(\hat{S}_1 \cdot \hat{S}_2) + \mu_B[g_1\hat{S}_{z1} + g_2\hat{S}_{z2}] \cdot \vec{B} \tag{5.1}$$

where

$$\hat{S}_1 \cdot \hat{S}_2 = \hat{S}_{x1} \cdot \hat{S}_{x2} + \hat{S}_{y1} \cdot \hat{S}_{y2} + \hat{S}_{z1} \cdot \hat{S}_{z2} \tag{5.2}$$

Here $\hat{S}_{z1}, \hat{S}_{z2}$, and $\hat{S}_{zc}$ are functions of the magnitude of the two effective spins, s_1 and s_2 and they are defined within the density matrix formalism as described in section 2.2.3. The Hamiltonian in equation 5.1 resembles equation 2.27, the only difference being $D' = D_1 = D_2 = C = 0$. These have been considered to allow simplification and to avoid overparametrization. The spin Hamitonian is essentially divided in three types of terms. The overall uniaxial

anisotropy of the dimer is expressed as D. The sign convention of the D parameter is such that, a negative (positive) value indicates out-of-plane (in-plane) magnetic anisotropy. The coupling parameter J_c defines the strength of the exchange interaction between the two atoms. In this case, a negative value indicates ferromagnetic (FM) exchange coupling and *vice versa*. Finally the g factors of the individual atoms appear in the Zeeman term as g_1 and g_2.

The preliminary DFT calculations, performed in the group of Professor Ž. Šljivančanin in Vinča Institute of Nuclear Sciences, Serbia, indicate that the ground state of the Ho-Co dimers corresponds to their flat lying geometry on the MgO surface. Moreover, it predicts a ferromagnetic exchange coupling between Ho and Co atom. This helps us fixing the sign of coupling constant J_c. Further to this, for simplicity and to avoid overparameterization, we will assume the following in our model spin Hamiltonian:

- only uniaxial anisotropy along z, *i.e.*, the off-diagonal terms of the CF are zero [a]
- $s_1 = 8$, *i.e.* the maximum total (spin + orbital) magnetic moment for the $4f^{10}$ configuration of the atomic Ho
- $g_1 = 10/8 = 1.25$, corresponding to the $4f^{10}$ configuration of the Ho atom
- $s_2 = 3/2$, *i.e.* the maximum spin magnetic moment of the Co atom in $3d^7$ configuration [b].

Altogether these leave D, $|J_c|$, and g_2 as the only degrees of freedom for establishing the spin Hamiltonian model. Note that equation 5.1 only considers terms that describe only collinear interactions defined with dot products of the spin operators. In order to explore the possibilities of complex orientations among the adjacent spins, one can also include non-collinear terms in the spin Hamiltonian, such as Dzyaloshinskii-Moriya interaction [108, 114]. However, this would necessitate optimization with a larger set of parameters. Therefore in order to avoid overparametrization, we have not considered this in the present model.

Figure 5.5 a shows the energy distribution of the magnetic levels at 0 T that can explain the experimentally observed inelastic steps at ±20 and ±8 meV in the heterodimers. This energy diagram has been obtained by considering an out-of-plane anisotropy with $D = -0.45$ meV, FM coupling strength of $J_c = -1.25$ meV, and $g_2 = 3$. This g_2 corresponds to an effective spin moment of $3 \times (3/2) = 4.5\ \mu_B$, and thereby an effective orbital moment of $1.5\mu_B$, assuming $6\ \mu_B$ as the total moment of atomic Co in $3d^7$ configuration following Hund's rules. In other words,

[a] Note the large g factor as well as the position of the inelastic steps can also be reproduced with a non-vanishing first order off-diagonal term, *i.e.* $E(S_x^2 - S_y^2)$. However, SES is only sensitive to $\delta J_z = 0, \pm 1$ transitions. Therefore with the two experimentally observed inelastic steps we can reliably reproduce only the lowest part of the full multiplet structure, without being sensitive to its overall shape. As the in-plane term E largely governs the mixing of the states and therefore influences the overall shape of the full multiplet structure, we can not comment on the corresponding value with large confidence (see Appendix C.1).

[b] As the SO coupling in TMs is significantly weaker than in REs, the total magnetic moment is not a good quantum number. Therefore we only consider the spin magnetic moment, whereas we account for the non-vanishing orbital component indirectly through the corresponding spin g factor namely, g_2.

this implies that the orbital moment of Co is not fully quenched which is markedly different than what is known for the conventional $3d$ bulk materials.

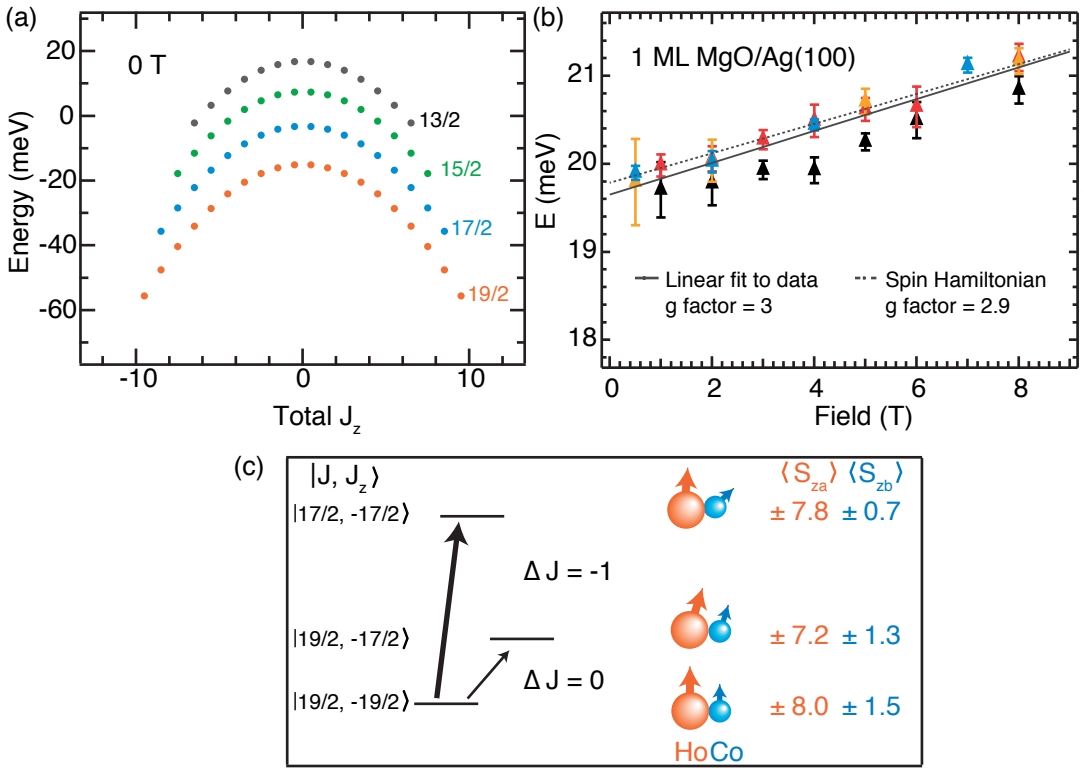

Figure 5.5: (a) Simulated energy distribution of the magnetic levels of the Ho-Co heterodimer at zero magnetic field. (b) The simulated Zeeman shift of the 20 meV transition and the linear fit to the data indicate $g = 2.9$. For comparison, the experimental data for 1 ML MgO from Figure 5.3b, are overlaid together with the corresponding mean fit. (c) Schematic illustrating the origin behind the two inelastic steps measured at around ±20 and ±8 meV. The former comes from a $\Delta J = -1$ transition, shown as a thick black arrow, while the latter comes from a $\Delta J = 0$ transition, shown with a thinner arrow. The orientation of the individual magnetic moments of Ho and Co in the given magnetic states are depicted schematically on the right.

The magnetic anisotropy barrier appears as an inverted parabola due to the negative sign of the D parameter. As expected for coupling between two spins of magnitude $s_1 = 8$ and $s_2 = 3/2$, we have obtained $(2s_1+1)(2s_2+1) = 68$ levels in total. Moreover, following the rules of coupling angular momenta the total momentum J discretely varies from $|s_1+s_2|$ to $|s_1-s_2|$ in steps of 1. The value of J defines the multiplicity of each multiplets as $2J+1$. This explains the reason behind the typical distribution of the levels in four distinct multiplets with $2(s_1+s_2)+1 = 20$ states in the lowest multiplet and $2(s_1-s_2)+1 = 14$ states in the highest one. The corresponding value of J is indicated next to each multiplets specified in different colours in Figure 5.5 a.

Given this energy level distribution, only two inelastic transitions are possible. Note that during the spin-excitations process the system is excited from ground state to an excited state

and such transitions allow only specific changes in the magnetic moment of the system, *i.e.*, $\Delta J_z = 0, \pm 1$. In the present case, this can be achieved either from transitions between the lowest two multiplets, *i.e.*, $\Delta J = -1$, or from transitions between the lowest two sublevels within the ground state multiplet, *i.e.*, $\Delta J = 0$. In Figure 5.5 c, these are schematically shown as thicker and thinner arrow respectively. At 0 T, the related energy gap in the former case ($|19/2, \pm 19/2\rangle \rightarrow |17/2, \pm 17/2\rangle$) is 19.9 meV and it is 8.1 meV for the latter ($|19/2, \pm 19/2\rangle \rightarrow |19/2, \pm 17/2\rangle$). These are in good agreement with the positions of the inelastic steps measured experimentally.

We have further quantified the contribution of both Ho and Co atom to the z projection of the total magnetic moment, J_z, by computing the expectation value of $\hat{S}_{z1}(s_1, s_2)$ and $\hat{S}_{z2}(s_1, s_2)$ using the density matrix formalism (see section 2.2.3 for details). Thus for Ho we obtain ± 7.8 and $\pm 7.2\ \hbar$ for $|17/2, \pm 17/2\rangle$ and $|19/2, \pm 17/2\rangle$ states respectively, while Co contributes ± 0.7 and $\pm 1.3\ \hbar$ in those states (Figure 5.5 c). This indicates that the prominent inelastic transition observed at ± 20 meV is dominated by the large (almost 55%) change in the spin moment of Co, while the moment of Ho changes only minimally. This further suggests that this transition is related to the exchange interaction between the atoms in the dimer (Figure 5.5 c). On the contrary, when the change of magnetic moment is mostly taken by the Ho atom for the transition related to the inner step at ± 8 meV, the spin-excitation is very weak and only measurable with a SP-tip.

Finally we have verified the value of overall g factor of the heterodimer by reproducing the full Zeeman plot of the main transition at ± 20 meV (Figure 5.5 b). From the linear fit to this data, we have obtained $g = 2.9$, in very good agreement with our experimental observation. Assumption of an anti-ferromagnetic (AF) coupling would result into an effective g-factor which is smaller than 2. Therefore, independently from the predictions of DFT, this confirms the FM coupling between Ho and Co. However note that the FM coupling is quite unusual compared to the bulk $3d-4f$ compounds of the late lanthanides. In those cases a ferrimagnetic exchange interaction is expected as explained in ref. [115].

Note that the choices of the magnetic moments and g_1 for building the spin Hamiltonian model are not unique. In fact, we can also reproduce the positions of the inelastic steps as well as the large g factor with at least another set of values, namely $s_1 = 15/2, s_2 = 3/2$, and $g_1 = 1.2$. In that case we have to choose $D = -0.52$ meV, $J_c = -1.35$ meV, and $g_2 = 3$. All results of the model with this different set of parameters remain the same apart from the projected spin moment of Co for the $\delta J = -1$ transition, which is reduced by almost 90% (in contrast to the 55% mentioned above). Nevertheless, this does not influence the interpretation about the observed inelastic steps for $\delta J = 0, -1$ transitions and the nature of exchange coupling between the Ho and Co atom.

5.4 Inelastic excitations in homodimers

5.4.1 Co-Co dimers

Similar to the Ho-Co dimers, we have also investigated the magnetic field-dependent dI/dV spectroscopy of the Co-Co dimers. Also in this case the inelastic step at around 13 meV shifts due to the change in the external out-of-plane B field.

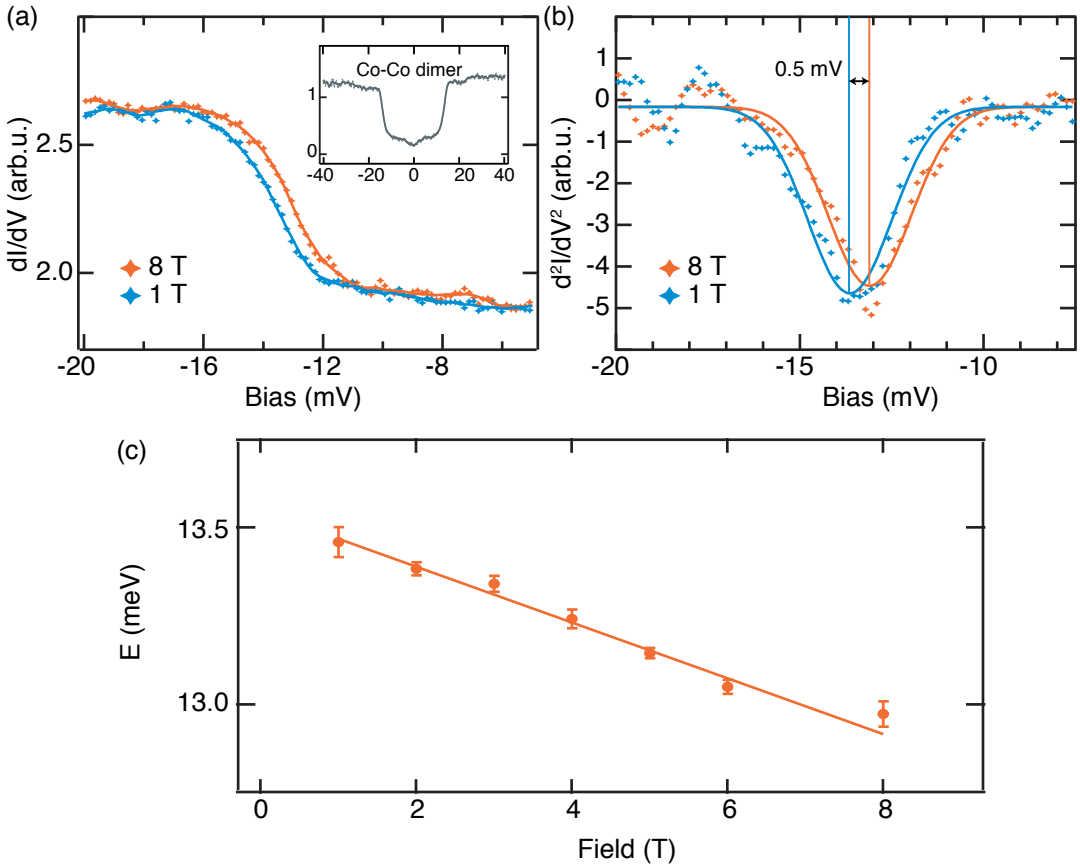

Figure 5.6: Zoom of the magnetic field dependent (a) dI/dV and (b) d^2I/dV^2 spectra of Co-Co dimers. Inset of (a) shows the full range dI/dV spectra. $V_t = 40$ meV, $I_t = 250$ pA, and $V_{mod} = 1$ meV peak-to-peak. The full Zeeman series indicating the linear shift of the inelastic feature with the external magnetic field is shown in (c). $T = 4.3$ K for all panels.

However, in contrast to the Ho-Co dimers, the steps shift to lower energies with increasing B field as illustrated in Figure 5.6 a and b. From the overall Zeeman plot, we obtain a total shift of -0.5 meV for $\delta B = 7$ T and an effective g factor of 1.3 (Figure 5.6 c). The shift of the inelastic steps towards the lower energy might arise from an antiferromagnetic exchange interaction between the Co atoms within the dimer. Further theoretical insights are required (a) to determine the magnetic moments and (b) the nature of the exchange coupling between the two Co atoms within the dimer. Knowing these information, we can employ the spin

Hamiltonian approach to interpret the observed negative shift of the inelastic step.

5.4.2 Ho-Ho dimers

Unlike Co-Co and Ho-Co dimers, the inelastic step in the dI/dV spectra observed for the Ho-Ho dimers does not shift or spilt as a function of the external out-of-plane B field (Figure 5.7 a and b). This indicates either a non-magnetic origin behind this inelastic transition, or a strong in-plane magnetic anisotropy in these dimers. Unveiling this will require further experimental evidences and this is beyond the scope of the present work.

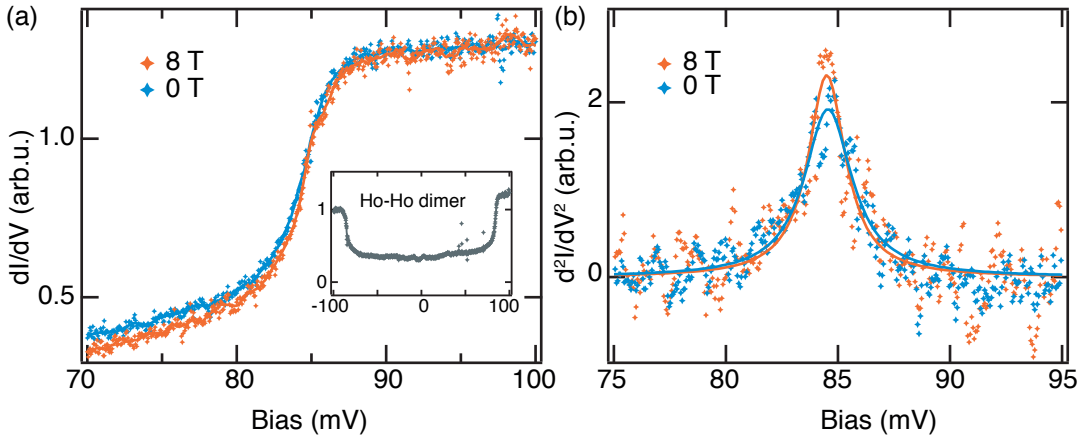

Figure 5.7: Zoom of the magnetic field dependent (a) dI/dV and (b) d^2I/dV^2 spectra of Ho-Ho dimer. Inset of (a) shows the full range dI/dV spectra. V_t = 120 meV, I_t = 1 nA, V_{mod} = 200 μV peak-to-peak, and T = 0.4 K.

Chapter summary

- Ho-Co dimers adsorbed on MgO/Ag(100) substrate exhibit spin-excitations at ±20 meV and ±8 meV. The former is a $\Delta J = -1$ transition while the latter stems from a $\Delta J = 0$ transition.
- According to our simple and yet interpretative spin Hamiltonian model, the most intense spin-excitation occuring at ±20 meV corresponds to a large (55%) change in Co spin moment.
- The spin-excitation at ±8 meV is very weak in intensity and is only detected with the help of a SP-tip. According to the spin Hamiltonian model, this corresponds to an overall canting of the heterodimer's magnetization.
- Co-Co dimers exhibit spin-excitation on the same surface at ±13 meV. However, the inelastic steps evolve towards lower energy with increasing magnetic field.
- There is a large inelastic transition at aournd ±85 meV in Ho-Ho dimers, the origin behind which is yet unknown.

6 Surface-supported single atom and single molecule magnets

In the previous chapters, I have elaborated the results on RE single atoms and small clusters adsorbed on various metal substrates as well as thin insulating substrate of MgO, as measured by STM and XMCD, and calculated using mean-field nucleation theory and multiplet analysis within point charge approximation. In this chapter, I will focus on four additional projects involving the measurements on surface-supported single atoms and single molecule magnets (SMM) which are listed below:

- Magnetic remanence in single Ho atoms on MgO/Ag(100) [41]
- Enhanced magnetic properties of *ex situ*-synthesized $TbPc_2$ SMMs on MgO/Ag(100) [111]
- Superlattice of single atom magnets of Dy on graphene/Ir(111) [80]
- On-surface synthesis of single molecule magnets (manuscripts are in preparation)

The first three projects were aimed at achieving magnetic stability in surface-supported single atoms and single molecules. The magnetic stability has been achieved essentially by adsorbing the magnetic atoms or molecules on substrates which are only weakly interacting and therefore do not perturb the magnetic properties of the adsorbate. The last project was aimed at designing SMMs using on-surface *in situ* metalation, that exhibits identical magnetic properties as known for their *ex situ* synthesized analogues. In this chapter, I will first introduce the scientific quests driving each project and then will briefly highlight the key results in each case.

Work contribution

I had the opportunity to contribute to these four projects as part of a research team, in particular, through the XMCD and x-ray photoemission spectroscopy (XPS) measurements. The XMCD team was led by Dr. Stefano Rusponi for the single atom magnet projects and by

Dr. Jan Dreiser for the $TbPc_2$ SMM project. The XPS measurements were performed under the supervision of Dr. Katharina Diller for on-surface synthesis of SMMs.

6.1 Magnetic remanence in single Ho atoms on MgO/Ag(100)

The beneficial effects of decoupling the magnetic adatoms from the scattering of substrate's conduction electrons, was first experimentally realized in 2007 while studying Mn atoms on Al_2O_3 layers grown on a NiAl surface [116]. The insulating layer allowed to obtain a strong contribution to the observed spin-excitations and provided direct insight into the quantum levels of the Mn adatoms. Following this, atomically thin layers of Al_2O_3 on NiAl and especially Cu_2N on Cu(100) has been widely used in several contemporary works [22, 28, 29, 63, 105, 117, 118]. However the growth of these insulating layers are self-limiting, and therefore the decoupling from the substrate has not been efficient enough. Consequently the magnetic lifetime remained short, *e.g.*, only about 100s of ns time scale in Fe-Cu dimers and even shorter in single atoms [117, 118]. To this end, the use of MgO grown on Ag(100) as an insulating barrier is quite recent. This was first used for investigating the magnetic properties of single Co atoms adsorbed on top. A record large MAE of 58 meV along with a spin-lifetime of $\approx 230\ \mu$s was reported for the Co atoms on this surface [33]. This increases up to 10 ms for Fe atoms on the same surface [32]. Notably these time scales are orders of magnitude larger than previous work on Cu_2N [118].

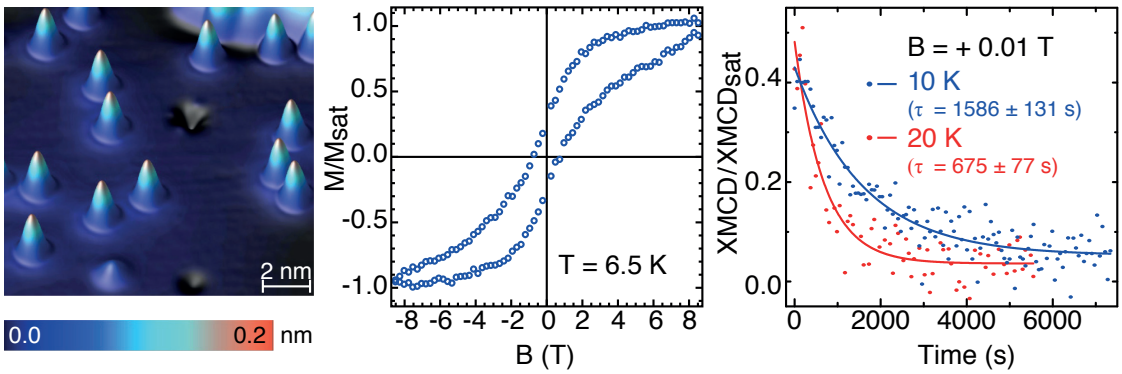

Figure 6.1: Adapted from [41]: (a) STM image of 0.005 ± 0.001 ML of Ho atoms adsorbed on 2 ML thick MgO/Ag(100). $V_t = 100$ mV, $I_t = 20$ pA. $T = 4.7$ K. (b) The $M(B)$ curves measured for a sample with 0.01 ML Ho atoms adsorbed on 7 ML MgO, in normal incidence, showing open hysteresis and a remanent magnetization of almost 25% of the saturation level. Employed field sweep rate = 8 mT/s, x-ray flux $\phi = 1 \times 10^{-2}$ photons nm^{-2}s^{-1}. (c) Measurement of magnetic lifetime from the time evolution of XMCD-maximum normalized to the saturation value at 6.8 T. Dots: measurements, solid lines: exponential fits to extract the magnetic lifetime τ. Ho coverage = 0.015 ML, MgO thickness = 6 ML, $\phi = 0.14 \times 10^{-2}$ photons nm^{-2}s^{-1}.

In this work we have achieved even longer magnetic lifetime from single Ho atoms adsorbed on MgO/Ag(100). Figure 6.1 a is a LT-STM image of a typical sample, highlighting the presence of the Ho atoms as single isolated protrusions on MgO layer. The magnetization curves

recorded in normal incidence exhibit hysteresis opening up to 8.5 T, with a coercive field of 1 T (Figure 6.1 b). The Ho atoms can preserve stable magnetization with exceptionally long lifetime of ≈ 1500 s at 10 K, albeit this reduces to a certain degree at 20 K as thermally induced relaxation mechanism sets in (Figure 6.1 c). As these measurements are perturbed by the energetic secondary electrons produced by the high energy x-ray photons, extrapolation to zero-photon limit suggests a lifetime of about 1 hour at 2.5 K [a]. Most importantly, the magnetic hysteresis and remanence, the properties which are considered as the most evident footprints of magnetic stability, have been recorded for this system up to 30 K [41].

The unprecedented magnetization lifetime and the observation of magnetic stability up to a considerably elevated temperature in the Ho atoms, firstly stem from the specific magnetic level distribution achieved in presence of the C_{4v} symmetry of MgO. This prevents magnetization reversal *via* quantum tunneling and first-order electron scattering at any field. Moreover the stiff and insulating MgO layers efficiently quench any probable higher order processes by decoupling the Ho-moment from the conduction electrons and the soft phonons of the underlying metal substrate, which by no means could be suppressed by the symmetry alone [41].

Notably there are some discrepancies between the results independently obtained using XMCD and STM for the Ho atoms adsorbed on MgO/Ag(100). For instance, in order to observe a clear opening of hysteresis we require thicker MgO layers (≥ 2.4 ML) as compared to the ones used for the STM measurements. Moreover, from the measured total magnetic moment in XMCD we infer $\langle J_z \rangle = 4.66$ in the ground state which is significantly low compared to the value of 8 inferred from STM measurements [109]. These discrepancies might arise from the very different detection mechanisms employed in these two techniques. The x-ray photons used during the XMCD measurements produce energetic secondary electrons, which continue to perturb the spin distribution of the Ho ensemble. This makes the detection of the loop opening very sensitive to the employed photon flux. This has been elaborated in detail in ref. [41, 111]. As the secondary electrons are mostly generated from the Ag(100) substrate, those can easily scatter off the Ho atoms across a thinner MgO barrier. This effect can be surpassed in presence of thicker MgO layer which makes the Ho moments less sensitive to the perturbation from the secondary electrons, finally leading to observation of a clear opening of hysteresis.

Moreover the perturbative effect of the secondary electrons can influence the measurement of the total magnetic moment in XMCD. In presence of the secondary electrons the equilibrium between spin-up and -down population is shifted from the thermal equilibrium. Since the Ho atoms possess a long magnetic lifetime at 6.8 T they can not "thermalize" within the timescale of measurement of the XAS and XMCD spectra at this field. Consequently the expectation value of the total magnetic moment, which is deduced from such spectra, is effectively reduced leading to a lower estimate of $\langle J_z \rangle$.

[a] The extrapolation is done based on the data obtained at varying photon flux at 2.5 K (for detail see ref. [41] and the supplementary information therein).

On the contrary, STM measurements are not intrinsically affected by such high energy electrons, thereby can represent a more reliable estimates of the magnetic moment and the J_z in the ground state. However, in this particular case, one can also question the magnetic moment obtained using STM since magnetic remanence from a system with $\langle J_z \rangle = 8$ is unexpected in presence of the four-fold C_{4v} symmetry of the underlying MgO surface due to QTM. Despite these open questions, the unprecedented magnetic stability in the Ho atoms at finite magnetic fields is unambiguously proved by both of these independent techniques. Inputs from further extended measurements will help to elucidate the true electronic structure and magnetic level distribution of the Ho atoms on MgO/Ag(100).

6.2 Enhanced magnetic properties of *ex situ*-synthesized $TbPc_2$ SMMs on MgO/Ag(100)

$TbPc_2$ is the most studied SMMs in the whole series of lanthanide-Pc_2 systems. In this SMM the Tb^{3+} ion is the magnetic center which is sandwiched between two phthalocyanine (Pc) macrocycles. An out-of-plane magnetization of the Tb^{3+} ion with a very large MAE barrier (65 meV) for magnetization reversal characterizes the key magnetic properties in this SMM [119]. Despite this large MAE barrier, only vanishingly small magnetic hysteresis and remanence has been reported for adsorption on non-magnetic metal substrates [120–123].

To this end, we have used the same strategy of employing thin insulating layers of MgO grown on Ag(100) as a substrate for hosting sub-ML coverage of this SMM. STM images evidence regular arrangement of these molecules with a periodicity of 1.45 nm [111]. Using XMCD

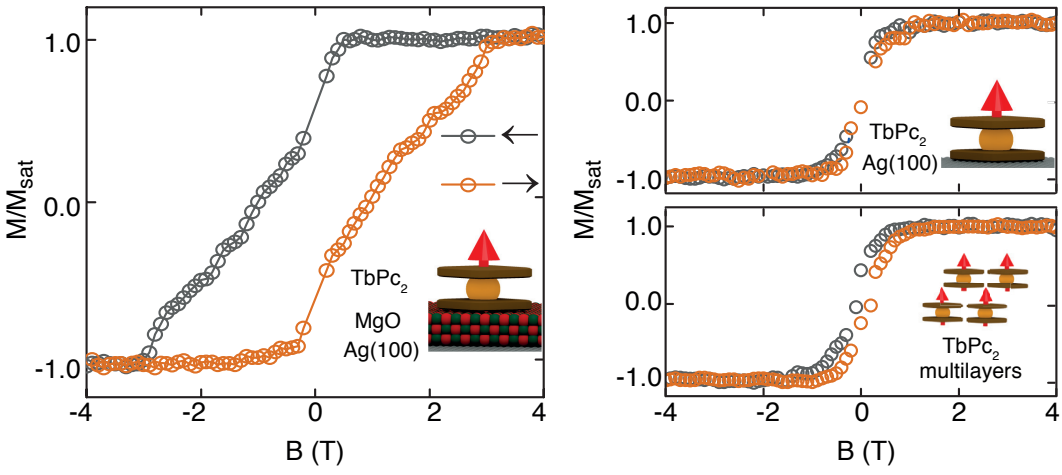

Figure 6.2: Adapted from [111]: Magnetic hysteresis loops measured in normal incidence for $TbPc_2$ molecules adsorbed (a) on 5 ML MgO, molecular coverage $\Theta = 0.6$ ML, (b) directly on Ag(100) with $\Theta = 0.3$ ML (one ML refers to the coverage for which the entire surface is covered by the molecules.), and (c) in multilayers ($\Theta = 3$ ML) on MgO. Field sweep rate = 33 mT/s, $T = 3$ K, and x-ray flux $\phi = 0.085 \times 10^{-2}$ photons $nm^{-2}s^{-1}$.

measurements we have shown that the magnetic remanence and the opening of hysteresis of this SMM can be significantly improved compared to direct adsorption onto a metal substrate. This can be readily deduced from the severely reduced opening presented in Figure 6.2 b. It is only in the case of adsorption on MgO/Ag(100) when a record large magnetic remanence and hysteresis have been achieved (Figure 6.2 a). For sub-ML molecular coverages on MgO, we have recorded long magnetic lifetime of τ = 14 min at 3 K and 0.5 T [111]. Increasing the molecular coverage from sub-ML to multilayers on MgO eventually reduces the opening, possibly due to the vertical interactions among the Tb^{3+} centers in each SMM in this geometry (Figure 6.2 c).

Similar to the case of the Ho atoms, the outperformance of $TbPc_2$ on this substrate arises from the insulating properties of MgO which efficiently filter out all relaxation mechanisms to the first-order (electron and phonon scatterings). Those are otherwise present when directly adsorbed on the metal substrate. Moreover, the presence of MgO significantly suppresses the direct hybridization with the underlying metal substrate, which further helps to preserve the ideal electronic configurations of both Pc ligands and to protect the perfect D_{4d} symmetry of the $TbPc_2$ molecule. On the contrary, direct adsorption onto a metal substrate might cause symmetry breaking of the Tb ligand fields, thereby causing mixing of terms in the corresponding spin Hamiltonian which can promote quantum tunneling of magnetization [9].

6.3 Superlattice of single atom magnets of Dy on graphene/Ir(111)

The ability to achieve magnetic stability down to the scale of single atoms indeed brings promises for their future applications in magnetic data storage. Recent measurements by Natterer *et al.* have even proved that the magnetic states of the individual Ho-atom-magnets can be manipulated (read and write) using LT-STM [109]. However, the realization of regularly arranged single atom magnets poses a severe constraint towards the ultimate feat of magnetic memory with single atom bits.

To this end, we have shown that Dy atoms adsorbed on graphene grown on Ir(111) can self-assemble in a regular hexagonal superlattice (Figure 6.3 a) with a periodicity of 2.5 nm. The periodic moiré pattern formed by graphene grown on lattice mismatched Ir(111) works as a template for such regular arrangement of the Dy adatoms. Most importantly, our XMCD measurements evidence that the Dy atoms exhibit magnetic remanence (Figure 6.3 b) and stability with a magnetic lifetime of τ = 1000 s at 0.01 T and 2.5 K [80].

The magnetic stability in the Dy adatoms stems from the convenient combination of a degenerate ground state doublet with $J_z = \pm 7$ and the C_{6v} symmetry provided by the graphene CF. Moreover, graphene being the stiffest material, it can efficiently suppress spin-phonon coupling. Besides these, for graphene grown on Ir(111), very low electron density is expected at the Fermi level [124] which reduces the scattering from the Ir(111) conduction electrons.

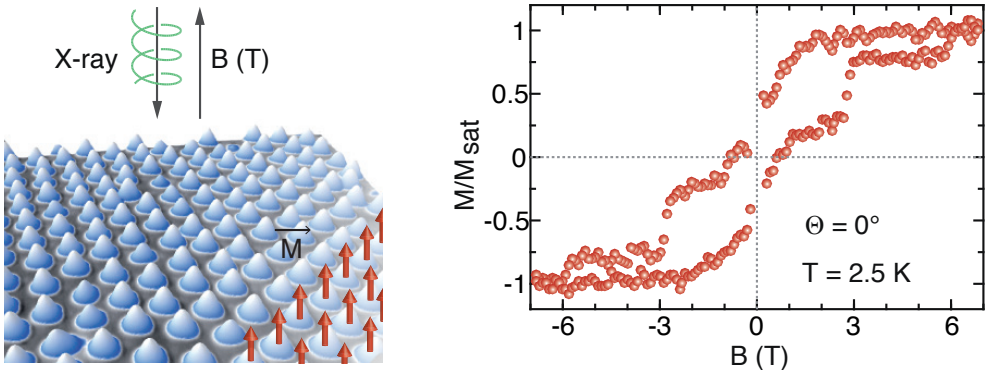

Figure 6.3: Adapted from [80]: (a) STM image showing periodic arrangement of Dy single atoms on graphene on Ir(111). Deposition temperature = 40 K and measurement temperature = 5 K. $V_t = -0.2$ V and $I_t = 100$ pA. (b) Magnetization curve measured in normal incidence for the Dy superlattice. Field sweep rate = 33 mT/s and x-ray flux $\phi = 1.5 \times 10^{-2}$ photons nm^{-2}s^{-1}.

6.4 On-surface synthesis of single molecule magnets

On-surface metalation of tetrapyrrole molecules is a profoundly studied field of research that focuses on *in situ* creation of molecules with varied chemical and electronic properties. In this technique, a metal atom is incorporated into the free base molecule(s) (hence the term metalation). The most widely used approach to achieve a controlled metalation, is the co-evaporation of the reaction ingredients onto a surface where the metalation reaction takes place. An excellent overview on this topic can be found in ref. [125]. The on-surface synthesis has a major advantage over the *ex situ* synthesized molecules. The latter needs to be thermally evaporated for adsorbing them on a desired surface. Often depending upon the evaporation conditions and the delicacy of the molecule, one ends up with certain fractions of unwanted broken species without any metal center. This has been reported for several lanthanide double deckers such as $TbPc_2$, $DyPc_2$, YPc_2, and $NdPc_2$ [126, 127]. On the contrary, an *in situ* synthesized sample can surpass this problem as the reaction precursors are added individually on the substrate and are subsequently allowed to react to produce the desired metal-organic complex.

We have employed this technique to create $TbPc_2$ SMMs on Ag(111) using 2HPc as the free base molecules. The well characterized $TbPc_2$ SMM serves as the benchmark. A successful *in situ* preparation of this can be considered as the starting point for designing novel magnetic molecules on surface which are otherwise difficult to prepare. We have proved using XPS measurements that the metalation reaction takes place already at room temperature (data not shown). Note that this is markedly different than what is known for the cerium tetraphenylporphyrin double deckers ($Ce(TPP)_2$) where annealing at 500 K was used by Écija *et al.* [128]. Moreover, our experiments evidence that the SMMs thus produced possess an x-ray absorption (XA) lineshape with the typical triple-peak feature (Figure 6.4 a, upper pairs of spectra in red and black) and an out-of-plane easy axis with an extent of angular dependence in the XMCD (Figure 6.4 a, middle spectra in purple and blue), which are identical to the *ex situ*

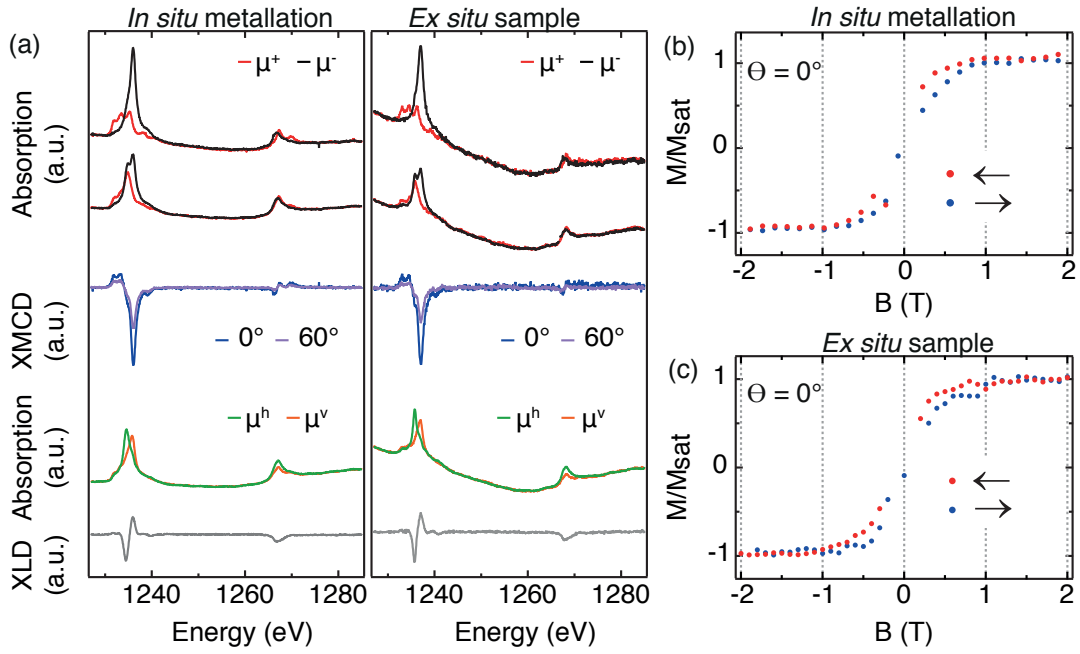

Figure 6.4: Comparison between *in situ* synthesized and pre-synthesized $TbPc_2$ molecules following the characteristic Tb $M_{4,5}$ edge XAS, XMCD, XLD signatures in (a) and the magnetization curves in (b) and (c). The in situ synthesis was performed by depositing 2 ML 2HPc on Ag(111) and by adding 0.3 ML Tb onto it. The presynthesized molecules are measured on Ag(100) with a sub-ML coverage of the $TbPc_2$. $B = 6.8$ T for XMCD and 0.1 T for XLD. Field sweep rate in (b) and (c) is 33 mT/s. $T = 3$ K for all measurements.

synthesized $TbPc_2$ molecules adsorbed on Ag(100) [111]. As observed for the pre-synthesized case, the *in situ* prepared $TbPc_2$ molecules also exhibit flat lying geometry as it becomes evident from the x-ray linear dichroism (XLD) signal (Figure 6.4 a, lower spectra in gray). Most importantly the $M(B)$ curves indicate a small hysteresis opening proving the finite magnetic lifetime of these molecules, as also observed in the pre-synthesized $TbPc_2$ (Figure 6.4 b and c).

Altogether these results confirm the feasibility of on-surface creation of lanthanide based SMMs. With this hindsight the fabrication of more exotic magnetic molecules on different types of substrates can be anticipated in the future.

Chapter summary

- Ho atoms on MgO/Ag(100) and Dy atoms on graphene/Ir(111) are the first evidence of surface-supported, stable single atom magnets.
- The insulating properties of MgO/Ag(100) significantly enhance the hysteresis opening in $TbPc_2$ SMM.
- *In situ* metalation is proved to be a feasible approach for designing SMMs on surface.

7 Conclusions and perspective

This thesis illustrates the experimental results and presents the insightful theoretical models for understanding the magnetic properties of surface-supported magnetic atoms, molecules, and atomic scale clusters of REs. In the following we will highlight the advances made in each projects together with the conclusive remarks.

Adatom-substrate interaction

Tailoring the magnetic properties in surface-supported REs demands optimum control on their magnetic level distribution. The adatom-substrate interaction is one of the most crucial factors which determines this. In the first part of Chapter 3, we have shown using XAS, XMCD, LT-STM, and multiplet calculations that individual Ho atoms adsorbed on Pt(111) exhibit a magnetic ground state with $\langle J_z \rangle = \pm 6$, in contrast to previously reported value of ± 8 [37]. Due to the three-fold symmetry at the adsorption site, this ground state is inconsistent with long magnetic lifetime in the Ho atoms.

In the second part of Chapter 3 we have have demonstrated that RE single atoms can possess both trivalent $4f^{n-1}$ and divalent $4f^n$ states when adsorbed on metal substrates, the occurrence of any of the two configurations being solely determined by the specific adatom-substrate interaction. In particular, the trivalent state is achieved in presence of (a) larger $4f-5d$ promotion energy of the RE and (b) the strong hybridization with the surrounding environment. For the specific case of Er adatoms, we have also shown using multiplet calculation that the adatom-substrate interaction is significantly stronger in case of Ag(100) compared to the one of Ag(111), and therefore, Er stays trivalent on Ag(100) while it shows divalent configuration on Ag(111).

None of the REs used in this work exhibit magnetic hysteresis on the metal substrates. This absence of magnetic stability possibly arises from the destabilization caused by the conduction electrons and soft phonons of the underlying substrates.

Nevertheless, from this systematic study of adatom-substrate interaction, one can deduce

that depending upon the spatial symmetry and electronic properties of the surrounding environment and the degree of hybridization with the substrate, the $4f$ occupancy, and therefore J, can differ from the free atom value. In addition, we have identified that it is the adatom-substrate interaction which determines whether the ground state will possess the maximum, minimum or intermediate value of J_z [40].

Adatom-adatom interaction

Adatom-adatom interaction becomes crucial in atomic-scale clusters. In Chapter 4, we have demonstrated how adatom-adatom interaction can be used for controlling certain magnetic properties, *e.g.*, the orientation of the magnetic easy axis, anisotropy, and emergence of hysteresis, in atomic scale clusters of Er. In the process of optimizing the electrostatic interaction with the delocalized $4s$ electrons of the underlying substrate, the Er adatoms exhibit a very strong in-plane magnetization on Cu(111) [40]. With the help of XMCD, LT-STM, MNFT, and multiplet analysis, we have demonstrated that, for Er clusters starting from the size of three atoms, the adatom-adatom interaction dominates over the adatom-substrate interaction. This leads to the observed large out-of-plane magnetic anisotropy in Er clusters (2.9 meV/atom). Interestingly all clusters starting from trimers also exhibit magnetic hysteresis. The measured lower bound of the magnetic lifeime is $\approx$ 2 min at 2.5 K and 0.1 T. However, these clusters exhibit quantum tunneling of the magnetization (QTM) [9, 11], as it becomes evident from the butterfly shapes and the absence of magnetic remanence in the hysteresis at low coverages. Only upon reaching a significant fraction of larger sizes, at $\Theta > 0.06$ ML, the feature disappears and remanence is observed.

The evidence of magnetic hysteresis reflects the presence of ferromagnetic exchange interaction within an Er cluster which creates macrospins with large total spin and MAE. This large total spin is intrinsically less sensitive to quantum fluctuations and scattering from the conduction electrons [21], leading to the observed magnetic stability in all clusters starting from the trimers, albeit being directly adsorbed on a metal substrate. This is an alternative approach to the use of symmetry-protected ground states combined with ultra thin insulating layers for stabilizing the spin of a quantum magnet, as we have recently demonstrated for individual Ho atoms on MgO (see section 6.1) [41].

Adatom-adatom interaction in RE-TM heterodimers

In order to further enrich our understanding of magnetism in surface-supported REs, we extended the investigation of adatom-adatom interaction for a RE-TM heterodimer system, *i.e.*, the Ho-Co heterodimers adsorbed on MgO/Ag(100) (Chapter 5). The thin insulating layer of MgO serves as a better alternative to the use of metals, as the former can efficiently protect the magnetic entity from the scattering with conduction electrons and soft phonons (see Chapter 6 and refs. [41, 111]). In presence of these beneficial effects of the insulating MgO substrate, the ferromagnetic coupling among the two atoms in the Ho-Co heterodimers

leads to the experimental evidence of spin-excitation at around ±20 meV. With the help of an effective spin Hamiltonian model, we have determined that the observed excitation stems from a $\Delta J = -1$ transition. During this transition, large part ($\approx 50\%$) of the Co moment is reduced while the Ho moment changes only by $\approx 3\%$. This suggests that the observed spin-excitation is somewhat correlated to the exchange coupling between Ho and Co atom. In addition, with the help of a SP-tip, we have detected another pairs of transition at ±8 meV. According to our effective spin Hamiltonian model this corresponds to $\Delta J = 0$ transition, *i.e.*, the spin-excitation occurring between the two sub levels within the ground state multiplet. This excitation occurs when both Ho and Co moments are reduced by similar amount, resulting in an overall canted magnetic moment of the heterodimer.

As the first evidence of spin-excitations in RE-TM heterodimers, this work demonstrates the potential of locally probing a $4f$ element as an integral part of an exchange coupled system. In addition, the peculiar properties detected in these heterodimers such as, the significantly large g factor of 3 and the ferromagnetic exchange interaction between Ho and Co instead of the ferrimagnetic exchange coupling known for their bulk analogues [115], hint towards an unusual mechanism driving their magnetic behaviours. Further investigations on other RE-TM heterodimers will significantly add to these knowledge and will allow us to elucidate this aspect further.

Stability in single atom and single molecule magnets

In Chapeter 6 we have briefly touched upon our recent discoveries of magnetic stability in Ho and Dy single atom magnets and of significantly enhanced magnetic lifetime in $TbPc_2$ SMM. It is intriguing to note that the magnetic lifetime of Dy on graphene/Ir(111) at 0.01 T and the one of $TbPc_2$ on MgO/Ag(100) at 0.5 T are comparable. Together with the discovery of the Ho-atom-magnets this demonstrates that single-atom-bit with largely better or at least comparable magnetic stability is feasible. Moreover, the array of the Dy-atom-magnets readily offers a very high bit density of 110 Tbit/in^2. This number simply demonstrates the scalability of single-atom-bits, exactly as the idea was once conceived six decades back by R. P. Feynman [129]. However, if compared with $TbPc_2$, the same competence in terms of the bit density is yet to be achieved in single-atom-magnets [a]. This leaves room for prospective research for discovering the ultimate bit density that can be achieved from single atoms.

As a final remark, the long spin relaxation time T_1 reported throughout this work for different systems is one of the most salient features of a stable quantum magnet. Together with this and specially in the context of quantum computation, there is another crucial relaxation term known as the phase coherence time T_2. This term determines the coherence time of a quantum superposition of states. As T_2 is intrinsically bounded by T_1 ($T_2 \leq 2T_1$), systems

[a] 110 Tbits/in^2 for Dy-atom-magnets *vs* 310 Tbits/in^2 for $TbPc_2$ SMM on MgO/Ag(100); the bit densities are calculated from the periodicity in the respective arrays as measured with the LT-STM.

with long T_1 provide promising routes to achieve prolonged T_2 time. Recently T_2 time has been measured for individual Fe atoms adsorbed on MgO/Ag(100) using single-atom EPR measurements with STM [130]. SMMs containing one RE ion as the magnetic core ($TbPc_2$, Yb-trensal), have also been investigated for the same [131–133]. Measurements of the T_2 times for single RE adatoms have not been reported so far. The discovery of magnetic stability down to single RE atoms opens a new avenue in this direction.

Appendix

A Multiplet calculations: Er clusters on Cu(111)

Multiplet analysis was performed to qualitatively reproduce the experimentally observed trend in XMCD as a function of Er coverage. This shows that indeed the presence of peripheral ligands plays an important role in the observed change in the magnetic easy axis (Figures A.1, A.2), thus quantitatively supporting the perceived role of the ligand charges depicted in Figure 4.1 as yellow and green speckles.

The magnetic ground state of an Er cluster is determined by the interplay of two interactions, (a) the electrostatic interaction of the $4f$ shell with the surrounding ligands (Cu as well as Er) and, (b) the exchange coupling between the $4f$ electrons via the external $6s$ and $5d$ electrons of Er. Although, the latter plays an important role and is known to induce complex magnetic phases in the late lanthanide single crystals [134], investigating this aspect is extremely demanding and far beyond the scope of this work. Therefore, we limited our analysis by involving only the interaction of an Er atom with the surrounding ligand charges. To verify the role of the ligand fields in governing the easy axis of magnetization for different clusters, we have performed atomic multiplet simulation with a point charge approach for the crystal field (CF) description using multiX software [60]. Our simulations provide a direct access to the energy levels of the ground state and first excited state multiplets. All simulations were performed for $T = 2.5$ K, with a number of holes $n_h = 3$, and by replacing the ligands as effective point charges in the middle of the two interacting atoms. The values of the spin-orbit coupling and coulomb interactions for Er were scaled to 97% and 85% of the Hartree-Fock values, respectively. The experimental line broadening due to the finite lifetime of the core-hole state was modeled by convolution with a Gaussian of $\sigma = 0.3$ eV.

In the low coverage limit most of the population is in the form of monomers and their spectrum can be simulated by modeling a single Er atom in an effective CF given by the ligand charges of the underlying Cu(111) substrate. We compared this simulation with the spectra measured at 0.015 ML where $Q_1 \geq 97\%$. A very good agreement between the measured and calculated spectra of the single atoms (Figure A.1 a) is obtained by applying least-squares fits to optimize z position and the charge of the effective Cu ligands (Table A.1). After applying sum rules on the simulated spectra we have obtained $\langle M_{tot} \rangle = 1.6\ \mu_B$ for $\theta = 0°$ and $8.1\ \mu_B$ for $\theta = 55°$, in

good agreement with our experimental measurements (Table 4.2).

Table A.1: Crystal field used for the multiplet simulations of an Er monomer. The x, y coordinates were chosen following the lattice parameters of bulk Cu(111).

Cu @ z = −1.3 Å		
x (Å)	y (Å)	Charge e
0.72	0.00	−0.07
−0.36	0.63	−0.07
−0.36	−0.63	−0.07

At the very high coverage, where cluster abundance is 100%, it is reasonable to assume that the Er atoms coordinate in a closed packed arrangement. Thus, each Er atom sees the ligands of the neighboring ones in the xy plane as equatorially placed charges around. The corresponding spectra of an ensemble of fully coordinated atoms, can therefore be simulated by placing an Er atom within the CF provided by 6 equispaced equatorial ligands. In order to investigate the effects of such equatorial ligands, we have first simulated a series of spectra by varying the Er ligand charge in between −0.05 e and −0.15 e while keeping the position and strengths of the underlying Cu ligands fixed as optimized for the single atom case (Table A.2). Figure A.1 b shows a gradual increase (decrease) of the XMCD signal in $\theta = 0°$ (55°) with increasing Er ligand charge. After applying sum rules on such spectra we obtain $\langle M_{\text{tot}} \rangle$ for the two angles of incidence from which we calculate R which is expressed as in the following equation:

$$R = \frac{\langle M_{\text{tot}} \rangle @ 0°}{\langle M_{\text{tot}} \rangle @ 55°} \tag{A.1}$$

Table A.2: Crystal field used for the multiplet simulations of a fully coordinated Er atom at the high coverage regime. The x, y coordinates were chosen based on the lattice parameters of bulk Er (355 pm) and Cu(111) (255 pm). The equatorial ligand charges were varied between −0.05 e and −0.15 e while Cu ligand charge was fixed at −0.07 e for simulations shown in Figure A.1 b. For the simulations shown in Figure A.2 b, best agreement was found with −0.4 e of Er and −0.3 e of Cu ligand charges.

Cu @ z = −1.3 Å		Er ligand charge @ z = 0 Å	
x (Å)	y (Å)	x (Å)	y (Å)
0.72	0.00	0.00	1.79
−0.36	0.63	0.00	−1.79
−0.36	−0.63	1.56	0.89
		1.56	−0.89
		−1.56	0.89
		−1.56	−0.89

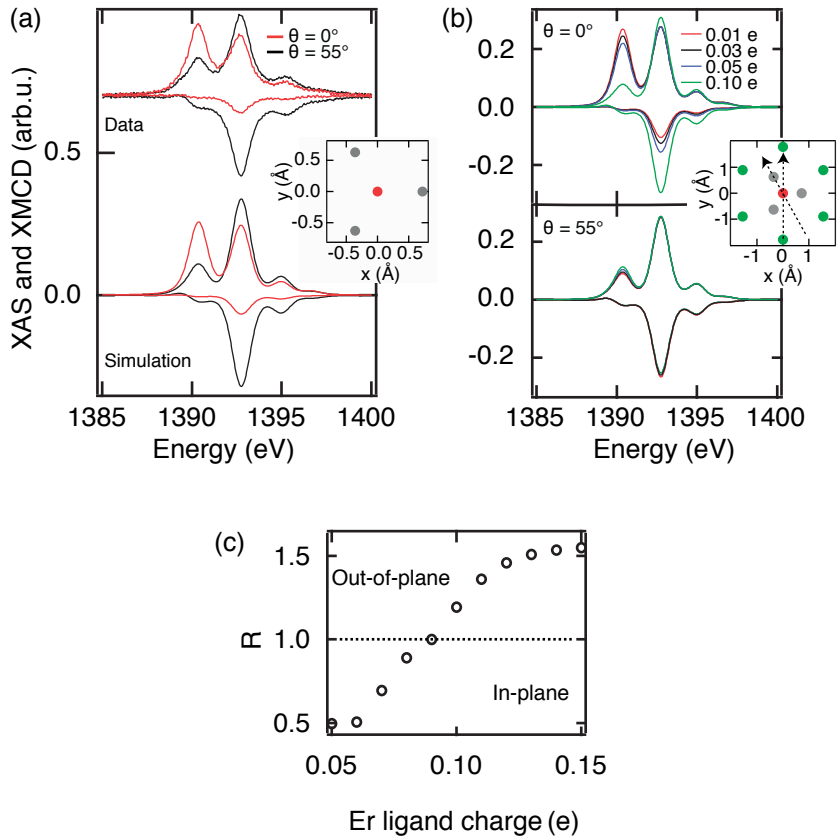

Figure A.1: Multiplet calculations for an Er atom (a) in presence of only Cu ligands, and (b) with 6 additional Er ligands of varying strengths. Experimental data for 0.015 ML are also presented for comparison in (a) and are offset for clarity. In all cases the simulated spectra corresponds to the Er atom at the origin. Insets show the schematics of the crystal field; Er atoms: red, Cu ligand charge: grey, Er ligand charge: green. Arrows show the non equivalent orientations of the probing beam with respect to a given crystal field. (c) Ratio of the total moments obtained from the two angles of incident as a function of Er ligand charge.

Thus $R > 1$ indicates that the easy axis is oriented out-of-plane. For the given set of CF parameters, this happens when the Er ligand charge exceeds -0.09 e (Figure A.1 c). The trend of R versus Er ligand charge directly proves the importance of the equatorial ligands in changing the orientation of the easy axis (Figure 4.1).

Finally, to quantitatively reproduce the spectrum and the magnetic moments at the high coverage limit, we optimized Cu and Er ligand charge in order to fit the measurements at 0.11 ML (Figure A.2). The best agreement using least-squares fits is obtained for -0.3 e of Cu and -0.4 e of Er ligand charges. To reduce the number of free parameters, we fixed the z distance of the Cu ligand charges to the ones optimized for the monomers (-1.3 Å). Note that the need of significantly large value of the Cu charge employed here as compared to the single atom case might be a direct consequence of neglecting other interactions in this simplified model e.g., the interatomic exchange coupling within a cluster, or a different Er-Cu

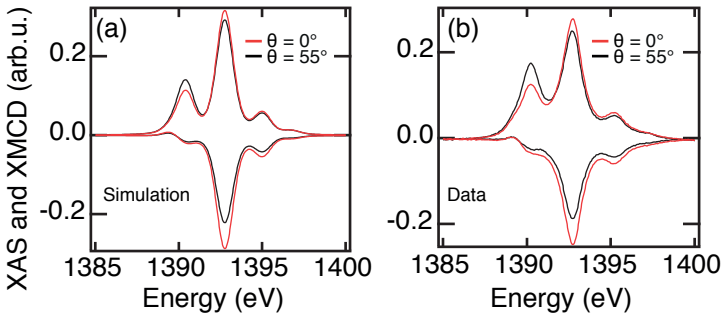

Figure A.2: Multiplet calculation for an Er atom in the high coverage regime with −0.3 *e* of Cu and −0.4 *e* of Er ligand charges. The simulations are shown in (a) while the experimental data are presented for comparison in (b) with 0.11 ML.

distance of the monomer compared to the cluster. Nevertheless, by applying sum rules on these calculated spectra we obtain $\langle M_{\mathrm{tot}} \rangle = 7.5\ \mu_{\mathrm{B}}$ for $\theta = 0°$ and $5.8\ \mu_{\mathrm{B}}$ for $\theta = 55°$, in very good agreement with our experimental results (Table 1). Note that all grazing spectra are obtained by averaging over all possible non equivalent orientations of the probing beam with respect to a given crystal field (shown as black arrows in the inset of Figures A.1 b).

B Mean-field nucleation and growth model

In the following we will describe the three and four population growth models. These equations directly follow from equation 2.12.

B.1 Three population nucleation and growth model

The three population nucleation and growth model relies on the following three rate equations from mean-field nucleation theory described in section 2.2.1:

$$\frac{dn_1}{d\Theta} = 1 - 2\kappa_1 n_1 - \kappa_2 n_2 - \kappa_{\geq 3} n_{\geq 3} - \frac{\sigma \nu_0}{F} \exp\left(\frac{-E}{k_B T_d}\right) n_1 (n_2 + n_{\geq 3}) \tag{B.1}$$

$$\frac{dn_2}{d\Theta} = \kappa_1 n_1 - \kappa_2 n_2 - \frac{\sigma \nu_0}{F} \exp\left(\frac{-E}{k_B T_d}\right) n_1 n_2 \tag{B.2}$$

$$\frac{dn_{\geq 3}}{d\Theta} = \kappa_2 n_2 - 2n_{\geq 3}\left(1 - \frac{dn_1}{d\Theta} - \frac{dn_2}{d\Theta}\right) + \frac{\sigma \nu_0}{F} \exp\left(\frac{-E}{k_B T_d}\right) n_1 n_2 \tag{B.3}$$

These equations express the growth rates of the species containing $1, 2$ and ≥ 3 atoms as a function of coverage Θ. Conventionally these rates are expressed with respect to time. Here we divide them by the deposition flux F. This is allowed if most of the nucleation and growth takes place during deposition, *i.e.*, post deposition processes are negligible. This is a legitimate approximation for our case since we cool down the samples immediately after deposition of Er and this cooling takes much shorter time (≈ 2 min) than the typical time for the deposition (> 5 min). Also note that it is sufficient to cool down by a few kelvin in order to suppress the post deposition processes since the respective rates depend exponentially on temperature.

The densities of the different species are expressed as n_1, n_2 and $n_{\geq 3}$. We have neglected lateral attachment of monomers to each other by thermal diffusion due to the observed strong repulsion amongst them. This assumption is further justified because: (i) we did not observe any dimer formation during the acquisition of STM images even though the single atoms are quite mobile under the STM tip and are only stabilized by the superlattice, (ii) at the lowest coverages, the density of dimers is not affected by the deposition temperature up to 10 K, indicating a large effective monomer-to-monomer attachment barrier. However, dimer formation through direct impingement onto monomers has to be included in order to model the observed dimer abundance. In the following, we show that this mechanism is central for proper modeling of the nucleation and growth of Er clusters.

The impingement cross-sections are defined by the number of sites around a given species where the impinging atoms directly lead to cluster formation or growth. We obtained $\kappa_1 = 7, 19, 37$ and $\kappa_2 = 12, 28, 50$ by counting for the 1^{st}, 2^{nd} and 3^{rd} nearest neighbor (NN) sites respectively. For $N \geq 3$, we computed $\kappa_{\geq 3}$ by considering a geometric approach [56, 57]. The average cluster size of $N \geq 3$ clusters is given by $\langle S_{\geq 3} \rangle = \frac{\Theta - n_1 - 2n_2}{n_{\geq 3}}$. The corresponding radius of the direct impingement zone $r = \sqrt{\frac{2\langle S_{\geq 3} \rangle}{\pi}} + \frac{\alpha\sqrt{3}}{2}$. The factor of 2 in the first term accounts for the ratio of the atomic volumes of Er to Cu while $\frac{\alpha\sqrt{3}}{2}$ accounts for the distance up to the α^{th} NN sites. Finally the impingement cross-section of a cluster of average size $\langle S_{\geq 3} \rangle$ is computed as $\kappa_{\geq 3} = \pi r^2$ (Figure B.1). In Figure B.1 we have assumed that all Er atoms adsorb on similar sites (either all fcc or all hcp). The schematic shows the case of all fcc adsorption. Thus the distance between two Er atoms in the heptamer is $\frac{\sqrt{3}}{2} \times a \approx 441$ pm [a], where $a = 255$ pm, the lattice spacing of the underlying Cu(111) substrate.

As can be seen from Figures B.2 (a-c), none of the direct impingement models, irrespective of the NN distances considered, can reproduce the experimentally observed trends. This deviation is due to the formation of the Er superlattice which is stabilized by the repulsive interactions between the adatoms. This lattice markedly changes the nucleation behavior.

The very low dimer density for $\Theta \leq 0.025$ ML indicates that direct attachment to monomers is ineffective in this coverage regime and that until the completion of the superlattice, the monomers can rearrange themselves in order to accommodate new atoms on the surface. The monomers which are pushed away in this process may either find empty sites or nearby dimers, which, differently from the monomers, are immobile (Figure B.3). Once the complete superlattice is formed, the monomers are locked in their positions and, thus are forced to form dimers if impinged directly. This implies: (i) a coverage-dependent impingement coefficient for monomers that is reduced at low Θ and increases up to a maximum value when the superlattice is formed, (ii) monomers and dimers have a shared impingement coefficient

[a] This is larger than the bulk lattice parameter of Er (355 pm). However note that this lattice spacing is used following geometric considerations, only for estimating the capture area in units of the underlying substrate lattice. For all other purposes (Figure 4.8b, and the inset of Figure A.1b), we have assumed that the atoms within an Er cluster ignore the compact spacing of the Cu(111) substrate (255 pm) and they adapt to their own bulk lattice spacing of 355 pm.

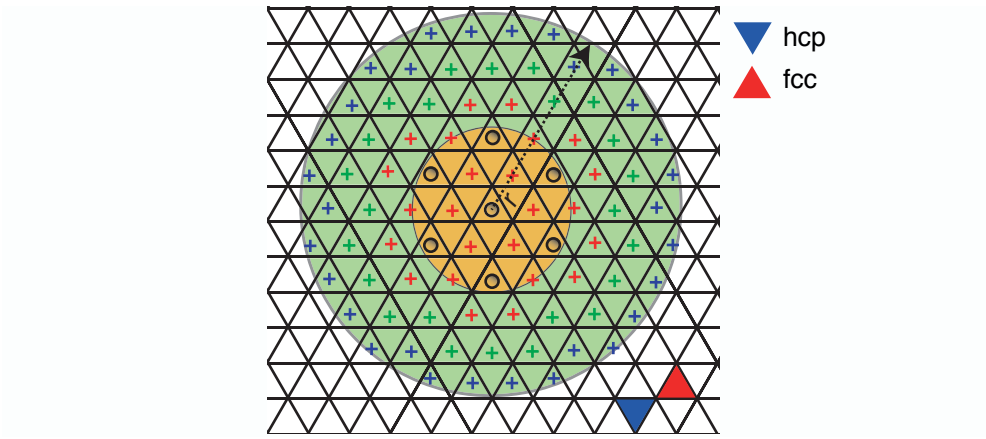

Figure B.1: Schematic showing the effective impingement cross-section (in green) of a heptameter considering up to the 3rd nearest neighbor sites. The substrate is shown as a black grid with periodicity $a = 255$ pm. Red, green and blue crosses define respectively the 1^{st}, 2^{nd}, and 3^{rd} nearest neighbor sites. The small circles indicate the positions of the Er atoms forming the heptamer.

to account for the probability of a monomer to be repelled by another monomer and to be eventually captured by a dimer. We rescaled the value of κ_1 using $G(\Theta) = \frac{1-\exp(-m\Theta)}{1+\exp(-m(\Theta-\frac{\Theta_0}{2}))}$, with Θ_0 being the ideal superlattice coverage, and introduced $\kappa_S \times G(\Theta)$ as the shared attachment area:

$$\begin{cases} \widetilde{\kappa_1} = (\kappa_1 - \kappa_S) \times G(\Theta) \\ \widetilde{\kappa_2} = \kappa_2 + \kappa_S \times G(\Theta) \end{cases} \tag{B.4}$$

These altogether render the coverage-dependent variation in the modified attachment areas $\widetilde{\kappa}_1$ and $\widetilde{\kappa}_2$ respectively within $(0, \kappa_1 - \kappa_S)$ and $(\kappa_2, \kappa_2 + \kappa_S)$. We obtain best agreement with experiment assuming $\kappa_1 = 37$, $\kappa_2 = 50$, which define attachment zones up to the third nearest neighbor sites.

Using $\nu_0 = 10^{12}$ s^{-1} and assuming $\sigma = 7$ for all sizes ≥ 2 atoms [57], we solved Eq. B.1-B.3 for $n_1(\Theta)$, $n_2(\Theta)$, and $n_{\geq 3}(\Theta)$. From them we determine the relative amount of Er present in clusters of size 1, 2, and ≥ 3 as: $Q_1(\Theta) = \frac{n_1(\Theta)}{\Theta}$, $Q_2(\Theta) = \frac{2n_2(\Theta)}{\Theta}$ and $Q_{N\geq 3}(\Theta) = 1 - (Q_1(\Theta) + Q_2(\Theta))$.

Simultaneous fit of the $Q_N(\Theta)$ derived from the STM apparent height histograms at $T_d = 4 \pm 1$ K provide the fitting parameters $m = 200$ ML^{-1}, $\Theta_0 = 0.044$ ML and $\kappa_S = 21$ (solid lines in Figure 4.11 a). $\widetilde{\kappa}_1$ approaches its maximum at the onset of superlattice formation Θ_0 (Figure B.4 a). The coverage Θ_0 is also in fair agreement with our STM measurements and with the ideal coverage of the superlattice (0.035 ML) that can be estimated from the NN Er distance of 1.38 ± 0.05 nm. The effective monomer-to-cluster attachment barrier E becomes important

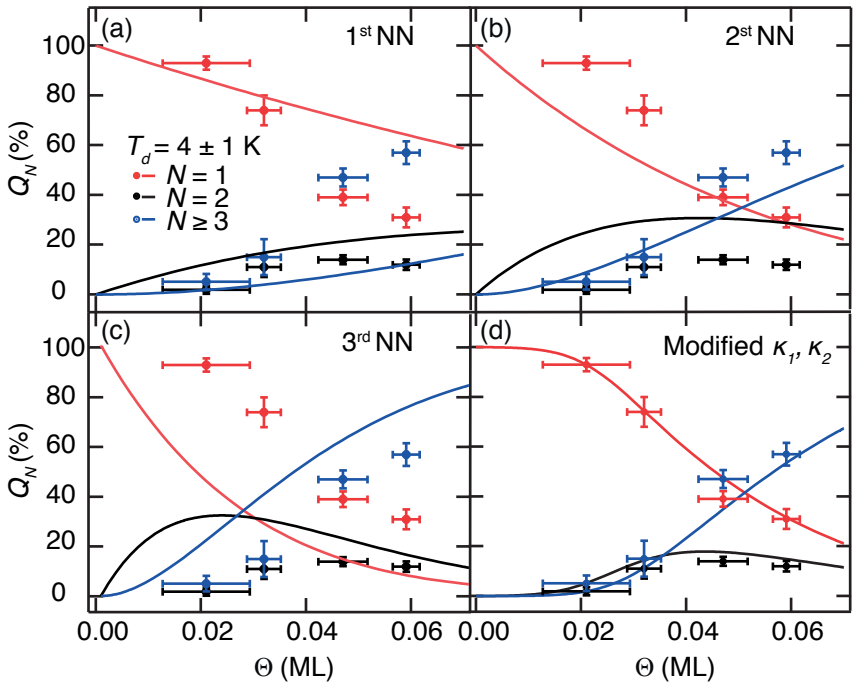

Figure B.2: Relative amount of Er present in the respective cluster sizes obtained from STM (dots) in comparison with simulations considering respectively 1st, 2nd and 3rd nearest neighbor (NN) attachment areas for $N \leq 2$ (a-c) and with their attachment areas modified using Eq. B.4 (d) ($T_d = 4 \pm 1$ K).

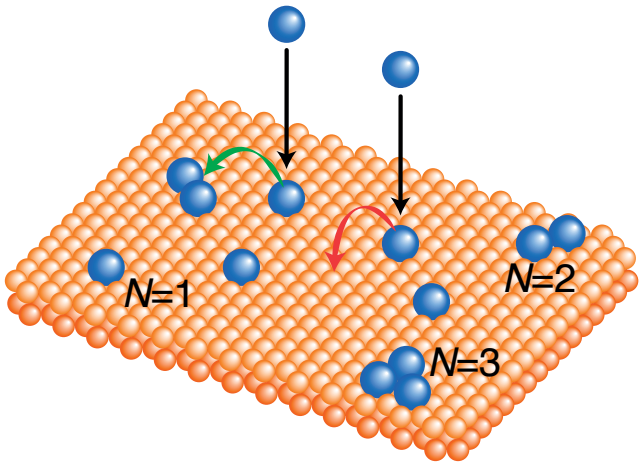

Figure B.3: Schematic illustrating that, due to the inherent dipolar repulsion among monomers, atoms are pushed away on direct impingements either to an empty site (red arrow) or towards a nearby dimer (green arrow).

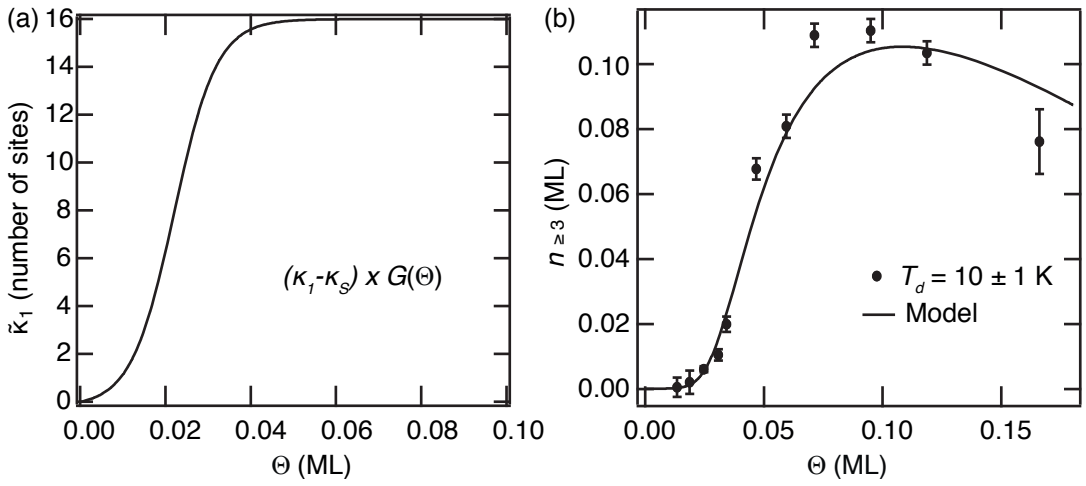

Figure B.4: (a) Coverage dependence of $\widetilde{\kappa}_1$. (b) Density of the trimers and bigger clusters ($n_{\geq 3}$) as a function of coverage.

only for 10 ± 1 K deposition where the available thermal energy helps to exceed adatom-cluster repulsion leading to an enhancement of the cluster growth by lateral attachment. We determined $E = 27 \pm 4$ meV, through the simultaneous fitting of the $Q_N(\Theta)$ obtained from the 10 ± 1 K dataset (solid lines in Figure 4.11 b), keeping the values of m, Θ_0 and κ_S the same as determined before. On the contrary, dimer formation is not affected by increasing the deposition temperature up to 10 K, therefore the adatom-adatom attachment barrier needs to be higher than E.

Finally we counterchecked the validity of this nucleation and growth model by reproducing the experimentally observed trend of the cluster density for $N \geq 3$ (Figure B.4 b). The model correctly follows the experimental measurements and deviates only beyond ≈ 0.10 ML, possibly due to the inherent limitations of mean-field nucleation theory in describing coalescence [93].

B.2 Four population nucleation and growth model

The four population growth model is relevant only to determine whether the presence of Er trimers triggers the onset of magnetic hysteresis. The underlying principle behind the four population model relies on the distinction between trimer and bigger clusters. The rate equations used for this model are:

$$\frac{dn_1}{d\Theta} = 1 - 2\widetilde{\kappa_1} n_1 - \widetilde{\kappa_2} n_2 - \kappa_3 n_{\geq 3} - \kappa_{\geq 4} n_{\geq 4} - \frac{\sigma \nu_0}{F} \exp\left(\frac{-E}{k_B T_d}\right) n_1 (n_2 + n_3 + n_{\geq 4}) \qquad \text{(B.5)}$$

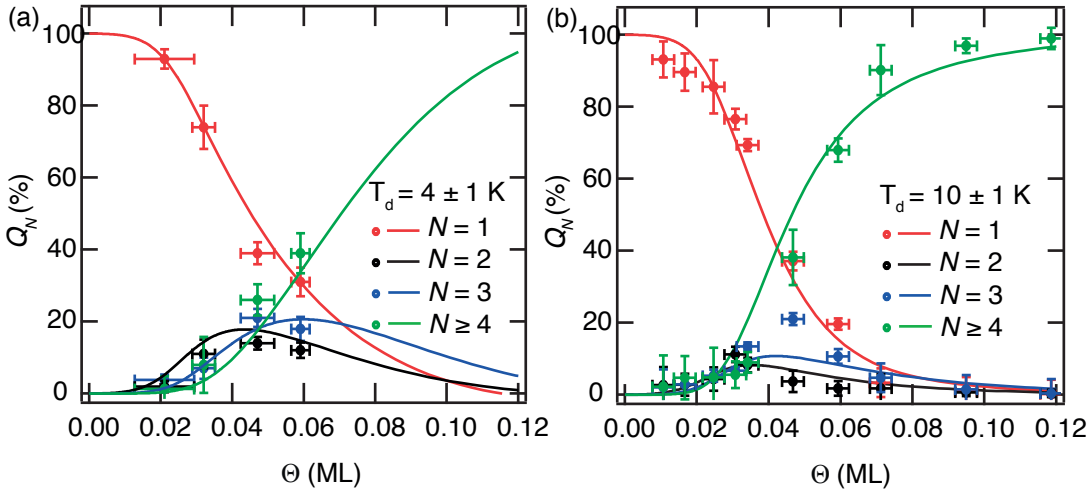

Figure B.5: Coverage dependence of Q_N, the fraction of Er present in N-sized cluster for Er deposition at (a) 4 K and (b) 10 K. Dots: experiments; solid lines: fits from the four population growth model.

$$\frac{dn_2}{d\Theta} = \widetilde{\kappa_1} n_1 - \widetilde{\kappa_2} n_2 - \frac{\sigma \nu_0}{F} \exp\left(\frac{-E}{k_B T_d}\right) n_1 n_2 \tag{B.6}$$

$$\frac{dn_3}{d\Theta} = \widetilde{\kappa_2} n_2 - \kappa_3 n_3 - \frac{\sigma \nu_0}{F} \exp\left(\frac{-E}{k_B T_d}\right) n_1 (n_3 - n_2) \tag{B.7}$$

$$\frac{dn_{\geq 4}}{d\Theta} = \kappa_3 n_3 - 2n_{\geq 4}\left(1 - \frac{dn_1}{d\Theta} - \frac{dn_2}{d\Theta} - \frac{dn_3}{d\Theta}\right) + \frac{\sigma \nu_0}{F} \exp\left(\frac{-E}{k_B T_d}\right) n_1 n_3 \tag{B.8}$$

The attachment areas $\widetilde{\kappa_1}$ and $\widetilde{\kappa_2}$ were calculated using Eq. B.4 and $\kappa_3 = 58$, obtained by counting up to the third nearest neighbor sites. For computing $\kappa_{\geq 4}$, we applied the generic approach based on effective radii calculation as described in the previous section. We used the previously found values of the relevant parameters κ_S, m, Θ_0 and E to reproduce the trends of $Q_N(\Theta)$ as described before (Figure B.5).

The fractions of Er present in the respective cluster size classes, $Q_N(\Theta)$, obtained from this model are in excellent agreement with the experimental observations (Figure B.5). We further employed this model to fit $\langle M_{\text{tot}}(\Theta)\rangle$ (Figure B.6). To avoid overparametrization, we used fixed values of $\langle M_1\rangle$ and $\langle M_2\rangle$, as extracted from the three population model (Table 4.2). We obtain $\langle M_3\rangle = 7.2 \pm 0.2\ \mu_B$/atom, and $\langle M_{\geq 4}\rangle = 7.1 \pm 0.2\ \mu_B$/atom for $\theta = 0°$ and $\langle M_3\rangle = 5.8 \pm 0.2$ μ_B/atom, and $\langle M_{\geq 4}\rangle = 5.3 \pm 0.2\ \mu_B$/atom for $\theta = 55°$. In perfect agreement with the three

population growth model (Table 4.2), this shows out-of-plane magnetic orientation for the trimers and bigger clusters. This again validates our conclusion on the Er trimers being the threshold size starting from which the easy axis turns out-of-plane.

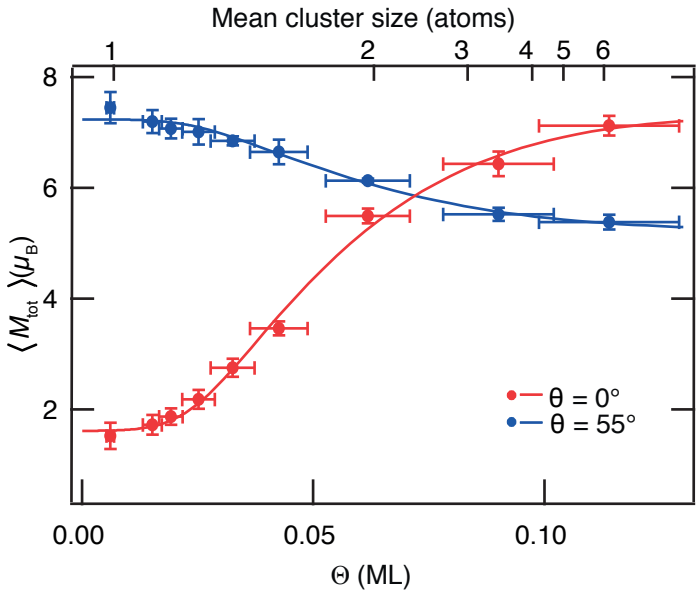

Figure B.6: Coverage-dependent total out-of-plane (0°) and close to in-plane (55°) magnetic moments and fits using four population nucleation and growth model. Dots: experiment; solid lines: fits.

C Spin Hamiltonian approach

C.1 Alternative model for Ho-Co heterodimer

Effects of an in-plane anisotropy term

The positions of both inelastic steps as well as the large effective g factor for the ±20 meV transition can also be reproduced considering a finite in-plane anisotropy of $E(S_{xc}^2 - S_{yc}^2)$ type. The resulting Hamiltonian takes the following form:

$$\hat{H} = D\hat{S}_{zc}^2 + E(S_{xc}^2 - S_{yc}^2) + J_c(\hat{S}_1 \cdot \hat{S}_2) + \mu_B[g_1\hat{S}_{z1} + g_2\hat{S}_{z2}] \cdot \vec{B} \tag{C.1}$$

Here E is the strength of the in-plane anisotropy that promotes mixing of the magnetic levels in $x-y$ plane. The definitions of S_{xc}^2 and S_{yc}^2 follow from equation 2.26. The rest of the terms have the same meaning as in equation 5.1.

Figure C.1 shows the multiplet structures obtained for two different values of E. In both cases we have used the following values of the parameters: $s_1 = 8\ \hbar$, $s_2 = 3/2\ \hbar$, $g_1 = 1.25$, $D = -0.45$ meV, $J_c = -1.25$ meV, and $g_2 = 3$, which are the same as in the simulations presented in Figure 5.5. Table C.1 shows that in both cases we can reproduce the positions of the inelastic steps as well as the large g factor.

Table C.1: Simulated inelastic steps and effective g factor in presence of two different strengths of the in-plane anisotropy term E.

E	Inelastic steps @		Effective g
meV	meV	meV	factor
0.10	20.0	7.9	2.7
0.05	20.0	8.0	2.8

Despite these good agreements, we should note that the strength of the E term significantly

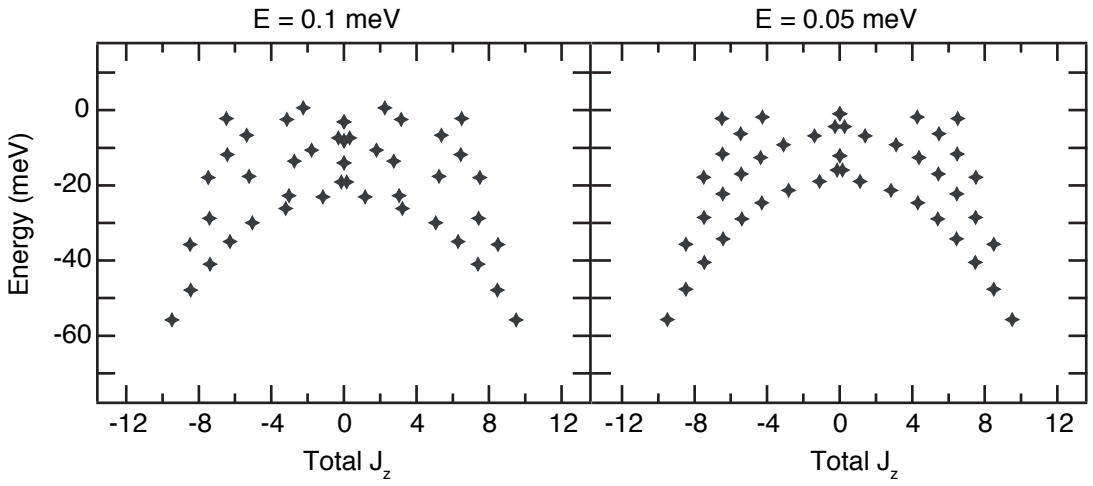

Figure C.1: Simulated magnetic level distributions of the Ho-Co heterodimers in presence of different strengths of the in-plane anisotropy E.

influences the shape of the overall multiplet structure (Figure C.1). In contrast, our SES measurements are only sensitive to the lowest part of the full multiplet (SES transitions are restricted only within $\delta J_z = 0, \pm 1$). Therefore, within the scope of the current work, we can not provide a realistic estimate of the in-plane anisotropy, if any.

Curriculum vitae

Aparajita Singha
✍ EPFL SB IPHYS LNS, Station 3 CH-1015 Lausanne, Switzerland
✉ aparajita.singha@epfl.ch

Scientific career

July 2013 – Present

Doctoral student
École Polytechnique Fédérale de Lausanne (EPFL), Switzerland

On-surface magnetism of rare earth single atoms, molecules, and atomic scale clusters.

November 2011 – May 2013

Research Assistant
University of Copenhagen, Denmark

Experimental biophysics.

July 2010 – July 2011

Research Assistant
Indian Institute of Technology, Bombay, India

Fluorescence microscopy.

List of publications

2016 **Superlattice of Single Atom Magnets on Graphene**
Nano Lett. 16, 7610 (2016). *R. Baltic, M. Pivetta, F. Donati, C. Wäckerlin, A. Singha, J. Dreiser, S. Rusponi, H. Brune.*

2016 **Magnetic Hysteresis in Er trimmers on Cu(111)**
Nano Lett. 16, 3475 (2016). *A. Singha, F. Donati, C. Wäckerlin, R. Baltic, J. Dreiser, M. Pivetta, S. Rusponi, H. Brune.*

2016 **Giant Hysteresis of Single-Molecule Magnets Adsorbed on a Nonmagnetic Insulator**
Adv.Mater. 28, 5195 (2016). *C. Wäckerlin, F. Donati, A. Singha, R. Baltic, S. Rusponi, K. Diller, F. Patthey, M. Pivetta et. al.*

2016 **Magnetic remanence in single atoms**
Science 352, 318 (2016). *F. Donati, S. Rusponi, S. Stepanow, C. Wäckerlin, A. Singha, L. Persichetti, R. Baltic, K. Diller et. al.*

2015 **Strong antiferromagnetic exchange between manganese phthalocyanine and ferromagnetic europium oxide**
Chem. Commun. 51, 12958 (2015). *C. Wäckerlin, F. Donati, A. Singha, R. Baltic, A. C. Uldry, B. Delley, S. Rusponi and J. Dreiser.*

2014 **Magnetism of Ho and Er Atoms on Close-Packed Metal Surfaces**
Phys. Rev. Lett. 113, 237201 (2014). *F. Donati, A. Singha, S. Stepanow, C. Wäckerlin, J. Dreiser, P. Gambardella, S. Rusponi, and H. Brune.*

2014 **Exchange Interaction of Strongly Anisotropic Tripodal Erbium Single-Ion Magnets with Metallic Surfaces**
ACS Nano 8, 4662 (2014) *J. Dreiser, C. Wäckerlin, Md. E. Ali, C. Piamonteze, F. Donati, A. Singha, K. S. Pedersen, S. Rusponi et. al.*

2014 **Single Molecule Activity Measurements of Cytochrome P450 Oxidoreductase Reveal the Existence of Two Discrete Functional States**
ACS Chem. Biol. 9, 630 (2014) *T. Laursen, A. Singha, N. Rantzau, M. Tutkus, J. Borch, P. Hedegård, D. Stamou, B. L. Møller et. al.*

Manuscripts in preparation

$4f$ **Occupancy and Magnetism of Rare Earth Atoms Adsorbed on Metal Substrates**
A. Singha, R. Baltic, F. Donati, C. Wäckerlin, J. Dreiser, L. Persichetti, S. Stepanow, P. Gambardella et. al.

Spin excitations in $4f - 3d$ **heterodimers adsorbed on MgO/Ag(100)**
A. Singha, F. Donati, F. D. Natterer, C. Wäckerlin, F. Patthey, Ž. Šljivančanin, and H. Brune

On-surface synthesis of single molecule magnets
K. Diller, A. Singha, M. Pivetta, S. Rusponi, C. Wäckerlin, R. Hellwig, A. Verdini, A. Cossaro et al.

Magnetism of single rare earth atoms adsorbed on graphene on Ir(111)
R. Baltic, F. Donati, A. Singha, M. Pivetta, C. Wäckerlin, J. Dreiser, S. Rusponi, and H. Brune.

Talks

2017 **APS March Meeting, New Orleans, Louisiana, the United States**
Magnetic properties of rare earth single atoms on metal substrates

2017 **Deutsche Physikalische Gesellschaft, Dresden, Germany**
Magnetic properties of rare earth single atoms on metal substrates

2016 **Deutsche Physikalische Gesellschaft, Regensburg, Germany**
Topic: Magnetic Hysteresis in Er trimers on Cu(111)

2015 **IOP conference, University College London, the United Kingdom**
Topic: Magnetism of Ho and Er atoms on close-packed metal surfaces

Experimental expertise

Scanning Tunneling Microscopy measurements in ultra high vacuum down to 0.4 K.

Synchrotron techniques including XAS, XMCD (X-treme beamline of Swiss Light Source (PSI, Switzerland) and ESRF, ID32), XPS, and NEXAFS (ALOISA beamline of Elettra (Trieste, Italy)).

Single molecule fluorescence microscopy.

Theoretical skills

Atomic multiplet simulations (MultiX) and Mean-field nucleation theory (MFNT).

Academic records

2010 **Master of Science (M.Sc.), Physics**
1^{st} rank in Indian Institute of Technology, Bombay (IITB)
Most outstanding student in the Department of Physics, IIT Bombay

2008 **Bachelor of Science (B.Sc.), Physics**
1^{st} rank at University of Calcutta
Meghnad Saha Centenary Medal, University of Calcutta, India

Software skills

Good level Igor pro, Python, MATLAB, Mathematica, C++, and Latex

Language proficiency

Fluent in English, Hindi, and Bengali. Limited working proficiency in French.

Bibliography

[1] M. Hilbert and P. López, Science **332**, 60 (2011).

[2] J. Stöhr and H. C. Siegmann, "Exchange, spin-orbit, and zeeman interactions," in *Magnetism: From Fundamentals to Nanoscale Dynamics* (Springer Berlin Heidelberg, 2006).

[3] D. Gatteschi, R. Sessoli, and J. Villain, in *Molecular Nanomagnets* (Oxford Scholarship Online, 2006).

[4] C. Hübner, B. Baxevanis, A. A. Khajetoorians, and D. Pfannkuche, Phys. Rev. B **90**, 155134 (2014).

[5] C. Hübner, *Single Spin Switching in Open Quantum Systems*, Ph.D. thesis, University of Hamburg (2015).

[6] M. Marciani, C. Hübner, and B. Baxevanis, Phys. Rev. B **95**, 125433 (2017).

[7] L. Thomas, F. Lionti, R. Ballou, D. Gatteschi, R. Sessoli, and B. Barbara, Nature **383**, 145 (1996).

[8] N. Ishikawa, M. Sugita, and W. Wernsdorfer, Angew. Chem., Int. Ed. **44**, 2931 (2005).

[9] M. Mannini, F. Pineider, P. Sainctavit, C. Danieli, E. Otero, C. Sciancalepore, A. M. Talarico, M.-A. Arrio, A. Cornia, D. Gatteschi, and R. Sessoli, Nat. Mater. **8**, 194 (2009).

[10] M. Mannini, F. Pineider, C. Danieli, F. Totti, L. Sorace, P. Sainctavit, M. Arrio, E. Otero, L. Joly, J. C. Cezar, A. Cornia, and R. Sessoli, Nature **468**, 417 (2010).

[11] M. Mannini, F. Bertani, C. Tudisco, L. Malavolti, L. Poggini, K. Misztal, D. Menozzi, A. Motta, E. Otero, P. Ohresser, P. Sainctavit, G. G. Condorelli, E. Dalcanale, and R. Sessoli, Nat. Commun. **5**, 5582 (2014).

[12] R. Westerström, J. Dreiser, C. Piamonteze, M. Muntwiler, S. Weyeneth, K. Krämer, S.-X. Liu, S. Decurtins, A. Popov, S. Yang, L. Dunsch, and T. Greber, Phys. Rev. B **89**, 060406 (2014).

[13] R. Sessoli, D. Gatteschi, A. Caneschi, and M. A. Novak, Nature **365**, 141 (1993).

[14] A. M. Ako, I. J. Hewitt, V. Mereacre, R. Clérac, W. Wernsdorfer, C. E. Anson, and A. K. Powell, Angew. Chem. Int. Ed. **45**, 4926 (2006).

[15] F. Neese and D. A. Pantazis, Faraday Disc. **148**, 229 (2011).

[16] N. Ishikawa, M. Sugita, T. Ishikawa, S. Koshihara, and Y. Kaizu, J. Am. Chem. Soc. **125**, 8694 (2003).

[17] D. N. Woodruff, R. E. P. Winpenny, and R. A. Layfield, Chem. Rev. **113**, 5110 (2013).

[18] L. Vitali, S. Fabris, A. M. Conte, S. Brink, M. Ruben, S. Baroni, and K. Kern, Nano Lett. **8**, 3364 (2008).

[19] J. Dreiser, C. Wäckerlin, M. E. Ali, C. Piamonteze, F. Donati, A. Singha, K. S. Pedersen, S. Rusponi, J. Bendix, P. M. Oppeneer, T. A. Jung, and H. Brune, ACS Nano **8**, 4662 (2014).

[20] R. Westerström, A.-C. Uldry, R. Stania, J. Dreiser, C. Piamonteze, M. Muntwiler, F. Matsui, S. Rusponi, H. Brune, S. Yang, A. Popov, B. Büchner, B. Delley, and T. Greber, Phys. Rev. Lett. **114**, 087201 (2015).

[21] A. A. Khajetoorians, B. Baxevanis, C. Hübner, T. Schlenk, S. Krause, T. O. Wehling, S. Lounis, A. Lichtenstein, D. Pfannkuche, J. Wiebe, and R. Wiesendanger, Science **339**, 55 (2013).

[22] S. Loth, S. Baumann, C. P. Lutz, D. M. Eigler, and A. J. Heinrich, Science **335**, 196 (2012).

[23] P. Gambardella, S. Rusponi, M. Veronese, S. S. Dhesi, C. Grazioli, A. Dallmeyer, I. Cabria, R. Zeller, P. H. Dederichs, K. Kern, C. Carbone, and H. Brune, Science **300**, 1130 (2003).

[24] H. Brune and P. Gambardella, Surf. Sci. **603**, 1812 (2009).

[25] P. Błoński, A. Lehnert, S. Dennler, S. Rusponi, M. Etzkorn, G. Moulas, P. Bencok, P. Gambardella, H. Brune, and J. Hafner, Phys. Rev. B **81**, 104426 (2010).

[26] C. Carbone, M. Veronese, P. Moras, S. Gardonio, C. Grazioli, P. H. Zhou, O. Rader, A. Varykhalov, C. Krull, T. Balashov, A. Mugarza, P. Gambardella, S. Lebègue, O. Eriksson, M. I. Katsnelson, and A. I. Lichtenstein, Phys. Rev. Lett. **104**, 117601 (2010).

[27] P. Gambardella, A. Dallmeyer, K. Maiti, M. C. Malagoli, W. Eberhardt, K. Kern, and C. Carbone, Nature **416**, 301 (2002).

[28] C. F. Hirjibehedin, C.-Y. Lin, A. F. Otte, M. Ternes, C. P. Lutz, B. A. Jones, and A. J. Heinrich, Science **317**, 1199 (2007).

[29] A. Lehnert, S. Rusponi, M. Etzkorn, S. Ouazi, P. Thakur, and H. Brune, Phys. Rev. B **81**, 104430 (2010).

[30] F. Donati, L. Gragnaniello, A. Cavallin, F. D. Natterer, Q. Dubout, M. Pivetta, F. Patthey, J. Dreiser, C. Piamonteze, S. Rusponi, and H. Brune, Phys. Rev. Lett. **113**, 177201 (2014).

[31] G. E. Pacchioni, L. Gragnaniello, F. Donati, M. Pivetta, G. Autès, O. V. Yazyev, S. Rusponi, and H. Brune, Phys. Rev. B. **91**, 235426 (2015).

[32] S. Baumann, F. Donati, S. Stepanow, S. Rusponi, W. Paul, S. Gangopadhyay, I. G. Rau, G. E. Pacchioni, L. Gragnaniello, M. Pivetta, J. Dreiser, C. Piamonteze, C. P. Lutz, R. M. Macfarlane, B. A. Jones, P. Gambardella, A. J. Heinrich, and H. Brune, Phys. Rev. Lett. **115**, 237202 (2015).

[33] I. G. Rau, S. Baumann, S. Rusponi, F. Donati, S. Stepanow, L. Gragnaniello, J. Dreiser, C. Piamonteze, F. Nolting, S. Gangopadhyay, O. R. Albertini, R. M. Macfarlane, C. P. Lutz, B. A. Jones, P. Gambardella, A. J. Heinrich, and H. Brune, Science **344**, 988 (2014).

[34] S. Baumann, *Investigation of the unusual magnetic properties of Fe and Co on MgO with high spatial, energy and temporal resolution*, Ph.D. thesis, University of Basel (2015).

[35] J. Stöhr and H. C. Siegmann, "Electronic and magnetic interactions in solids," in *Magnetism: From Fundamentals to Nanoscale Dynamics* (Springer Berlin Heidelberg, 2006).

[36] T. Schuh, T. Miyamachi, S. Gerstl, M. Geilhufe, M. Hoffmann, S. Ostanin, W. Hergert, A. Ernst, and W. Wulfhekel, Nano Lett. **12**, 4805 (2012).

[37] T. Miyamachi, T. Schuh, T. Markl, C. Bresch, T. B., A. Stohr, C. Karlewski, S. Andre, M. Marthaler, M. Hoffmann, M. Geilhufe, S. Ostanin, W. Hergert, I. Mertig, G. Schon, A. Ernst, and W. Wulfhekel, Nature **503**, 242 (2013).

[38] K. T. Rim, K. H. Koo, and J. S. Park, Saf. Health Work **4**, 12 (2013).

[39] C. Piamonteze, U. Flechsig, S. Rusponi, J. Dreiser, J. Heidler, M. Schmidt, R. Wetter, M. Calvi, T. Schmidt, H. Pruchova, J. Krempasky, C. Quitmann, H. Brune, and F. Nolting, J. Synchrotron Radiat. **19**, 661 (2012).

[40] F. Donati, A. Singha, S. Stepanow, C. Wäckerlin, J. Dreiser, P. Gambardella, S. Rusponi, and H. Brune, Phys. Rev. Lett. **113**, 237201 (2014).

[41] F. Donati, S. Rusponi, S. Stepanow, C. Wäckerlin, A. Singha, L. Persichetti, R. Baltic, K. Diller, F. Patthey, E. Fernandes, J. Dreiser, Ž. Šljivančanin, K. Kummer, C. Nistor, P. Gambardella, and H. Brune, Science **352**, 318 (2016).

[42] A. Singha, F. Donati, C. Wäckerlin, R. Baltic, J. Dreiser, M. Pivetta, S. Rusponi, and H. Brune, Nano Lett. **16**, 3475 (2016).

[43] R. Gaisch, J. Gimzewski, B. Reihl, R. Schlittler, M. Tschudy, and W. Schneider, Ultramicroscopy **42**, 1621 (1992).

[44] L. Claude, *Construction d'un microscope á effet tunnel á basse température et études d'impuretés magnétiques en surfaces*, Ph.D. thesis, École Polytechnique Fédéral de Lausanne (2005).

[45] Q. Dubout, *Magnetism of Single Adatoms and Small Adsorbed Clusters Investigated by Means of Low-Temperature STM*, Ph.D. thesis, École Polytechnique Fédéral de Lausanne (2013).

[46] J. Stöhr and H. C. Siegmann, *Magnetism: From Fundamentals to Nanoscale Dynamics* (Springer Berlin Heidelberg, 2006).

[47] R. D. Cowan, *The Theory of Atomic Structure and Spectra* (University of California Press, Berkeley, 1981).

[48] B. T. Thole, P. Carra, F. Sette, and G. van der Laan, Phys. Rev. Lett. **68**, 1943 (1992).

[49] P. Carra, B. T. Thole, M. Altarelli, and X. Wang, Phys. Rev. Lett. **70**, 694 (1993).

[50] S. Lounis, ArXiv e-prints (2014), arXiv:1404.0961 [cond-mat.mes-hall] .

[51] J. Bardeen, Phys. Rev. Lett. **6**, 57 (1961).

[52] J. Müller, "Stm: a project by jürgen müller," (2006).

[53] M. Ternes, *Scanning Tunneling Spectroscopy at the Single Atom Scale*, Ph.D. thesis, École Polytechnique Fédéral de Lausanne (2006).

[54] G. Zinsmeister, Vacuum **16**, 529 (1966).

[55] G. Zinsmeister, Thin Solid Films **7**, 51 (1971).

[56] J. A. Venables, G. D. T. Spiller, and M. Hanbücken, Rep. Prog. Phys. **47**, 399 (1984).

[57] H. Brune, Surf. Sci. Rep. **31**, 125 (1998).

[58] N. Knorr, H. Brune, M. Epple, A. Hirstein, M. A. Schneider, and K. Kern, Phys. Rev. B **65**, 115420 (2002).

[59] F. de Groot, Coord. Chem. Rev. **249**, 31 (2005).

[60] A. Uldry, F. Vernay, and B. Delley, Phys. Rev. B **85**, 125133 (2012).

[61] N. F. Chilton, D. Collison, E. J. L. McInnes, R. E. P. Winpenny, and A. Soncini, Nat. Commun. **4**, 3551 (2013).

[62] J. J. Baldoví, J. M. Clemente-Juan, E. Coronado, and A. Gaita-Ariño, Inorg. Chem. **53**, 11323 (2014).

[63] B. Bryant, A. Spinelli, J. J. T. Wagenaar, M. Gerrits, and A. F. Otte, Phys. Rev. Lett. **111**, 127203 (2013).

[64] W. Wernsdorfer and R. Sessoli, Science **284**, 133 (1999).

[65] K. Blum, *Density Matrix Theory and Applications* (Springer, 2011).

[66] D. Karevski, V. Popkov, and G. M. Schütz, ArXiv e-prints (2016), arXiv:1612.03601 [math-ph] .

[67] M. Ternes, C. Weber, M. Pivetta, F. Patthey, J. P. Pelz, T. Giamarchi, F. Mila, and W.-D. Schneider, Phys. Rev. Lett. **93**, 146805 (2004).

[68] F. Silly, M. Pivetta, M. Ternes, F. Patthey, J. P. Pelz, and W.-D. Schneider, Phys. Rev. Lett. **92**, 016101 (2004).

[69] B. T. Thole, G. van der Laan, J. C. Fuggle, G. A. Sawatzky, R. C. Karnatak, and J. M. Esteva, Phys. Rev. B **32**, 5107 (1985).

[70] M. Steinbrecher, A. Sonntag, M. dos Santos Dias, M. Bouhassoune, S. Lounis, J. Wiebe, R. Wiesendanger, and A. A. Khajetoorians, Nat. Commun. **7**, 10454 (2015).

[71] D. Coffey, J. L. Diez-Ferrer, D. Serrate, M. Ciria, C. d. l. Fuente, and J. I. Arnaudas, Sci. Rep. **5**, 13709 (2015).

[72] A. Delin, L. Fast, B. Johansson, J. M. Wills, and O. Eriksson, Phys. Rev. Lett. **79**, 4637 (1997).

[73] L. Peters, S. Ghosh, B. Sanyal, C. van Dijk, J. Bowlan, W. de Heer, A. Delin, I. di Marco, O. Eriksson, M. I. Katsnelson, B. Johansson, and A. Kirilyuk, Sci. Rep. **6**, 19676 (2016).

[74] B. Johansson, Phys. Rev. B **20**, 1315 (1979).

[75] G. Meyer, Chem. Rev. **88**, 93 (1988).

[76] E. Lundgren, J. N. Andersen, R. Nyholm, X. Torrelles, J. Rius, A. Delin, A. Grechnev, O. Eriksson, C. Konvicka, M. Schmid, and P. Varga, Phys. Rev. Lett. **88**, 136102 (2002).

[77] M. Domke, C. Laubschat, M. Prietsch, T. Mandel, G. Kaindl, and W. D. Schneider, Phys. Rev. Lett. **56**, 1287 (1986).

[78] L. Peters, I. Di Marco, M. S. Litsarev, A. Delin, M. I. Katsnelson, A. Kirilyuk, B. Johansson, B. Sanyal, and O. Eriksson, Phys. Rev. B **92**, 035143 (2015).

[79] C. Nistor, A. Mugarza, S. Stepanow, P. Gambardella, K. Kummer, J. L. Diez-Ferrer, D. Coffey, C. de la Fuente, M. Ciria, and J. I. Arnaudas, Phys. Rev. B **90**, 064423 (2014).

[80] R. Baltic, M. Pivetta, F. Donati, C. Wäckerlin, A. Singha, J. Dreiser, S. Rusponi, and H. Brune, Nano Lett. **16**, 7610 (2016).

[81] P. Gambardella, S. S. Dhesi, S. Gardonio, C. Grazioli, P. Ohresser, and C. Carbone, Phys. Rev. Lett. **88**, 047202 (2002).

[82] Y. Teramura, A. Tanaka, B. Thole, and T. Jo, J. Phys. Soc. Jpn. **65**, 3056 (1996).

[83] B. T. Thole, G. van der Laan, and G. A. Sawatzky, Phys. Rev. Lett. **55**, 2086 (1985).

[84] G. Kaindl, G. Kalkowski, W. D. Brewer, B. Perscheid, and F. Holtzberg, J. Appl. Phys. **55**, 1910 (1984).

[85] C. Kittel, in *Introduction to Solid State Physics* (John Wiley and Sons, Inc) p. 50.

[86] P. Quaino, E. Santos, G. Soldano, , and W. Schmickler, Adv. Phys. Chem. **2011**, 1 (2011).

[87] D. A. Papaconstantopoulos, in *Handbook of the Band Structure of Elemental Solids* (Springer, 1985).

[88] J. Stöhr and H. C. Siegmann, "Interactions of polarized photons with matter," in *Magnetism: From Fundamentals to Nanoscale Dynamics* (Springer Berlin Heidelberg, 2006).

[89] J. R. Smith, J. Ferrante, and J. H. Rose, Phys. Rev. B **25**, 1419 (1982).

[90] Y. Shapira, M. T. Liu, S. Foner, R. J. Howard, and W. H. Armstrong, Phys. Rev. B **63**, 094422 (2001).

[91] Y. Shapira, M. T. Liu, S. Foner, P. J. Bonitatebus, and R. J. Howard, Phys. Rev. B **59**, 1046 (1999).

[92] A. A. Khajetoorians, T. Schlenk, B. Schweflinghaus, M. dos Santos Dias, M. Steinbrecher, M. Bouhassoune, S. Lounis, J. Wiebe, and R. Wiesendanger, Phys. Rev. Lett. **111**, 157204 (2013).

[93] H. Brune, G. S. Bales, J. Jacobsen, C. Boragno, and K. Kern, Phys. Rev. B **60**, 5991 (1999).

[94] F. Meier, L. Zhou, J. Wiebe, and R. Wiesendanger, Science **320**, 82 (2008).

[95] A. A. Khajetoorians, J. Wiebe, B. Chilian, S. Lounis, S. Blügel, and R. Wiesendanger, Nat. Phys. **8**, 497 (2012).

[96] N. N. Negulyaev, V. S. Stepanyuk, L. Niebergall, P. Bruno, M. Pivetta, M. Ternes, F. Patthey, and W.-D. Schneider, Phys. Rev. Lett. **102**, 246102 (2009).

[97] T. R. Umbach, M. Bernien, C. F. Hermanns, A. Krüger, V. Sessi, I. Fernandez-Torrente, P. Stoll, J. I. Pascual, K. J. Franke, and W. Kuch, Phys. Rev. Lett. **109**, 267207 (2012).

[98] J. D. Rinehart and J. R. Long, Chem. Sci. **2**, 2078 (2011).

[99] R. W. Green, S. Legvold, and F. H. Spedding, Phys. Rev. **122**, 827 (1961).

[100] J. Dreiser, R. Westerström, C. Piamonteze, F. Nolting, S. Rusponi, H. Brune, S. Yang, A. Popov, L. Dunsch, and T. Greber, Appl. Phys. Lett. **105**, 032411 (2014).

[101] X. P. Zhang, B. F. Miao, L. Sun, C. L. Gao, A. Hu, H. F. Ding, and J. Kirschner, Phys. Rev. B **81**, 125438 (2010).

[102] R. Cao, X. Zhang, B. Miao, Z. Zhong, L. Sun, B. You, A. Hu, and H. Ding, Surf. Sci. **610**, 65 (2013).

[103] M. Pivetta, G. E. Pacchioni, U. Schlickum, J. V. Barth, and H. Brune, Phys. Rev. Lett. **110**, 086102 (2013).

[104] A. Sperl, J. Kröger, N. Néel, H. Jensen, R. Berndt, A. Franke, and E. Pehlke, Phys. Rev. B **77**, 085422 (2008).

[105] A. Spinelli, B. Bryant, F. Delgado, J. Fernández-Rossier, and A. F. Otte, Nat. Mater. **13**, 782 (2014).

[106] S. Ouazi, S. Wedekind, G. Rodary, H. Oka, D. Sander, and J. Kirschner, Phys. Rev. Lett. **108**, 107206 (2012).

[107] W. Wernsdorfer, E. B. Orozco, K. Hasselbach, A. Benoit, B. Barbara, N. Demoncy, A. Loiseau, H. Pascard, and D. Mailly, Phys. Rev. Lett. **78**, 1791 (1997).

[108] J. Hermenau, J. Ibañez-Azpiroz, C. Hübner, A. Sonntag, B. Baxevanis, K. T. Ton, M. Steinbrecher, A. A. Khajetoorians, M. dos Santos Dias, S. Blügel, R. Wiesendanger, S. Lounis, and J. Wiebe, ArXiv e-prints (2017), arXiv:1703.09419 [cond-mat.mes-hall] .

[109] F. D. Natterer, K. Yang, W. Paul, P. Willke, T. Choi, T. Greber, A. J. Heinrich, and C. P. Lutz, Nature **543**, 226 (2017).

[110] L. T. Baczewski, D. Givord, J. M. Alameda, B. Dieny, J. Nozieres, J. P. Rebouillat, and J. J. Prejean, Acta Phys. Pol. A. **83**, 629 (1993).

[111] C. Wäckerlin, F. Donati, A. Singha, R. Baltic, S. Rusponi, K. Diller, F. Patthey, M. Pivetta, Y. Lan, S. Klyatskaya, M. Ruben, H. Brune, and J. Dreiser, Adv. Mater. **28**, 5195 (2016).

[112] E. Fernandes, F. Donati, F. Patthey, S. Stavric, Ž. Šljivančanin, and H. Brune, (Submitted to Phys. Rev. B., 2017).

[113] W. Paul, K. Yang, S. Baumann, N. Romming, T. Choi, C. P. Lutz, and A. J. Heinrich, Nat Phys **13**, 403 (2016).

[114] G. Chen, J. Zhu, A. Quesada, J. Li, A. T. N'Diaye, Y. Huo, T. P. Ma, Y. Chen, H. Y. Kwon, C. Won, Z. Q. Qiu, A. K. Schmid, and Y. Z. Wu, Phys. Rev. Lett. **110**, 177204 (2013).

[115] Y. Janssen, *Interplay between magnetic anisotropy and exchange interactions in rare-earth-transition-metal ferrimagnets*, Ph.D. thesis, Universiteit van Amsterdam (2003).

[116] A. J. Heinrich, J. A. Gupta, C. P. Lutz, and D. M. Eigler, Science **306**, 466 (2004).

[117] S. Loth, K. von Bergmann, M. Ternes, A. F. Otte, C. P. Lutz, and A. J. Heinrich, Nat. Phys. **6**, 340 (2010).

[118] S. Loth, M. Etzkorn, C. P. Lutz, D. M. Eigler, and A. J. Heinrich, Science **329**, 1628 (2010).

[119] F. Branzoli, P. Carretta, M. Filibian, M. J. Graf, S. Klyatskaya, M. Ruben, F. Coneri, and P. Dhakal, Phys. Rev. B **82**, 134401 (2010).

[120] S. Stepanow, J. Honolka, P. Gambardella, L. Vitali, N. Abdurakhmanova, T.-C. Tseng, S. Rauschenbach, S. L. Tait, V. Sessi, S. Klyatskaya, M. Ruben, and K. Kern, J. Am. Chem. Soc. **132**, 11900 (2010).

[121] L. Margheriti, D. Chiappe, M. Mannini, P. Car, P. Sainctavit, M.-A. Arrio, F. B. de Mongeot, J. C. Cezar, F. M. Piras, A. Magnani, E. Otero, A. Caneschi, and R. Sessoli, Adv. Mater. **22**, 5488 (2010).

[122] M. Gonidec, R. Biagi, V. Corradini, F. Moro, V. De Renzi, U. del Pennino, D. Summa, L. Muccioli, C. Zannoni, D. B. Amabilino, and J. Veciana, J. Am. Chem. Soc. **133**, 6603 (2011).

[123] D. Klar, A. Candini, L. Joly, S. Klyatskaya, B. Krumme, P. Ohresser, J.-P. Kappler, M. Ruben, and H. Wende, Dalton Trans. **43**, 10686 (2014).

[124] S. Rusponi, M. Papagno, P. Moras, S. Vlaic, M. Etzkorn, P. M. Sheverdyaeva, D. Pacilé, H. Brune, and C. Carbone, Phys. Rev. Lett. **105**, 246803 (2010).

[125] K. Diller, A. C. Papageorgiou, F. Klappenberger, F. Allegretti, J. V. Barth, and W. Auwarter, Chem. Soc. Rev. **45**, 1629 (2016).

[126] K. Katoh, Y. Yoshida, M. Yamashita, H. Miyasaka, B. K. Breedlove, T. Kajiwara, S. Takaishi, N. Ishikawa, H. Isshiki, Y. F. Zhang, T. Komeda, M. Yamagishi, and J. Takeya, J. Am. Chem. Soc. **131**, 9967 (2009).

[127] S. Fahrendorf, N. Atodiresei, C. Besson, V. Caciuc, F. Matthes, S. Blügel, P. Kögerler, D. E. Bürgler, and C. M. Schneider, Nat. Commun. **4**, 2425 (2013).

[128] D. Écija, W. Auwärter, S. Vijayaraghavan, K. Seufert, F. Bischoff, K. Tashiro, and J. V. Barth, Angew. Chem. Int. Ed. **50**, 3872 (2011).

[129] R. P. Feynman, in Annual Meeting of the American Physical Society (1959).

[130] S. Baumann, W. Paul, T. Choi, C. P. Lutz, A. Ardavan, and A. J. Heinrich, Science **350**, 417 (2015).

[131] S. Thiele, F. Balestro, R. Ballou, S. Klyatskaya, M. Ruben, and W. Wernsdorfer, Science **344**, 1135 (2014).

[132] K. S. Pedersen, A.-M. Ariciu, S. McAdams, H. Weihe, J. Bendix, F. Tuna, and S. Piligkos, J. Am. Chem. Soc. **138**, 5801 (2016).

[133] Y.-S. Ding, Y.-F. Deng, and Y.-Z. Zheng, Magnetochemistry **2**, 40 (2016).

[134] I. D. Hughes, M. Dane, A. Ernst, W. Hergert, M. Luders, J. Poulter, J. B. Staunton, A. Svane, Z. Szotek, and W. M. Temmerman, Nature **446**, 650 (2007).